Trinity College Dublin
Coláiste na Tríonóide, Baile Átha Cliath
The University of Dublin

Electromigration of atoms on vicinal surfaces at high temperatures

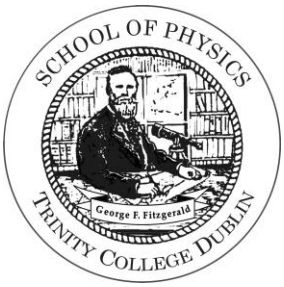

Olzat Toktarbaiuly

A thesis submitted to the *University of Dublin* in application for the degree of *Doctor of Philosophy*

School of Physics,
University of Dublin,
Trinity College Dublin.
Ireland

September 2015

Declaration of Authorship

This thesis is submitted by the undersigned for examination for the degree of Doctor of Philosophy at the University of Dublin. It has not been submitted as an exercise for a degree at any other University.

With the exception of assistance noted in the acknowledgements, this thesis is entirely my own work for a degree in this or any other university.

I agree that Trinity College library may lend or copy this thesis freely upon request.

_____

Olzat Toktarbaiuly

Dated: September 2015

Менің бақилық болған ата-анама арнаймын!

Summary

This thesis deals with the theoretical and experimental study of antiband formation on terraces between step bunches of Si(111) and shows for the first time step bunching formation on vicinal Al_2O_3(0001), W(110), and $MgAl_2O_4$(100) surfaces. Step bunching instability occurs on these surfaces due to the influence of the electromigration field which is directed perpendicular to the step direction. The results obtained on electromigration induced step bunching on insulating and metallic surfaces indicates that this phenomena is universal.

The thesis is divided into eight chapters. Chapter 1 gives an introduction and motivation for this current study. The second chapter provides an overview to the theoretical background of the phenomenon of electromigration induced step bunching. The third chapter deals with the experimental methods and experimental equipment used.

Chapter 4 examines the formation of antibands on Si(111), and the effect of miscut angle on these structures is investigated. It is known that prolonged direct current–annealing of Si(111) results in the formation of antibands; i.e., the step bunches with opposite slope to the primary bunches. A theoretical description for the formation of antibands is provided, and the criteria for the onset of antiband formation are determined under conditions of sublimation controlled by slow adatom diffusion. The effect of changing the electromigration field on antiband instability of Si(111) was investigated at 1270°C and compared to the theoretical model. The experiment strongly supports the validity of the theoretical model and indicates the significance of the factor of critical electric field in theoretical models of step bunching and antiband instabilities. The lower limit for kinetic characteristic length (d_s = 0.3 nm) provides an upper limit for the effective charge of the surface atoms on Si of +2e. Here it is found that values for d_s in the range of 1.7-4.5nm provide a value for effective charge that is in line with previous studies.

In chapter 5 the electromigration induced step bunching process on vicinal surfaces of Al_2O_3(0001) will be shown. Electromigration fields of $E \approx$ 30-140 V/cm were applied in the step-up direction at 1500 ˚C leading to formation of step bunching. It was further found

that under similar conditions regular step arrays are attained when annealed with the electric field applied in the step-down direction. However, prolonged annealing time in the same direction can lead to the formation of weakened step bunches. The relationships between the step bunches' height and their slope, evolution of crossing steps towards the antibands and finally the existence of a critical field ($E_{cr} \approx 30$ V/cm) are investigated.

Chapter 6 deals with the experimentally observed electromigration induced step bunching on W(110). The surface morphology of bunched W(110) was studied with varying miscut angles and orientations. An applied electric field as small as 30 mV/cm was found to be sufficient to induce step bunching on vicinal W(110) while annealing in the both step-up and step-down directions at 1500 ˚C. A scaling relationship between the maximum slope of a step bunch, y_m, and its height, h, was detected and was analysed by the fitting of a power law function ($y_m \sim h^{\alpha}$). Experimental results show that higher electric field results in higher step bunches on W(110).

Chapter 7 demonstrates the step bunching instability on vicinal $MgAl_2O_4$(100) surfaces. Annealing $MgAl_2O_4$(100) with electromigration field $E \approx 140$ V/cm at 1400 ˚C in the step-up direction produces step bunches separated by large terraces, while annealing in the step-down direction causes the creation of a faceted surface. The morphological changes on the terraces of the bunched surface is discussed. The scaling relationships between the maximum slope of a step bunch, y_m, and step bunch height h was analyzed using a power law relationship ($y_m \sim h^{\alpha}$).

Finally chapter 8 will summarise the main findings of this work and also outline potentially interesting further investigations that could be carried out.

Acknowledgements

I have had a great and unforgettable time during my PhD study at Trinity College Dublin. I have been surrounded by a warm atmosphere of people who supported and gave advice to me throughout my study. First I would like to especially thank to my one of my best school friends Saken, who introduced me to Prof. Igor Shvets and recommended to him that I join his Applied Physics Group.

Of course, firstly I would like to express my biggest thanks to my supervisor Prof. Igor Shvets for giving me chance to study in his research group and for his excellent supervision. He gave me invaluable advice and guidance all these years. I have learned a lot from him as he is a great source of ideas and I am still learning.

Secondly, I would like to thank my international scholarship “Bolashak” of Kazakhstan for the financial support. Particular thanks to manager of the Europe office Elvira Myrzaliyeva in JSC “Center for International Programs”.

I would especially like to thank Dr Victor Usov. I appreciate his excellent supervision and scientific suggestions. Thanks to Dr Cormac O'Coilean who is my long term colleague. He has helped me a lot in the lab and made helpful discussions.

Special thanks first co-supervisor Dr. Sergey Krasnikov and colleagues Dr Olaf Lübben and Dr Barry Murphy from STM subgroup. They provided tremendous support and guidance to me in these experiments. I would like to give my sincere appreciation to Dr Sergey Boshko who was the invited researcher from Moscow. He was the great teacher because he provided a number of physical problems and resources to solve them. He is very patient listener and gracious person. Also another big thanks to invited researcher Dr Alexandr Chaika. I’ll never forget his valuable advice. I’d like to thank all group members, past and present. Especial thanks to Dr Brendan O’ Dowd, Brian Walls, David and Daragh for correcting my PhD thesis and also to Dr Karsten Fleischer for his great scientific points. Thanks to Jeanette Cummins and Ellen Bowman for helping to solve administrative issues.

I would like to give my sincere thanks to my Kazakh friends with whom I studied at the same faculty of Kazakh National University. Thanks to Ozhet for his friendly encouragement

and many hours of discussion. Thanks to Oral for his help and assistance during the long time we spent together. Thanks to Azat and Askar for support when I had some financial circumstances. I would like to thank to Nurlan for keeping my sense of humor. Many thanks to my friends in Kazakhstan: Serikbol, Shyngys, Bolatbek. Thanks to my friend Ehsan who brought me opportunities to participate in chemistry society activities. Also thanks to my Brazilian friends Vilmar and Amaury for introducing me culture of Brazil.

Unfortunately, my father and mother are early left this life and could not see my PhD graduation. Without my parents' endless love and education I would not be the man I am today. However, I have a little brother and two sisters with whom I am proud of it.

Finally, the huge thanks to my lovely wife Gaukhar and my son Yerassyl. Their love, moral support and endless comprehension still give me soulful power.

Publications

1. V. Usov, S. Stoyanov, C. Ó Coileáin, **O. Toktarbaiuly**, and I.V.Shvets
   Antiband instability on vicinal Si (111) under the condition of diffusion-limited sublimation. *Phys. Rev. B* **86**, 195317 (2012). DOI: 10.1103/PhysRevB.86.195317.

2. A. Syrlybekov, E. Arca, R. Verre, C. Ó Coileáin, **O. Toktarbaiuly,** A. Khalid, H. Zhang, and I. V. Shvets.
   Induced morphological changes of vicinal MgO (100) under high temperature anneal: step formation and surface stability. *Surface and Interface Analysis* **47**, 969 (2015). DOI: 10.1002/sia.5805.

3. **O. Toktarbaiuly**, V. Usov, C. Ó Coileáin[1], E. Norton, S. Bozhko, V. Semenov, A. Chaika, S. Krasnikov,[1] O. Lübben,[1] Barry E. Murphy,[1] A. Syrlybekov, B. Walls, G. Cross, and I. Shvets.
   Electromigration induced Step Bunching on W(110).
   (*In preparation*)

4. **O. Toktarbaiuly**, V. Usov, C. Ó Coileáin, E. Norton, and I. Shvets.
   Electromigration induced step bunching on vicinal α-Al_2O_3(0001) surfaces at high temperatures.
   (*In preparation*)

5. **O. Toktarbaiuly**, C. Ó Coileáin, and I. Shvets.
   Electromigration induced step bunching on vicinal $MgAl_2O_4$(100) at high temperatures.
   (*In preparation*)

Abbreviations

DC – Direct current
STM – Scanning tunneling microscopy
LEED – Low energy electron diffraction
UHV – Ultra high vacuum
AFM – Atomic force microscope
NC-AFM – Noncontact atomic force microscopy
XRD – X-ray diffraction
SXRD – surface X-ray diffraction
FWHM – Full width at half Maximum
BCF – Burton-Cabrera-Frank
FCC – Face centered cubic
XPS – X-ray Photoelectron Spectroscopy

Contents

Chapter 1

Introduction and Motivation

Ақыл - тозбайтын тон,

Білім – таусылмайтын кен.

It has been long known that atomic steps on crystalline vicinal surfaces affect the dynamics of multiple processes such as atom or molecule adsorption, the nucleation and growth of thin films, and chemical and catalytic reactions at surfaces [1-3]. Vicinal surfaces with high uniformity and regularity can be created in a relatively simple way by cutting single crystals at a small angle from a low index crystallographic plane. Since atomic steps can hinder (or even improve) the performance of certain devices, it is important that we understand their behavior so that their influence can be controlled.

Atoms at the step edge and kink positions have lower bond saturation than atoms comprising terraces and can potentially demonstrate increased reactivity [4]. Also, substrates' atomic steps provide favourable positions for adatom attachment during epitaxial film growth, which makes vicinal surfaces ideal as templates for directing ordered growth of thin films and nanowire arrays [5-7]. In addition, the stepped morphology of surfaces creates active sites for catalytic reactions to occur at the step edges. For instance, the N_2 dissociation on Ru(0001) is totally dominated by atomic steps with the adsorption rate at the steps being at least 9 orders of magnitude higher than on terraces at 500 K and corresponding difference in activation energy of 1.5 eV [8]. Furthermore, catalytic

reductions or molecule dissociation predominantly occur at particular sites and stepped surfaces of metal oxides can expose chemically different surface terminations [9-11].

Aside from catalytic reactions, vicinal surfaces allow a degree of anisotropy to be introduced into magnetic properties of heteroepitaxial ultrathin films. Atomic steps locally break films' rotational symmetry forcing additional in-plane step-induced uniaxial anisotropy between magnetically equivalent crystallographic directions. This in turn can affect the magnetic properties of the thin film, in some cases causing the original magnetic easy axes to rotate towards other directions [12-19].

The ability to manipulate the size, shape, height and interatomic distance of atomic step enhances the potential for existing and proposed applications [20, 21]. The evolution and arrangement of crystalline surfaces at high temperatures driven by thermodynamic and kinetic processes involves adatom diffusion on terraces, attachment/detachment of adatoms at the step edges and adsorption/desorption of adatoms from the surface. In this regard, the diffusion of adatoms induced by electromigration is of interest for the control of the self-organisation processes on the crystalline surface, in particular in the case of step bunching instabilities which consist of agglomerated steps separated by wide atomically flat terraces. Starting from evenly spaced atomic steps, the flat terraces produced by step bunching can be up to several μm wide, with hundreds of atomic steps in the bunch. The step density within the bunches is quite high, with consequent angles of the bunch of up to 30 degrees with respect to the flat, low-index terraces.

The phenomenon of step bunching on the surface of single crystals of Si(111) was first observed by Latyshev *et al.* in 1989 [22]. They found that atomic steps could be caused to bunch together by passing direct current (DC) through the sample. Since Latyshev's discovery of step bunching on Si(111) the focus has been on electromigration induced step bunching on silicon surfaces [23-30]. This interest has been further stimulated by potential nanotechnology-style applications of stepped Si(111) substrates [5, 27, 31].

The most fascinating aspect of the step bunching behaviour on Si(111) is the fact that the final state of the bunched surface strongly depends on the current direction and temperature. The electric field must be oriented in either in the "step-up" or "step-down" direction relative to the miscut direction to produce the step-bunching instability. There

are four recognized temperature regimes where the step bunching of Si(111) surface occurs, requiring alternate current directions with increasing temperature. Bunching takes place only if the current flows in the step-down direction in the temperature regimes I (∼850-950˚C) and III (∼1200-1300˚C), while a reversed current direction is necessary for temperature regimes II (∼1040-1190˚C) and IV (>1300˚C) [22]. If the electric field orientation is opposite to the stated regimes then the surface adopts an array of uniformly spaced single-atomic height steps. The relationship between current direction and temperature required to achieve step bunching is believed to be related to temperature-dependent changes in the "transparency" (permeability) of atomic steps to the flow of Si adatoms, which is determined by the kink density within the steps [32], although the nature or relevance of this mechanism is still debated. It is generally accepted that surface atoms may acquire a small effective charge which causes them to drift parallel or anti-parallel to the applied DC when under the influence of the electric field [24, 33, 34]. This is different to studies of surface shape evolution, which is driven by the reduction of the surface free energy without an external driving force [35-37]. The adatom electromigration also gives rise to surface features such as step-wandering [38, 39] and step density waves [40].

It was found that prolonged DC annealing of Si(111) allows the surface morphology to further develop, giving rise to new morphologies such as antibands which can be described as step bunches with slopes of the opposite sign as compared to the primary bunches [41]. Antibands are primarily formed via the shape evolution of atomic steps crossing the wide terraces between step bunches. At a certain stage of their development these crossing steps acquire an S-shape, which does not manifest self-similarity when the terrace width grows wider, i.e. beyond a certain terrace width these S-shaped steps lose their stability and further develop towards a less symmetric shape.

A number of theories have been proposed to explain the step bunching mechanism of Si(111) [42-44]. Stoyanov proposed that the atomic steps could be "transparent" or "non-transparent" depending on electric field directions, and his model could be used to explain the alternating directions of electric field required in the various temperature regimes. [23, 45]. The steps are said to be nontransparent when the kink density is high and adatoms easily migrate along the step edges and attach to the kink positions. In this case the step

bunching takes place for the step-down electromigration [26]. Contrary to this, the steps are described as transparent when the density of kinks is low and most adatoms cross the steps without taking part in the exchange between the crystal phase and the dilute layer of migrating adatoms. The step bunching in the transparent steps model occurs for the step-up electromigration [29].

Surface electromigration acting on a diffusing adatom consists of a "direct electrostatic force", which requires that the adatoms are ionized and carry some effective charge and an "electron wind" force due to momentum exchange between the current carrying electrons and the migrating ions [46, 47]. For metal, the electron wind force is believed to be the dominant force contributing to electromigration [48], while for semiconductors it is the electrostatic force which has the greatest influence [28]. Electromigration can have a profound influence on surface morphology [49, 50] and can lead to the development of macro-scale steps [51, 52]. However these studies have made no observations of step bunching on metallic and insulating surfaces.

The question addressed by this study is: can electromigration in metals and insulating oxide surfaces cause step bunching and if so, then what are the differences or similarities between the phenomena in Si and in metallic or insulating oxide surfaces. There are two motivations for this research. Firstly, understanding the fundamentals of electromigration and secondly, numerous current and prospective technology applications.

This thesis presents for the first time that the step bunching driven by electromigration is a universal effect that can be induced on a variety of crystallographic surfaces including metals and insulating oxides. This is demonstrated by analysis of surface morphologies created by electromigration on W(110), Al_2O_3(0001) and $MgAl_2O_4$(100). The observed step bunched surfaces closely resemble the morphological features created on Si(111) by directional drift of Si surface atoms. The main similarity between the step bunching behavior on insulating oxide surfaces and Si(111) is the fact that the final state of the bunched surface strongly depends on the electric field (*E*-field) annealing direction. However, this is in contrast with the behavior on W(110) where step bunching occurs regardless of *E*-field direction. The finding suggest that the mechanism of step bunching on

the Si(111) and insulating oxides is fundamentally the same and that there are significant differences existing between bunched metallic tungsten and silicon surfaces.

Chapter 2

Step Bunching Morphology

Ғылым – теңіз, білім – қайық.

This chapter will give an introduction to the atomic structure of vicinal surfaces and will cover the background of the step bunching behavior on Si(111) induced by electromigration. In addition, the surface morphologies that can be created on the terraces between step bunches on Si(111) will be described.

First I will introduce silicon, on which the effect of electromigration induced step bunching has been widely investigated. This is followed by sapphire, which has had some research showing faceting and step bunching under thermal annealing. Then tungsten and spinel structure are introduced, on which step bunching induced by the electric field has not yet been shown. These materials are chosen as exemplars of different classes of material.

2.1 Vicinal Surfaces

A surface of a crystal which is imperfectly aligned with a low index plane is called a vicinal surface and is characterized by a series of atomic steps. The angle of inclination between the surface and the crystal plane is known as the miscut angle and is typically less than 6 degrees. Figure 2.1(a) demonstrates a schematic of an untreated initial surface. The degree

of miscut can be determined by using the simple expression tan $\vartheta = h_0/l_0$, where is the h_0 initial step height and l_0 is the initial terrace width. The step height is defined by the thickness of a single atomic layer. Figure 2.1(b) shows the case where single steps under suitable annealing conditions gather together to form step bunches separated by atomically flat terraces.

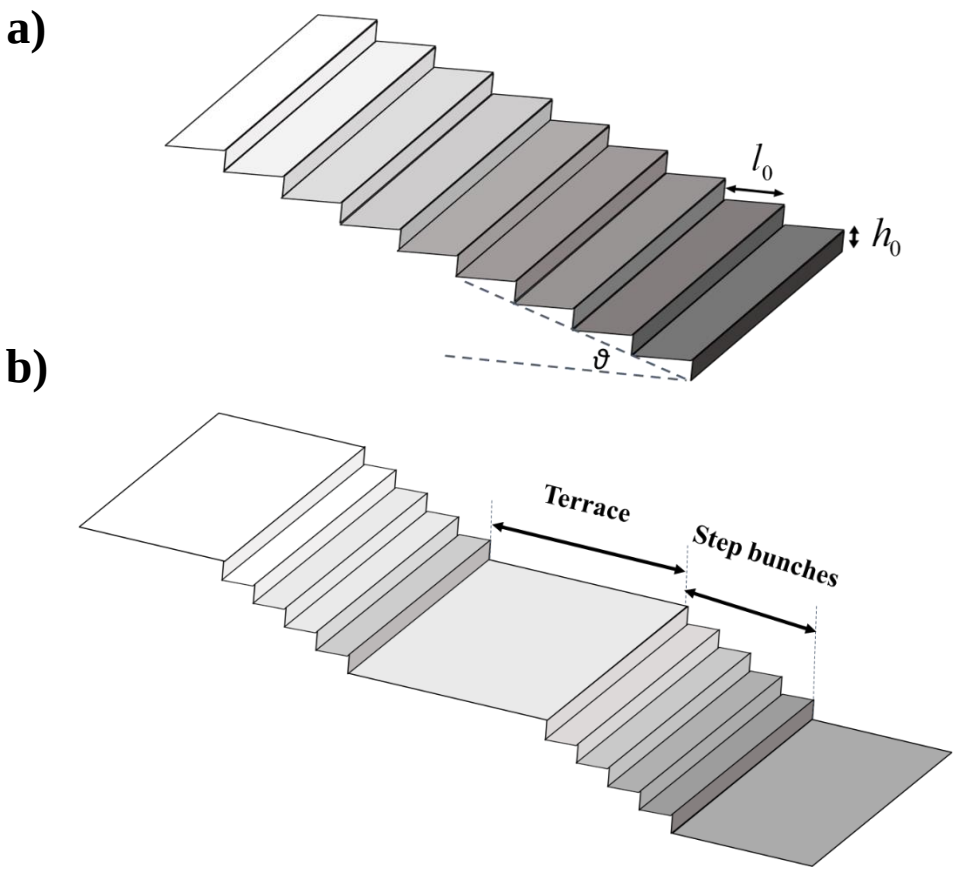

Figure 2.1: Vicinal and bunched surfaces

(a) A schematic of a vicinal surface. The miscut angle, initial step height h_0 and initial terrace width l_0 can be expressed by tan $\vartheta = h_0/l_0$. (b) A schematic of step bunched surface with preserved miscut angle ϑ. The atomically flat terraces are separated by step bunches.

2.1.1 Silicon

Bulk silicon has diamond cubic crystal structure with 8 atoms per conventional cubic cell with a lattice spacing of 5.431Å and a bond length of 2.352Å as shown in the ball and stick schematic of the unit cell of Si in figure 2.2(a). The Si(001) and Si(111) surfaces are the most widely used in the industry. Figure 2.2(b) shows the ideal bulk terminated Si(111) surface structure. In this figure larger circles represent atoms in the top surface layer with one dangling bond pointing up into vacuum, while the smaller circles are the atoms in the second layer. The Si(111)-(1x1) surface unit cell is highlighted in light orange in both figures. This bulk termination is not stable and after thermal treatment above 670˚C the (111) surface converts to more stable (7x7) Takayanagi type reconstruction [53], and at temperature in excess of 850˚C becomes a disordered (1x1) phase [54-56]. The Si(111) surface and the variety of reconstructions related to the (7x7) phase have been intensively studied in surface science, but great scientific interest was added after the "Electromigration" driven phenomena on Si(111) was discovered by Latyshev *et al* [22].

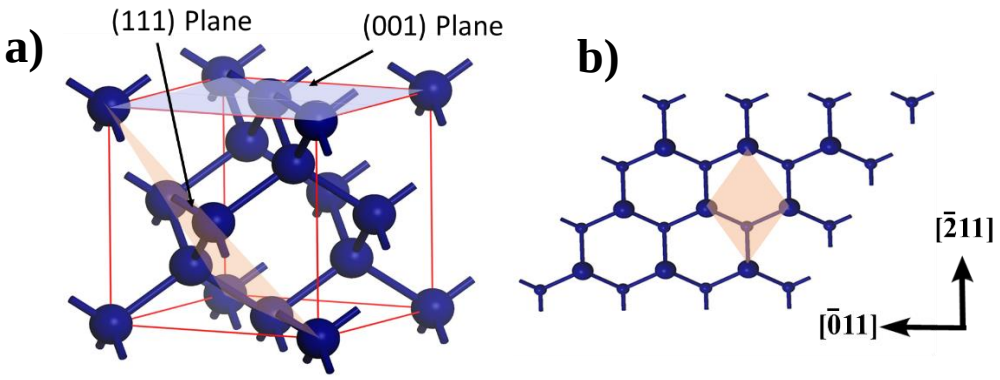

Figure 2.2: Silicon structure

(a) Ball and stick model of the crystalline Si unit cell with the (001) and (111) planes highlighted by the light blue square and the pink square, respectively. (b) Unreconstructed Si(111) surface (*i.e*. 1x1). The light orange diamond outlines surface unit cell, which can be identified in (a). These images reproduced from [57].

Vicinal Si(111) cut in either the $[11\bar{2}]$ or the $[\bar{1}\,\bar{1}\,2]$ by 1-4˚ is used in this study. These two off-cuts are not totally equivalent because on an unreconstructed surface they have an inequivalent number of dangling bonds as demonstrated in figure 2.3. The off-cut in the $[11\bar{2}]$ direction has twice the number of dangling bonds at the step edge.

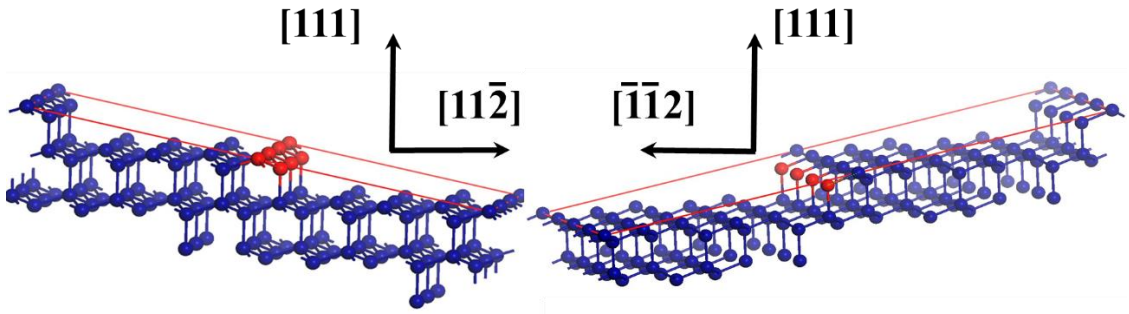

Figure 2.3: Single atomic steps on Si(111)

Inequivalent vicinal (111) surfaces cut in the $[11\bar{2}]$ (left) or the $[\bar{1}\,\bar{1}\,2]$ (right) directions. The step-edge atoms, highlighted in red, have a different termination and number of dangling bonds in each case. These images are taken from [57].

2.1.2 Sapphire

Crystal Structure

Sapphire or α- Al_2O_3 crystallizes in a hexagonal structure with a rhombohedral primitive cell. It is an electrical insulator and chemically non-reactive. It has a high melting point (≈ 2070 ˚C) and is transparent between 0.45–6.5 eV. In the hexagonal unit cell the lattice vectors of the basal plane (a_1, a_2, and a_3) are equivalent to 4.758 Å, with an angle of 120˚ between each, while the vertical lattice vector d has a length of 12.992 Å. Aluminium (Al^{3+}) cations fill 2/3 of the octahedral sites and oxygen (O^{2-}) anions form a distorted hexagonal close-packed lattice. The oxygen presence in octahedral interstices permits strong bonding which lends the material its hardness and electrical insulation properties.

The most commonly encountered planes of sapphire are shown in figure 2.4(a). C-plane (0001) sapphire is the most widely used among these planes because it is the most stable (lowest surface energy). Figure 2.4(b) shows the crystal structure of this C-plane surface. There are three different terminations possible on the (0001) surface, each exposing a different surface crystal structure. It can be an oxygen layer, a double aluminium layer or single aluminum layer, which turns out to have the lowest surface energy [59]. The separation of two neighboring planes of oxygen atoms is given by *d*/6, i.e. one-sixth the unit cell, which equals to 2.1 Å.

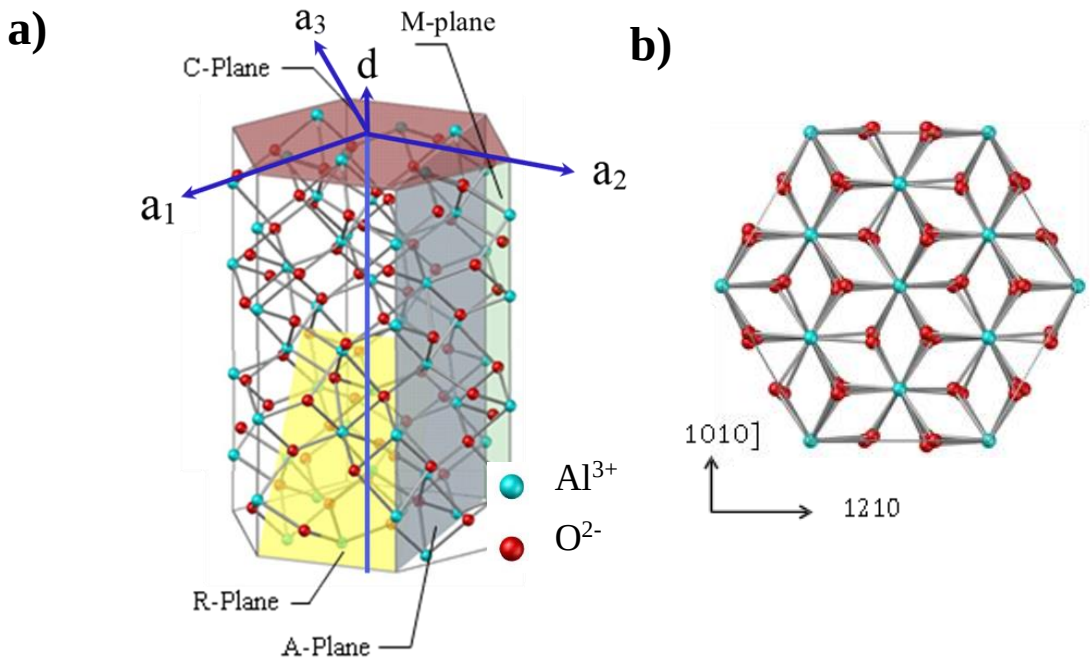

Figure 2.4: Sapphire structure

(a) Primitive unit cell of C-plane α- Al_2O_3 with four most widely used planes indicated as follows. Red: C-plane (0001), green: M-plane $(1\bar{1}00)$, yellow: R-plane $(1\bar{1}02)$, and blue: A-plane $(1\bar{2}10)$. (b) The C-plane surface of sapphire with aluminium (blue) and oxygen (red). These images are taken from [58].

Faceting Mechanism

Faceting is a process by which a surface decomposes into two or more planar surfaces. The formation of facets on single-crystal α- Al_2O_3 surfaces begins with the creation of 0.2 nm high steps. These steps show a preference for existing as pairs: the pairs then bunch together and form facets which are typically multiplies of *c* (c=1.3 nm) in height [60]. Previous studies have investigated the surface evolution of sapphire as a function of a variety of annealing parameters, such as temperature [61, 62], time [60, 63], atmosphere [64], pressure [61] and miscut angle [65]. Annealing vicinal C-plane α- Al_2O_3 substrates in air in the 1000-1500 ˚C temperature range for several hours, by irradiative heat, creates a step-and-terrace morphology with wide terraces (several hundreds of nm) separated by steps (1-5nm) [61, 66]. The duration of the step-bunching phase before faceting initiates is found to depend on a number of parameters, including miscut angle ϑ, with a higher miscut angle corresponding to a longer duration of step-bunching [67]. This step-terrace formation has been attributed to faceting of the surface. Studies of annealing at higher temperatures (>1500 ˚C) produced dendritic structures on sapphire [68]. The figure 2.5 taken from a PhD thesis by Dr O. Ualibek [69] shows the results obtained on stepped sapphire templates after annealing at temperatures between 1350-1550 ˚C for 15 hours. As can be seen in figures 2.5(a) and (b), the surface appears highly uniform with a step periodicity of 100 ± 17nm. The dependence of periodicity as a function of the annealing temperature is demonstrated in figure 2.5 (c). Here, the step periodicity increases with annealing temperature, which is in agreement with other studies [62, 70]. This faceting mechanism can be considered to be a thermally activated diffusion process in which the periodicity of the steps is assumed to be equivalent to the average adatom displacement, *D* [62]. In this case, the relationship between *D* and temperature (*T*) can be given by the Einstein equation:

$$D = D_0 \exp\left(-\frac{E_{ac}}{k_B T}\right) \tag{2.1}$$

where E_{ac} is the activation energy and k_B is the Boltzmann constant.

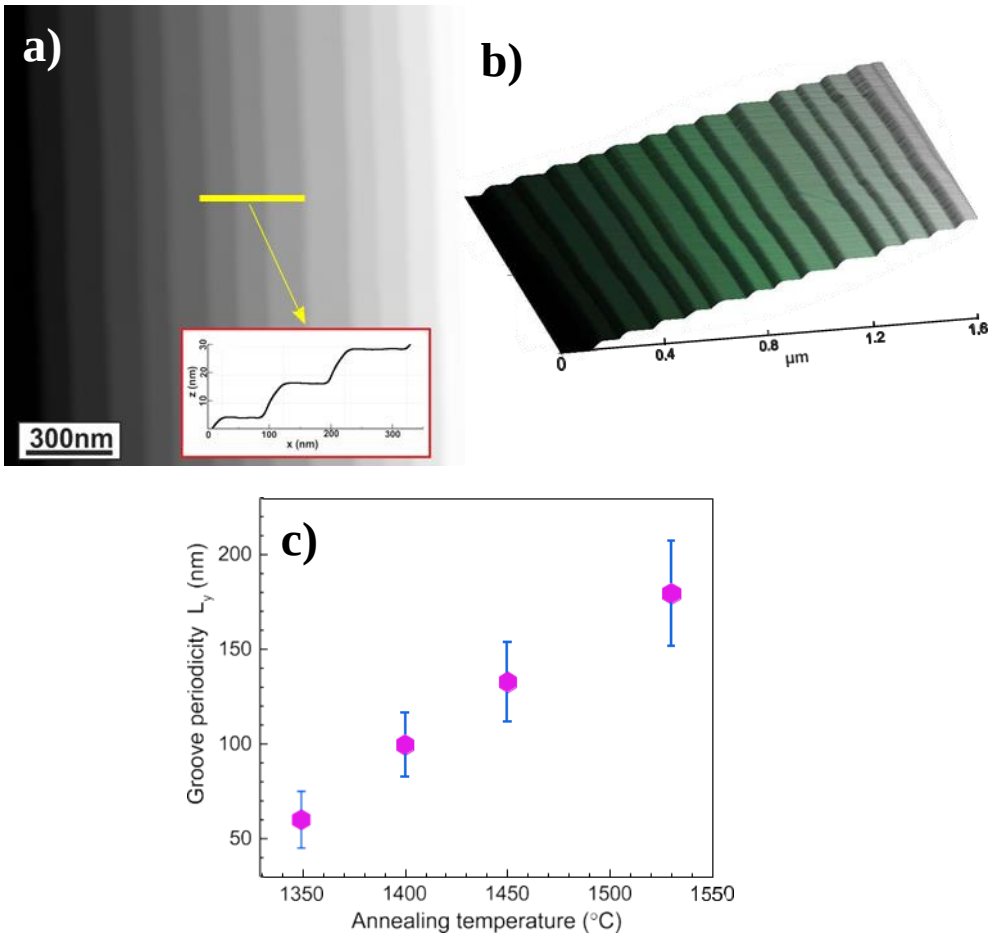

Figure 2.5: Sapphire annealing at high temperatures

(a) AFM image of Al_2O_3(0001) surface after annealing in air for 15 hours at 1400 °C. This surface is offcut by 6° towards the $[1\bar{2}10]$ direction. Inset, line profile showing the step heights. (b) The 3D view of the faceted sapphire surface. (c) Dependence of step periodicity of annealed samples on temperature. These images are taken from [69].

Faceting of Al_2O_3 surfaces can be explained by different models. A model proposed by Marchenko involves an attractive elastic forces to produce the periodic step arrangement [71]. In his model, the constraint of conservation of the average surface orientation suggests the coexistence of alternating directions. The strains are unbalanced at the intersections between different facets resulting in the formation of elastic forces which will propagate into the bulk. These structures are found to exhibit an optimum period

corresponding to the minimum of the surface free energy of the system. Another possible mechanism responsible for the faceting is the entropic contribution of step wandering and repulsive stress-mediated interactions [72]. In this model it is suggested that most faceting transitions occur as the result of competing free energy curves induced by surface composition changes due to adsorption or reconstructions.

However the faceting behavior of the sapphire surfaces still remains unclear and the actual cause is likely to be a complex interplay between the mechanisms described above. Deeper investigations are required to explain the surface evolutions towards the faceting formation.

2.1.3 Tungsten

Tungsten has a body centered cubic (bcc) structure as represented in figure 2.6(a). In this thesis W(110) was studied which has centered rectangular surface structure with lattice parameters of 3.16 Å and 4.47 Å in the [001] and [$\bar{1}$ 10] directions respectively as shown in figure 2.6(b). W has the highest melting point of all metals (3422˚C) [73].

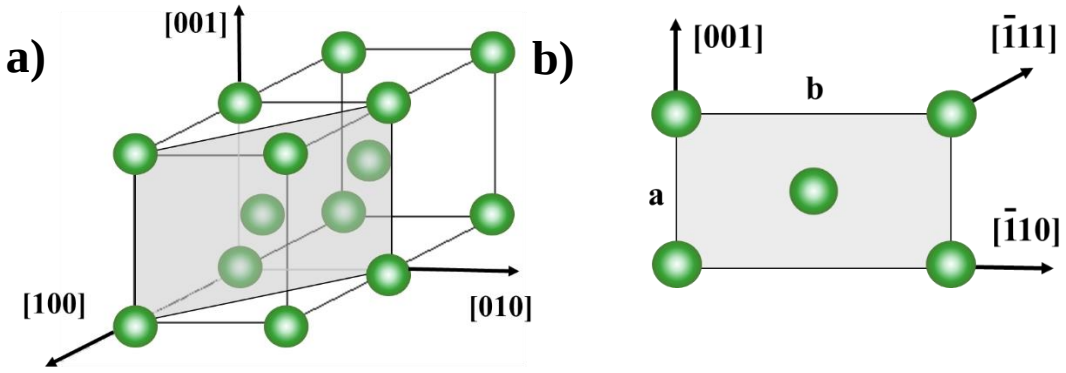

Figure 2.6: Tungsten structure

(a) The unit cell of bcc Tungsten, with the (110) plane highlighted in grey. (b) W(110) surface.

STM image in figure 2.7 (which is taken from ref. [74]) shows the clean W(110) surface with primary crystallographic directions indicated by arrows. The clean W(110) surface consists of large single atomic height terraces with an average width of approximately 100 nm.

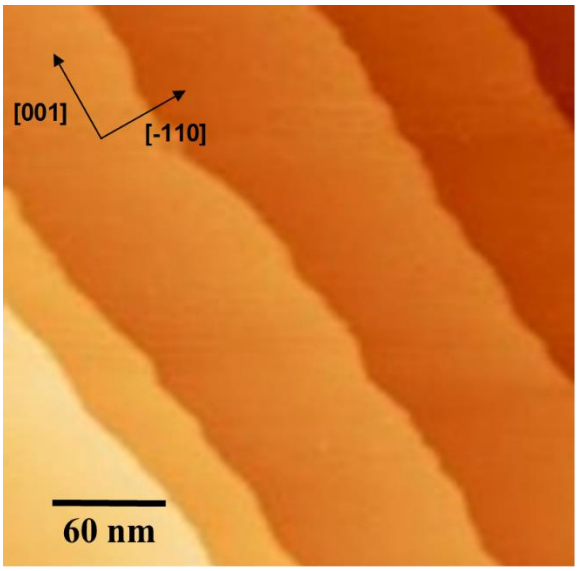

Figure 2.7: Atomic steps on W(110)

STM image of the clean W(110) surface taken from the thesis of S.R. Vadapoo [74].

The possibility of a lateral reconstruction was critically discussed for a long time [75] and led to the conclusion that the clean W(110) surface is unreconstructed [76]. In the presence of a rigid displacement of the (110) surface along the $[\bar{1}10]$ direction brings the surface atoms from a two-fold coordinated position to a three-fold one as shown in figure 2.8. These images are adapted from a figure in a publication from 1983 by Chauveau *et al*. [76]. The stability of the unreconstructed state of the clean W(110) surface, without adsorbed hydrogen, was confirmed by experimental [76-78] and theoretical studies [79].

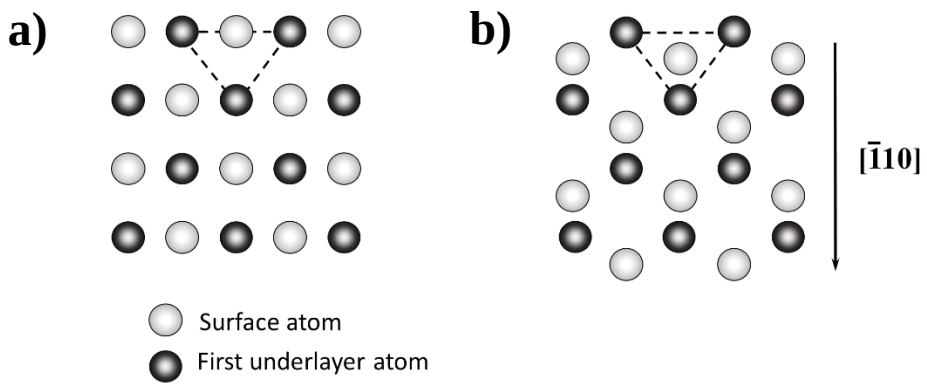

Figure 2.8: Reconstruction of the W(110) surface

(a) Unreconstructed surface with surface atoms in bridge positions. (b) Reconstructed surface with surface atoms displaced in the [1$\bar{1}$0] direction relative to the second layer, in the presence of hydrogen, and going to ternary positions.

The W(110) surface has been studied in ultra-high vacuum (UHV) and an oxygen atmosphere with low energy electron diffraction (LEED) and scanning tunneling microscopy (STM) in the range 293 to 2500 K [80]. Reconstruction was observed on the oxygen covered (110) surface.

2.1.4 Spinel

The normal spinel ($MgAl_2O_4$) structure consists of oxygen anions in a distorted face centered cubic (fcc) arrangement with Mg^{2+} cations occupying 1/8 of the tetrahedral interstices and Al^{3+} cations occupying 1/2 of the octahedral interstices [82]. The unit cell length of $MgAl_2O_4$ is 8.075 Å at 25 °C (figure 2.9). The stacking sequence of the planes in the [100] direction can give rise to two different bulk surface terminations: a termination consisting of two Mg atoms per unit cell or alternatively a termination consisting only of O_8 and Al_4 atoms (see figure 2.9). Both (100) terminations are polar and for the Mg–terminated layers, the Mg^{2+} cations fill tetrahedral interstices along either [011] or [0$\bar{1}$1] direction as shown in figure 2.10(a) and (b), respectively. Also the Al^{3+} cations, in consecutive O_8–Al_4 terminated layers form rows along either the [011] or [0$\bar{1}$1] directions as demonstrated in figure 2.10(c) and (d), respectively. The surface energy of these

different terminations have been calculated in the literature [83, 84]. Massaro *et al*. performed empirical calculations of the surface configurations at 0 K of the (100) face of spinel and found that the Mg-terminated configuration has a surface energy of 1.596 J m^{-2}, while Al-O-terminated (100) one has a surface energy of 2.161 J m^{-2} [85].

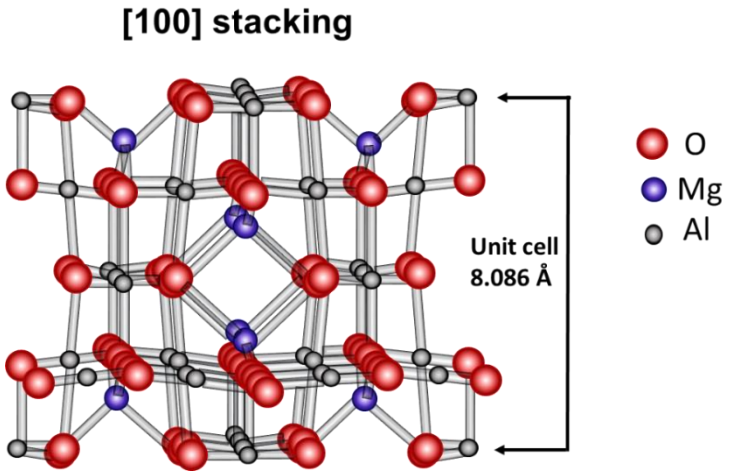

Figure 2.9: Crystal structure of $MgAl_2O_4$

The ball model of the bulk structure of $MgAl_2O_4$ spinel showing the stacking in the [100] direction. O^{2-} anions form a fcc cubic lattice with Mg^{2+} cations in tetrahedral coordination and Al^{3+} cations in octahedral coordination.

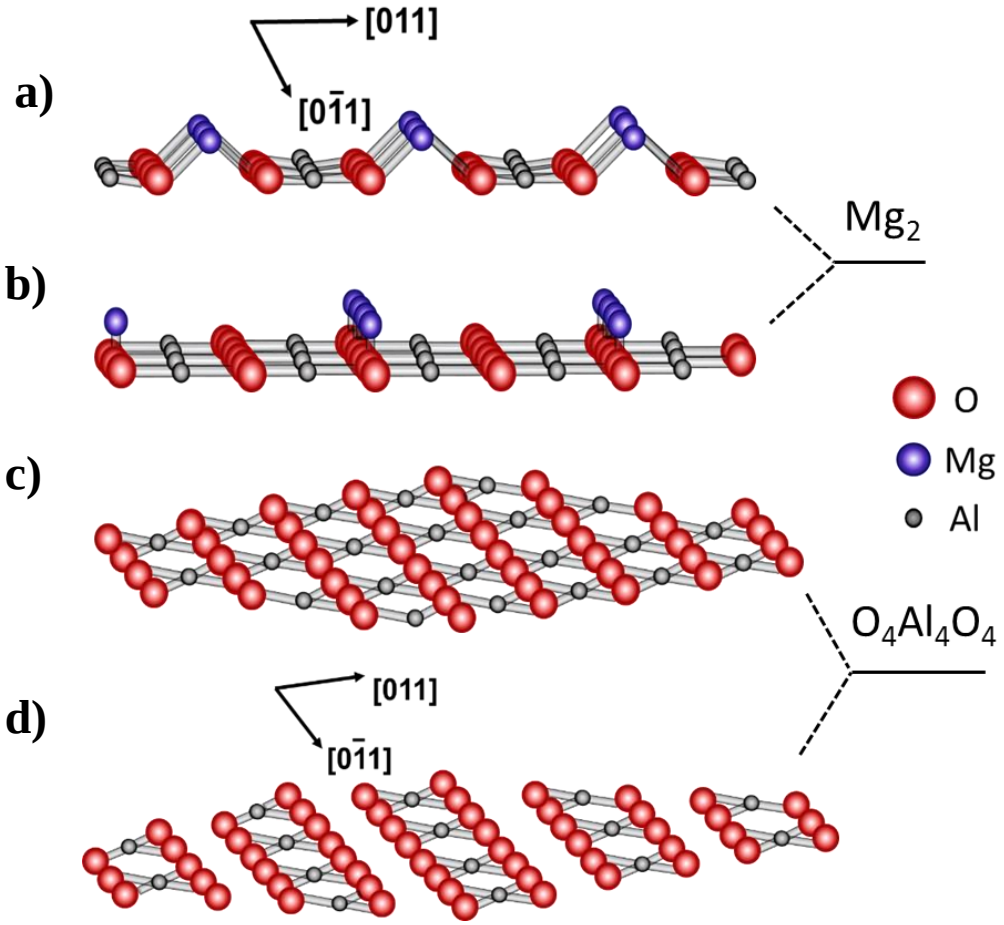

Figure 2.10: Bulk surface terminations of $MgAl_2O_4(100)$

Spinel (100) surface layers produce two different terminations by forming a Mg or O_4–Al_4–O_4 terminated surface. ((a) and (b)) The edges of tetrahedral interstices filled by the Mg^{2+} are aligned along the [011] and [0 $\bar{1}$ 1] directions in the upper and lower (100) layers, respectively. ((c) and (d)) Al^{3+} cations fill octahedral interstices in the upper (100) layer along the [011] direction, and lower layer along the [0 $\bar{1}$ 1] direction. In the bulk, these planes are separated by a distance of 2 Å.

Recently, atomic-scale studies have been performed to determine the surface structure of $MgAl_2O_4(100)$ by using atom-resolved non-contact atomic force microscopy (NC-AFM) [84, 86]. The surface of spinel $MgAl_2O_4(100)$, when prepared under vacuum conditions, adopts a structurally well-defined O_4–Al_4–O_4-termination consisting of Al and double-O rows, which are interrupted by defects identified as interchanged Mg in the surface layers [87]. This finding implies that so-called Mg-Al antisites, which are defects in the bulk of

spinel, become thermodynamically stable and integral part of the surface. The polarity can be abolished by removing a certain percentage of atoms in the surface layer [88]. The surface vacancies will then most likely re-organize and lead to a surface reconstruction in order to satisfy the polar stabilization criteria [89]. A balanced non-polar surface may exist if the Mg has half occupancy in the Mg-layer (Mg 50%) termination, which can be achieved by the surface adopting a (2x2) reconstructed unit cell [91]. Among the non-polar stoichiometric surface terminations, the Mg-terminated (100) surface is considered to be the most stable [90]. Jensen *et al*. revealed that the surface structures obtained at temperatures ranging from 800 °C to 1200 °C is sensitive to the exact preparation conditions and the resultant surface structure can be explained by different stabilization mechanisms which predominate for different annealing temperatures [91].

2.2 Electromigration

Electromigration is a mass transport phenomenon driven by an externally applied electric field. In practice, an electric current flows through a conducting solid resulting in a migration of ions and point defects within the material. Metallic electromigration along interfaces and grain boundaries plays a crucial role in the failure of metallic interconnects in integrated circuits [92, 93].

A number of studies have examined the changes in surface morphology that can be brought about through electromigration [50, 51, 95]. The scientific interest to this phenomenon is further stimulated by the discovery of electric-current-induced step bunching on vicinal Si(111) [22, 95].

It is generally accepted that step bunching on Si(111) is caused by the surface drift of Si adatoms in the direction of the current flow[12]. This drift results from electromigration force acting on the adatoms, which may be expressed as:

$$F = q_{ef} E \tag{2.2}$$

where q_{ef} is the adatom effective charge and *E* is the applied electric field [49, 92]. The effective charge can be thought of as the sum of two charge terms:

$$q_{ef} = e(Z_{el} + Z_w) \tag{2.3}$$

where *e* is the elementary charge, Z_{el} describes the direct force arising from electrostatic interactions between the atom and the electric field and Z_w is the so called "wind" term charge which describes the force on the adatom due to the collisions with the flow of charge carriers. Depending on the position of atom and the effect of screening due to current carriers, Z_{el} lies in a range from zero to the atomic valence, while Z_w is the output of the number of current carriers, their mean free path and the cross section of the adatom.

The value of q_{ef} can be rather easily calculated for the case of an adatom on a surface of a different material by examining the rate of drift. However, for adatoms migrating on a surface composed of the same material (such as Si adatoms on the Si(111) surface), the calculation of q_{ef} is more problematic. [25, 96-98].

It is suggested that electromigration on metallic surfaces is mainly driven by the electron wind, while for both semiconductor and insulating surfaces the direct electrostatic force, acting on diffusing adatoms, is primarily responsible [49, 92].

2.3 Step Bunching on Si(111)

Step bunching in Si can be brought about by driving an electric current through Si(111) which has a small miscut (typically <6˚) in the $[11\bar{2}]$ direction. In the present study we consider cases where the electric current is applied perpendicular to the step-edges, either in the "step-down" $[11\bar{2}]$ direction, or the "step-up" $[\bar{1}\,\bar{1}\,2]$ direction. The step bunches produced grow with annealing time and can reach tens to hundreds of nanometres in height, while the atomically flat terraces between the bunches can grow to several microns in width.

As mentioned in the previous chapter (section 2.1.4), the first observation of step bunching on Si(111) was made by Latyshev et al. who also found that the final state of step bunches depends on the current direction [22]. In this case there are currently four temperature regimes as following: Regime I from 850-950˚C, Regime II from 1040-1190˚C, Regime III from 1200-1300˚C and Regime IV from 1300˚C upwards.

Regime	Temperature	Step-up *E* field	Step-down *E* field
I	~850˚C – 950˚C	Regular	Bunched
II	1040˚C – 1190˚C	Bunched	Regular
III	1200˚C – 1300˚C	Regular	Bunched
IV	>1300˚C	Bunched	Regular

Table 2.1: Step bunching temperature regimes on Si(111)

Presence of step bunching on vicinal Si(111) surfaces for 4 different temperature regimes.

These regimes are summarized in table 2.1. Bunching of steps can occur with a step-up current in the temperature regimes I and III, while step-down current is necessary for temperature regimes II and IV [22, 99]. When the current is applied in the opposite direction to that required to produce step bunching, the result is a regular array of steps of atomic height which is stable against step bunching. However, during cooling to room

temperature some bunching may occur, resulting in steps having a periodicity on the order of tens of nanometers [58].

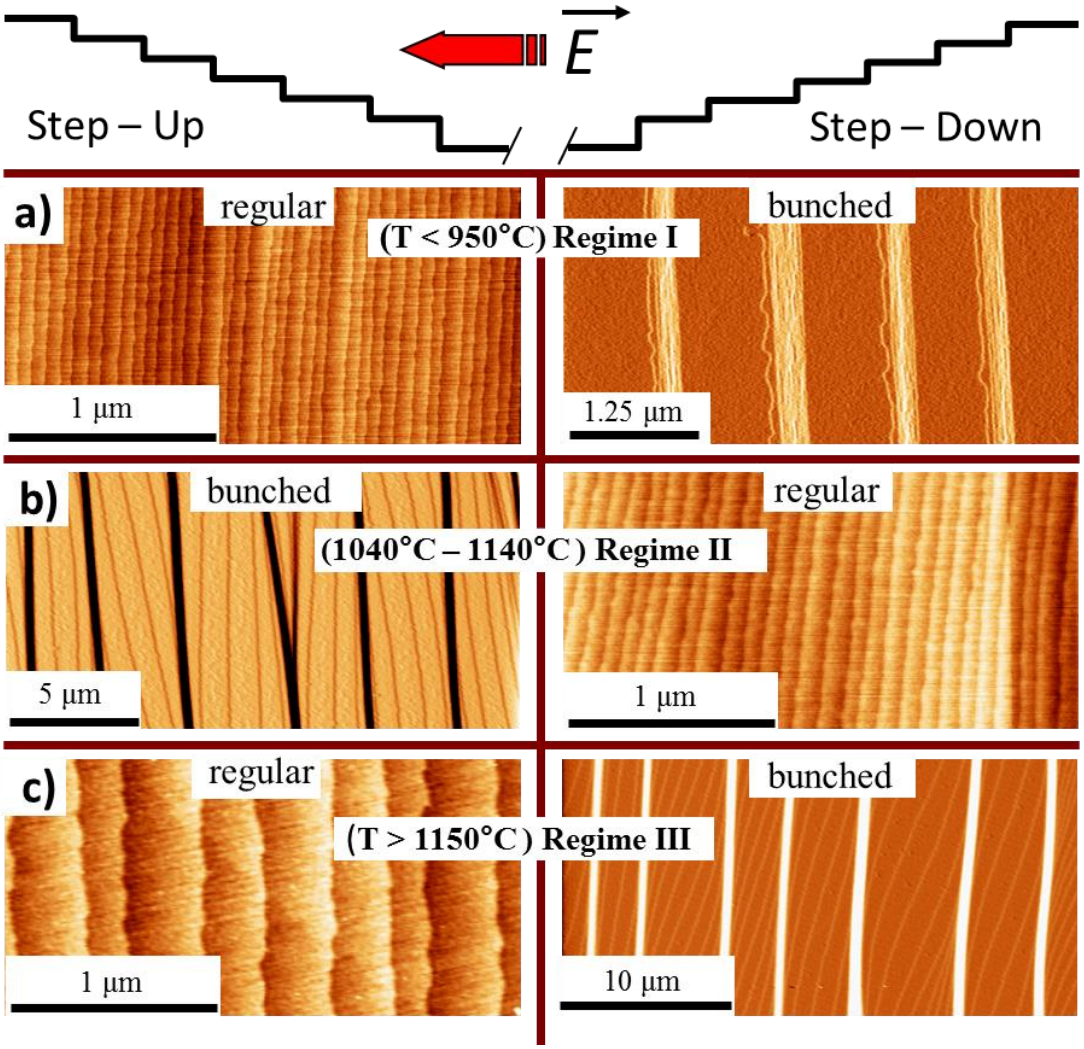

Figure 2.11: Step bunching behavior on Si(111)

The direction of the electric field relative to the step-up and step-down directions is indicated schematically view above the figure, and the corresponding the AFM images are shown directly below. The red arrow represents the direction of the current. Images (a)-(c) show the formation of step bunches in three for the four different temperature Regimes. These AFM images taken from the PhD thesis of Brian J. Gibbons [100].

The effect of temperature and current direction on the formation of step bunches is illustrated in figure 2.11 (which is taken from [100]). The schematic above the images demonstrates the step-down (right) and step-up (left) current directions corresponding the images below where the red arrow indicates the DC direction. Heating vicinal Si(111) with the *E*-field in the step-down direction in Regime I leads to the formation of step bunches, while when annealed with the applied field in the step-down direction, the result is smaller steps with a uniform distribution (see figure 2.11(a)). In the right-hand side of figure 2.11(a), the step bunches are identified as the bright regions and the darker areas are terraces separating the step bunches. In Regime II, the required directions of applied field to induce step bunching or regular atomic step arrays are the opposite to those required in Regime I, as shown in figure 2.11(b). Finally, in Regime III, a step-down E-field is required to induce step bunching (fig. 2.11(c).

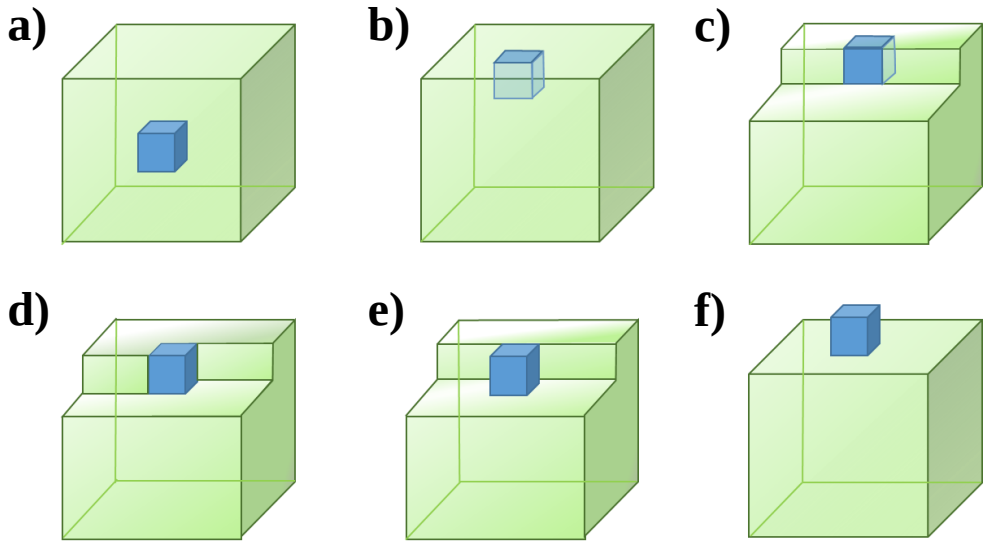

Figure 2.12: 3D cubic model of atom locations

Schematic showing the simple cubic model of an atom (blue cube) on or in a crystal. The images (a)-(f) are organized in order of decreasing number of saturated bonding sides.

It is essential to define the basic mechanisms used to characterize the movement of surface atoms in all regimes. This can be achieved using a simple cubic model which is presented in figure 2.12. The images (a)-(f) are organized in order of increasing number of dangling bonds which corresponds to an increasing free energy. A single atom in the system is demonstrated by blue cube. The lowest possible energy state for an atom is when the atom encapsulated within the solid as shown in figure 2.12(a). In figure 2.12(b) the atom forms part of the surface crystal where five of its bonding sites are saturated, i.e. incorporated into a solid. Figure 2.12(c) shows the atom as a part of step edge running across the crystal surface. The atom in figure 2.12(d) is located at a kink in the step edge and is exposed on 3 sides, while in figure 2.12(e) it is attached to a step edge. Finally in figure 2.12(f) there is a solitary atom on the surface, known as an adatom. When energy is supplied to an atom (typically in the form of heating) it may move between 6 states, preferably to a lower energy state as described by figure 2.12. The supply of heat may also cause the desorption of atoms from the surface, corresponding to a further increase in free energy.

2.4 Step Bunching Theories

The step bunching behavoiur on Si(111) has long been theoretically studied which will be discussed below. However, due to the fact that electromigration-induced step-bunching on insulating and metallic surfaces has so far not been observed, there are no theoretical frameworks to describe such phenomena.

Silicon

The first model which accounted for the *E*-field induced adatom drift was proposed by S. Stoyanov [23] which was the modified the BCF (Burton Cabrera Frank) [102] theory of crystal growth. It considers adatoms with an average drift velocity of

$$v_{drift} = \frac{D_s F}{k_B T} \tag{2.4}$$

where D_s is the coefficient of surface diffusion, k_B is the Boltzmann constant, T is temperature and F, which is given by

$$F = q_{ef} E \,, \tag{2.5}$$

is the electromigration force acting on adatoms [102, 103]. While this is a simple 1D model, it is a good approximation for the behavior of adatoms on a vicinal Si(111) surfaces as the step-bunches are normally quite straight and parallel. The model proposed by Schwoebel [104] also adapts the BCF theory, where attachment/detachment of atoms at surface steps is considered to occur with a certain probability. However, in contrast to the Ehrlich-Schwoebel effect [104, 105], the influence of electromigration force can be controlled by manipulating the *E*-field applied through the crystal.

The following is a qualitative description of how the dynamics of adatoms can lead to step bunching, by incorporating the concepts of electromigration, attachment/detachment and adatom concentration [23]. In figure 2.13(a) the adatoms (blue circles) under the influence of an external force *F* can diffuse/desorb in the direction of arrows. This figure is adapted from an image in Ref. [23]. Steps on the surface have a limited capability to release and receive atoms. There is a short, yet finite time associated with the departure of atoms from step-edge A, and similarly adatoms released from A are not instantly accepted by site B. This results in higher concentration of adatoms close to B as illustrated in figure 2.13(b). Thus a backwards diffusion of adatoms towards A is induced, which retards the retreat of step A. If the distance AB is wider than the average step-egde to step-edge distance (or periodicity), then the adatom gradient will be weaker. As a result the back-diffusion of adatoms corresponding to this gradient will be lower than elsewhere on this surface, and so the net flux of adatoms towards B will be greater. This causes larger than average terraces to increase in width, while smaller terraces will shrink, leading to step bunching. When the force *F* is applied in the opposite direction, the effect of the gradient is to stabilize terrace width and prevent step bunching.

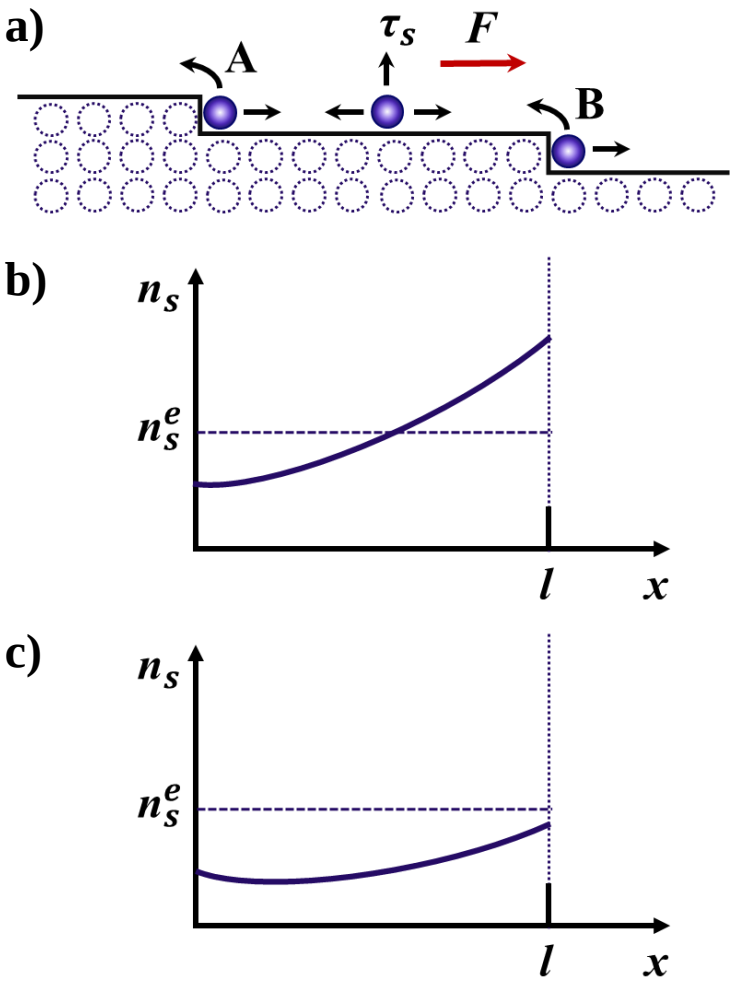

Figure 2.13: Adatom motion and concentration

(a) Detachment of adatoms from a step edge (at A or B) followed by surface diffusion in a direction of the applied external force *F*. This movement may involve of desorption of adatoms. The label τ_s indicates the average time for adatom desorption on the flat terrace. (b) Schematic illustration of the adatom concentration n_s along the terrace of the step which has the length *l*. The label n_s^e indicates the equilibrium value for adatom concentration across the entire terrace. The concentration close to B increases causing a back diffusion, which offsets the flux of adatoms towards B. (c) Under substantial desorption of the adatoms from the surface, the adatom concentration is below the equilibrium value, n_s^e, over the entire terrace.

In vacuum at higher temperatures there is substantial desorption of adatoms from the surface. That means the concentration of adatoms is lower than equilibrium across the whole step as shown in figure 2.13(c). As adatoms migrate across the step from A to B,

there is a greater probability of desorption where the step-to-step distance is greater. Therefore the arrival rate of adatoms at a step-edge is greater if the width of the terrace preceding it is lower than average. Thus, narrower terraces are inclined to become wider, and vice versa. As a result, the surface maintains a pattern of evenly spaced atomic steps and is stable against step bunching.

If the direction of the applied force is reversed, then the arrival rate at point A will be less for wider terraces, leading to their further growth at the expense of narrower terraces. Thus in this circumstance the electromigration will result in step bunching.

For a quantitative treatment of step bunching, one may follow Stoyanov with the following expression for the surface transport as a starting point [23]:

$$D_S \frac{d^2 n_S}{dx^2} - \frac{D_S F}{k_B} \frac{dn_S}{dx} - \frac{n_S}{\tau_S} = 0 \qquad (2.6)$$

where n_S is the adatom concentration and other terms are as previously described. There are three primary terms in this equation. The first term describes the movement of adatoms by diffusion due to adatom concentration, and the second one expresses the effect of the force due to the presence of the *E*-field. Finally, the third term is related to the lifetime of adatoms on the surface before they are lost to desorption. Further mathematical treatment requires the description of step edges along *x* and the boundary conditions for adatoms at the step edges, but this is a considerable task in itself and is not the main focus of this present thesis.

The steps are assumed to be impermeable or nontransparent in the generalized BCF theory [23, 101], which comfortably describes the step-bunching behavior for step-down adatom electromigration, as for Regimes I and III, it predicts stable surfaces for step-up *E*-fields. The model above, which can explain the surface behavior in Regimes I and III, considers the “non-transparency” of atomic steps when the kink density is high and adatoms hopping onto step must participate in the exchange between 2D gas of adatoms and the crystal phase and attach to the step edge. Stoyanov suggests a separate continuum model to explain the step bunching with a step-up electromigration for regimes II and IV [45]. Within this model, in contradistinction to the generalized BCF model, the steps are

assumed to be (partially) transparent or permeable, which means there is a direct exchange of adatoms between neighbouring terraces. In this case, if the concentration of kinks at the step is low, many adatoms have a chance to attach to the step edge, diffuse along it and detach without attaching to kink position at all. As a result adatoms simply cross the step without the contribution in the exchange between the crystal phase and the migrating adatoms' dilute layer.

Aside from models produced by Stoyanov, other theoretical studies have been put forward to explain the electromigration induced step bunching on Si(111), with varying degrees of success [42-44]. The detailed theoretical discussion of step bunching is not the main focus of this study, as this thesis deals with the investigation of antiband instability which appears on step bunches formed on bunched Si(111). An introduction to antibands shall be given in the following section.

2.5 Antibands

Prolonged annealing time of the Si surface with the DC driven along the miscut direction results in the formation of antibands on terraces between step bunches. Electromigration of adatoms causes steps crossing the wide terraces to twist until they acquire a reversed alignment and form bands with opposite inclination to primary bunches, *i.e.* antibands [30, 100]. The schematic of this morphology is illustrated in figure 2.14, and sample AFM images showing this phenomenon are shown in figure 2.15(a) which is taken from Coileáin *et al.* [109]. There are two mechanisms responsible for the formation of antibands: sublimation spirals and the slow evolution of the shape of the steps crossing the large terraces between the step bunches. The antibands developed by these mechanisms are demonstrated on neighbouring terraces of the bunched surface of an AFM image in figure 2.15(b). The dislocations responsible for the sublimation spirals are relatively rare on the terrace and primarily act as a localized source of crossing steps, which finally develop into antibands. The formation of these antibands, which involves the evolution of atomic steps, is one of the main subjects of the present study.

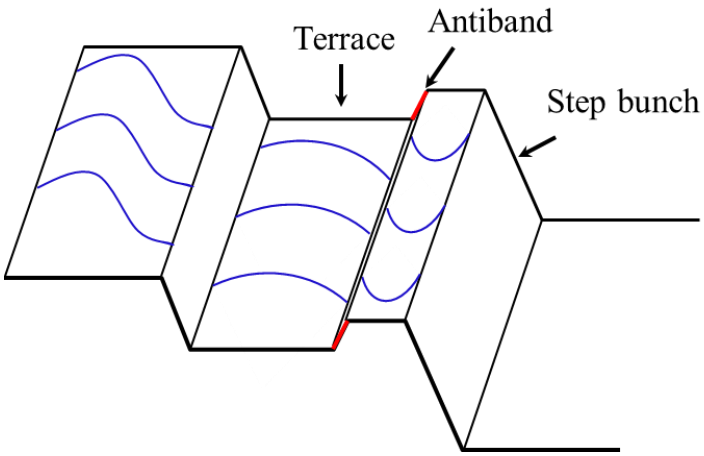

Figure 2.14: Schematic of Antibands

This schematic illustrates a step bunched surface. Anibands (red) are the bunch of steps inclined in the opposite direction as compared to the primary bunches.

Crossing steps on the terrace develop with time as demonstrated in figure 2.16 (a). Variation of the adatom concentration is compensated by the variation of the step curvature. This concentration gradient causes the crossing steps to bend and leads to characteristic S-shape deformation. Also the step velocity near the upper step edge of the terrace is greater than at the lower edge. The crossing step marked by S on terrace 1 in Figure 2.16 (b) demonstrates a symmetric S-shape which aligns perpendicular to the step bunches. As the terrace width grows the inner lobes of the S-shaped steps continue to stretch as shown on terrace 2 in Figure 2.16 (b). Finally, the middle parts of crossing steps align parallel to the step-bunches to create a continuous thick band known as antiband. Terrace 3 in Figure 2.16 (b) clearly demonstrates the final stage of this development.

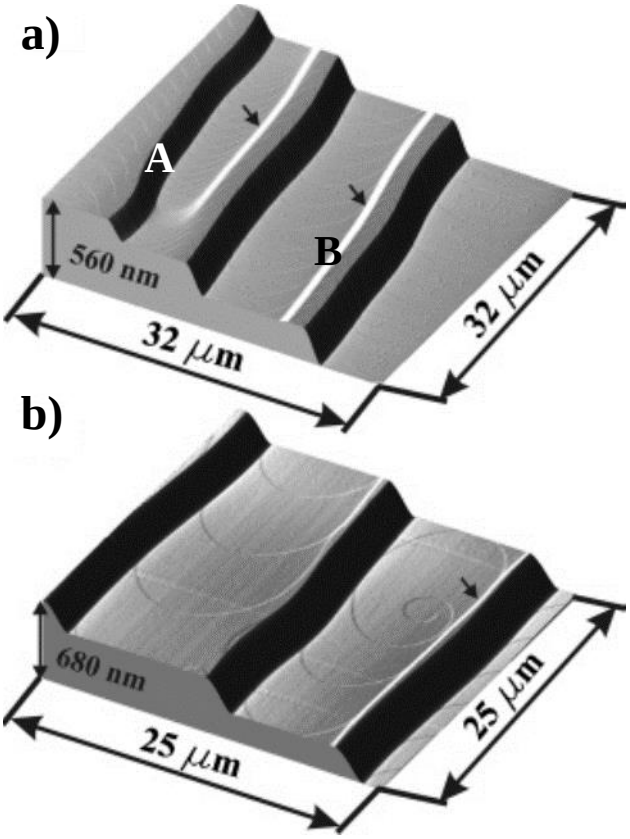

Figure 2.15: Surface morphologies created on Si(111)

(a) AFM phase image overlaid on 3D topographical data for bunched Si(111) surface shows 10 nm (A) and 14 nm (B) high antibands located close to terrace edges. Anibands are white and primary step bunches are black. (b) AFM image of Si(111) shows two neighboring terraces, where antibands evolved by bending of crossing steps (upper terrace) and sublimation spirals (lower terrace) [106].

The minimum limit of the electromigration field in the antiband study can be determined by the critical field, E_{cr}, as applying an electric field weaker than E_{cr} resulted in the cessation of the step bunching process. The studies of Coileáin *et al.* [109] shows that the compressed step-density wave have been created on Si(111) after annealing with the critical field E_{cr} or weaker field and the number of atomic steps is found to be relatively small compared to the coarsening step bunches and is not affected by the duration of annealing.

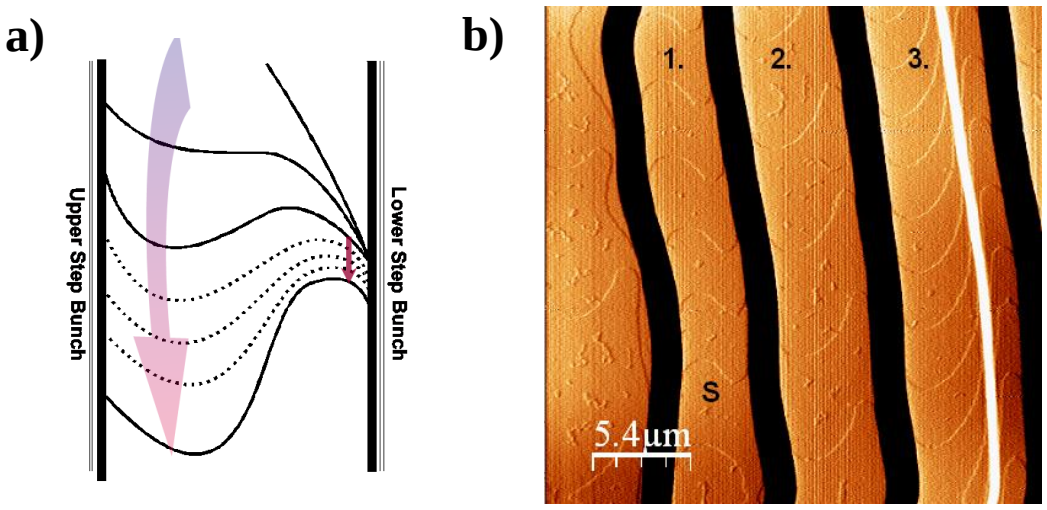

Figure 2.16: Antiband formation

(a) Schematic showing the evolution of crossing steps on a terrace which is progressing in the direction of the arrow. (b) A derivative AFM image shows the different stages of development towards antiband formation. The crossing step is marked S on terrace 1. recognized by its symmetric S-shape. Crossing steps on terrace 2. are beyond the symmetric S-shape. On terrace 3. crossing steps form continuous antibands.

Generally, two groups of processes are responsible for crystal sublimation. The first group involves surface diffusion accompanied by adatom desorption on terraces separated by atomic steps. The second group involves the interaction of adatoms with the atomic steps, i.e. attachment to step edges, migration along the edges to the kink sites, detachment from the kink positions, and detachment from the steps. Depending on the relative rates of these processes, there are two distinguishable sublimation states in the Regime III. First, the attachment-limited state is characterized by relatively slow adatom attachment-detachment kinetics and fast diffusion on terraces. Second, the diffusion-limited state is characterized by relatively slow surface adatom diffusion and fast kinetics at the steps. Since these two sublimation modes are physical distinct, they possess different dynamic properties and must be studied independently.

In this thesis the antiband instability on vicinal Si(111) for the step-down electromigration (Regime III) is investigated. In chapter 4 we provide the theoretical treatment of the antiband instability under the condition of diffusion-limited sublimation.

Chapter 3

Experimental Methods

Оқу - білім азығы,
Білім - ырыс қазығы

This chapter describes the experimental methods and equipment used to initiate step bunching on vicinal samples and to analyse the final surface morphology.

Step bunching on vicinal surfaces has been achieved by following a procedure with three key steps:

1. Thorough cleaning of the initial surface
2. Pre-annealing with no applied electric field
3. Annealing with *E*-field applied perpendicular to the miscut direction.

3.1 Annealing Setup

Step bunching was induced by annealing samples in the ultra-high vacuum (UHV) chamber shown in figure 3.1. The experimental setup was custom designed and developed for the purpose of inducing step bunching. It consists of two separate volumes divided by a gate valve. One system section is kept under constant vacuum at all times by a *Perkin Elmer* ion pump (base pressure of 2×10^{-10} Torr). The adjoining section includes an annealing stage and can be opened to load new samples, with pumping provided by an additional turbo

molecular pump. Three different prototype sample holder designs were tested by Dr Cormac O'Coilean [57] before settling on the current design.

In conventional step bunching experiments, annealing is conducted on a DC joule heating stage, and the temperature of the sample is measured by means of an infra-red pyrometer. However in our case, in order to control the *E*-field applied to the sample, the DC current annealing platform was surrounded by a heating shroud. This allows the surroundings' temperature to be tuned to compensate for any temperature deficit when using lower DC heating current. This configuration not only allows independent temperature control of the sample and the voltage across it, compared to the less-controlled annealing on an open stage, the set-up also provides the added advantage of excellent temperature homogeneity across samples. A schematic of the sample stage in the heating shroud is shown in figure 3.2(a).

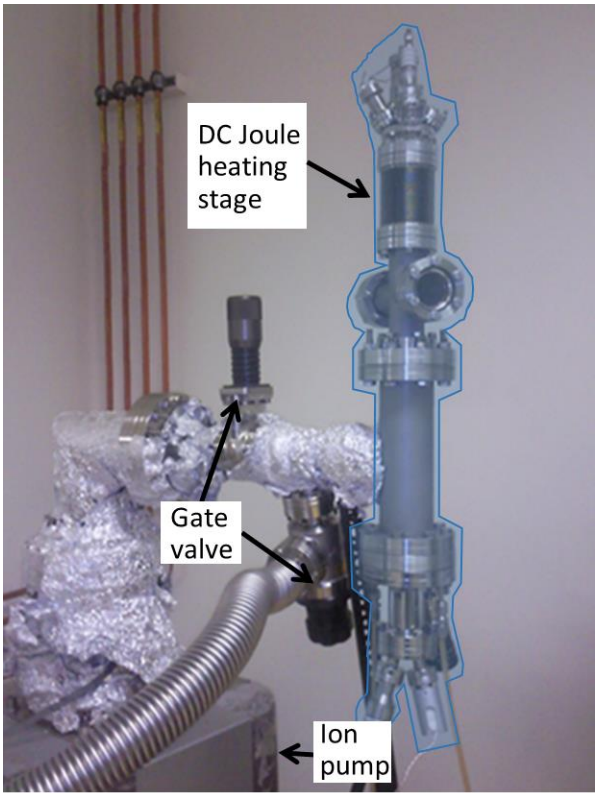

Figure 3.1: Photograph of the UHV chamber containing the sample stage, with its component parts labelled.

The sample holder is designed to anneal samples measuring ~ 20 × 1.5 × 0.5 mm^3. It is possible to anneal samples of other dimensions with a few minor modifications. The purpose-built sample stage is constructed from Mo and ceramic alumina components (figure 3.2(b)) for high temperature vacuum compatibility.

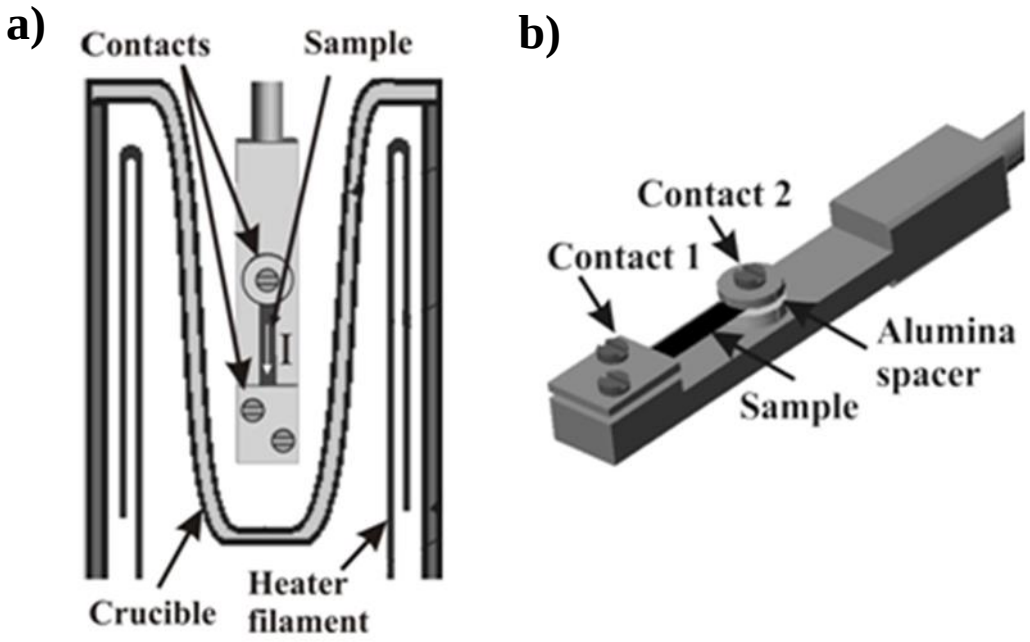

Figure 3.2: A schematic of the sample stage. (a) The sample stage is placed within the alumina crucible of a high temperature effusion cell with a diameter of approximately 10 mm. (b) The sample holder is composed entirely of Mo, W and ceramic alumina components (figure reproduced from [57]).

The annealing platform was built using an effusion cell as its heating source. The sample stage both acts as an electrode and provides mechanical support. The first electrode is clamped in direct contact with the Mo stage. The second electrode is affixed through a hole in the primary stage and isolated using alumina spacers. The sample is held in place using a Ta nut at one end and Ta plate at the other. On the opposite side of the sample holder, the electrode is connected to a 1 mm thick Mo wire, which is insulated with alumina beading. These electrodes are connected through an electrical feed-through to an *Agilent* DC power supply. Once the samples are mounted between the electrical contacts, the entire assembly is inserted vertically into the clean alumina crucible of a Knudsen effusion

cell ("K-cell") made by *MBE-Komponenten GmbH*. The depth of the sample stage inside the crucible can be regulated via a linear drive with a Z travel range of 100 mm. The crucible diameter is only 10 mm, meaning that the operating space is quite restricted and confined, which was the primary limiting factor in the design.

3.2 System Calibrations

Several calibrations and tests were performed by Dr O'Coilean [57] to verify that the measurements taken were secure and consistent. The K-cell is supplied with an attached C-type W5%Re/W26%Re thermocouple (approximate error of 1% between 425°C and 2320°C) located next to the wall of the crucible. This is used to record t_c, the crucible temperature. A second K-type Chromel/Alumel thermocouple (error of 0.75% between 277°C and 1260°C) is inserted with the sample holder to determine whether it was reasonable to use the readout as the temperature at the centre of the crucible (t_k). The temperature measurements were found to agree within an acceptable margin of error and are compared in Table 3.1. Above 1020°C the temperature difference between t_c and t_k vanishes, implying that they can be used as a measure of the sample temperature with confidence.

In order to determine how the resistance of the components changed with temperature, the sample stage was loaded with a piece of Ta foil between the electrical contacts. This was heated to annealing temperature and the resistance was measured using an applied current. The value obtained was $\sim 0.3\,\Omega$. This value remained relatively constant up to the temperatures required for our experiments and was taken into account in determining the voltage drop across our samples.

Long annealing times in UHV can have an unfavorable effect on surface quality and on the step bunching process. To prevent contamination of the surface, several precaution must be taken, as described in section 3.6.

t_c (°C)	t_k (°C)
755	736
862	847
902	892
965	958
1011	1007
1027	1026
1051	1049
1067	1066
1093	1093
1110	1111
1130	1132

Table 3.1: Crucible temperature calibration. t_c is the crucible temperature recorded by C-type thermocouple and t_k is recorded by K-type thermocouple.

3.3 Scanning Tunneling Microscopy

Scanning tunneling microscopy (STM) is a surface imaging technique which provides apparent three dimensional (3D) real space images. It was developed at IBM (Zurich) by Gerd Binnig and Heinrich Rohrer in the 1980s and for this work they were awarded the Nobel Prize in Physics [106]. STM probes the density of states of a conducting material using the concept of quantum tunneling.

When a sharp tip approaches a conducting sample at a distance of $\sim$ 1 nm and a voltage bias is applied between the tip and surface, the so-called tunneling current starts to flow. A piezoelectric tube scanner allows tiny, controlled movements by applying a voltage across the piezos. Thus the electronics of the STM system can control the tip position in such a way that the tunneling current and, hence, the tip-surface distance is kept constant, while at the same time scanning a small area of the sample surface. This movement is recorded and can be displayed as an image of the surface topography.

The STM tip typically has a radius of curvature on the order of several nanometers, however it consists of a number of "microtips" that may each end in a single atom. The

majority of the tunneling effect is due to the closest atom to the surface, and so the most important factor for a tip is the stability of the longest microtip.

The STM can be operated in two scanning modes; constant-current and constant-height. These modes are demonstrated in figure 3.3. In constant-current mode, the tunneling current is kept constant using an electronic feedback loop, while the height is varied, thereby causing the tip to trace out the topography of the surface. In the constant-height mode the sharp tip scans at a fixed height and records the varying tunneling current due to the make-up of the surface and its corrugation. All STM images presented in this thesis were obtained in constant-current mode by my colleagues.

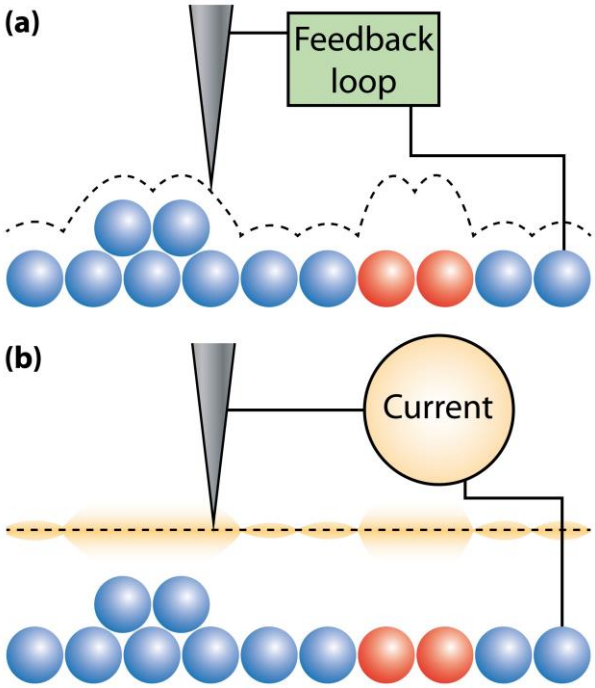

Figure 3.3: (a) STM tip operates in constant current scanning mode. The path followed by the STM tip is shown by dotted line. Substituted atoms (in red) exhibit a different visible height to the blue adatoms due to their different local density of states. (b) Constant-height mode. Tip keeps a constant height over the surface by recording current (shown by orange fluorescence). These images reproduced from the PhD thesis of Dr Barry Murphy [108].

3.4 Low-energy Electron Diffraction

Low-energy electron diffraction (LEED) is a technique which involves measuring the diffraction of electrons by the surface rows of atoms of a single-crystalline material. A collimated beam of low energy electrons (10-200 eV) is directed normal to the surface. The mean free path of electrons in the material is limited to the first few atomic layers, because the electrons have low energy and hence LEED gives information of geometric structure of the surface. When a sample has a well-ordered crystalline surface, the impinging electron beam will be elastically back-scattered by the surface rows of atoms of the crystal back on to a fluorescent screen, resulting in the display of the diffraction pattern of the surface.

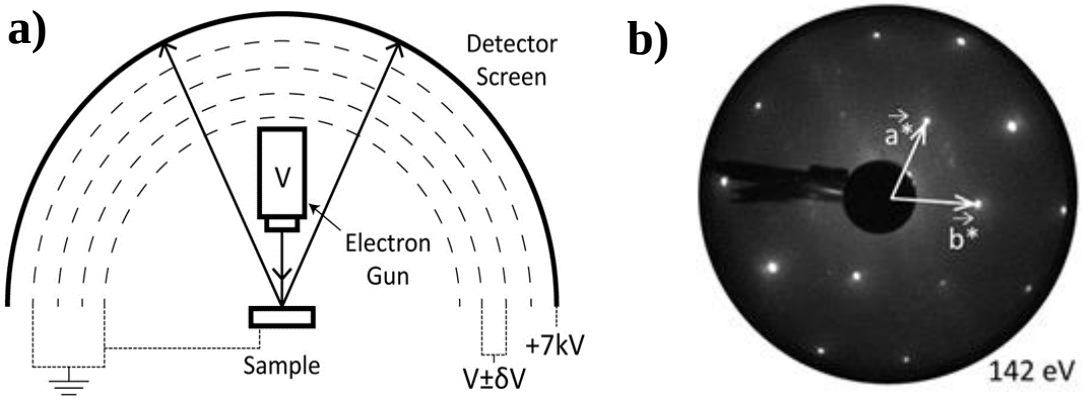

Figure 3.4: A schematic of the experimental LEED setup and a typical LEED pattern. (a) Experimental LEED apparatus. (b) LEED pattern obtained from the clean Mo(110) surface at energy of 142 eV. The indicated a^* and b^* in white arrows are the primitive reciprocal lattice vectors (Images are reproduced from [108]).

A schematic of the LEED apparatus is shown in figure 3.4 (a). An electron gun produces monochromatic electrons, which are accelerated through a voltage *V*, and are diffracted by the sample. These electrons pass four metal grids before colliding with fluorescent screen, where light is emitted. The first and fourth grids are on ground

potential to restrict the field. The central two grids are kept close to V at $V \pm \partial V$ to choose only elastically scattered electrons. Finally, the electron will be post-accelerated by the screen's high voltage, in order to maximize the fluorescence efficiency. Figure 3.4 (b) shows the LEED pattern of the clean Mo(110) surface.

3.5 Atomic Force Microscopy

Atomic Force Microscopy is a surface imaging and analysis instrument designed to represent the atomic-scale topography of a surface by measuring the electronic forces acting between the tip and the sample surface [107].

In general, the principles by which AFM works are simple. The sharp tip scans across a surface in one of two modes: constant height or constant force. Either the height or force between the tip and surface is kept constant while the other is measured. A simple schematic sketch of the working mechanism of an AFM is shown in figure 3.5. The tip experiences the van der Waals forces, dipole-dipole interactions, electrostatic forces, etc. due to its closeness to the surface. A laser is directed at the back of the tip, which is reflective. The reflected light is measured by a collection of photodiodes so that the deflection of the tip can be ascertained precisely. There is a feedback loop which adjusts the tip-sample separation to maintain the scanning mode. The tip moves in a series of parallel lines (this is called rastering) building up a picture of the area as it does. This is then converted into an electrical signal which is interpreted by the computer software.

In this thesis AFM images were obtained with a NT-MDT Solver Pro scanning probe microscope using silicon cantilevers, and the images were processed using NT-MDT Nova and WSxM programs. The radius of the tip is less than 10 nm and the Si cantilever has a nominal resonant frequency of approximately 300 kHz.

The AFM can be operated in three basic scanning modes: contact, non-contact and tapping modes. These modes are introduced in the following sections.

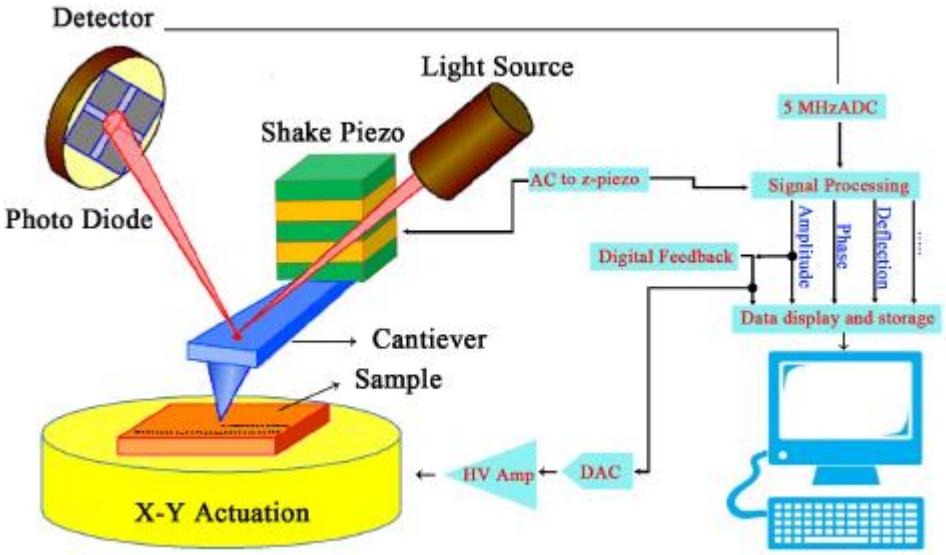

Figure 3.5: Schematic representation of AFM's working principle (Image reproduced from [74]).

3.5.1 Contact Mode

In this mode the tip is “dragged” across the surface of the sample. If the measured deflection differs from the desired value, the feedback amplifier alters the voltage applied to the piezoelectric to return it to the desired set point. However there is a primary problem with this mode of scanning, because the excessive forces applied can lead to damage of the tip or sample. The beneficial part of contact mode is the simultaneous acquisition of topographic and spreading resistance information if both the sample and tip are conductive.

3.5.2 Non-contact Mode

In non-contact mode, the tip of the cantilever does not make contact with the sample’s surface. The cantilever is oscillated above its resonance or maintained at 1-10 nm above the surface where the attractive Van der Waals forces are strongest and act to reduce the resonance frequency of the cantilever. Any changes in the phase, amplitude or frequency of the cantilever can be measured, thus allowing the scanning software to build a topographical image of surface.

3.5.3 Tapping Mode

This mode (also known as AC mode) the cantilever is driven to oscillate with a large amplitude, typically 100-200 nm. If the tip comes close to the surface, the interacting forces such as Van der Waals, electrostatic forces, and dipole-dipole interaction cause the amplitude of this oscillation to reduce as the tip comes closer to the surface of the sample. Scanning with the tapping method overcomes the tip sticking problems which occur in non-contact, and friction problems of contact mode. In the present work only this tapping mode was used.

3.6 Annealing Procedure

Experiments were conducted in UHV using a setup that combines independently controlled direct current (DC) and irradiative heating, with a base pressure of 2×10^{-10} Torr [40].The irradiative heating was supplied by an effusion cell, which surrounds the custom-made direct current annealing stage inserted into an empty crucible.

For Si, the sample temperature was extracted from the sample's resistance, essentially using the sample as a resistive thermometer. The capacity to decouple the DC current from the sample temperature enabled us to control the strength of the electric field while maintaining the sample at a desired temperature. The strongest electric field $E = 3.6$ V/cm was applied to Si samples when the DC was the only source of heating and the weakest field was determined by the critical electromigration field (E_{cr}) [109]. Correspondingly, when the entire heating requirement was supplied by the radiative heater, the applied voltage was 0 V. For the oxides Al_2O_3, $MgAl_2O_4$ and the metallic W, sample temperature was determined by the effusion cell's thermocouple. For these materials, the produced joule heat is negligible and hence did not significantly affect the sample's temperature due to their high or low resistivity, respectively.

Rectangular strips were cut from wafers (Si) or substrates (Al_2O_3, $MgAl_2O_4$ and W) and the samples' long sides were always aligned to the miscut direction. To remove

contamination after cutting, the samples were cleaned with acetone, methanol and isopropanol in an ultrasonic bath. After cleaning, the strips were mounted between the two electrical contacts and lowered into the effusion cell. Before annealing with an applied *E*-field, each sample was outgassed for 24 hours at 700˚C. Finally, after annealing and then cooling to room temperature, the samples were removed from UHV for *ex-situ* analysis of the step bunched surfaces using AFM. Detailed annealing procedures for different samples shall be given in the following sections below.

3.6.1 Si(111)

Samples were sliced in the shape of rectangular 20 × 1.3 mm^2 strips from n-type doped 0.525 mm thick Si(111) wafers (*Siltronix*, resistivity ~ 1Ωcm), with misorientation angles (α) from the Si(111) plane in the range 1.1°-4° towards the $[11\bar{2}]$ direction. To reduce surface defects, the samples were then DC-annealed for 24 hours at a temperature of approximately 450-500˚C, followed by repeated DC flash-annealing up to 1250˚C for 10 seconds. Samples were later annealed for time intervals ranging between 15 and 60 minutes at 1270°C (regime III) with current driven along the miscut in the down-step direction. At this temperature, the Si(111) surface bunches at the high rate of approximately 1 step/second [97] and reaches the phase of antiband formation relatively rapidly, compared to other temperature intervals. Shorter annealing times were used for samples annealed with stronger electric fields.

Prolonged sample annealing in vacuum can result in carbon segregation. Therefore, a separate experiment was set up in order to investigate the extent of surface contamination that could be potentially induced by the described annealing procedure. Auger electron spectroscopy analysis showed that after flash annealing to 1250°C, the surface was free from carbon and oxygen contamination and remained clean after further annealing for 2 hours at 1270°C [40]. After the annealing sequence the samples were maintained at 650˚C for an hour using only radiative heating.

3.6.2 W(110)

High purity W single crystals were grown, aligned and cut at the Institute of solid state physics RAS, Chernogolovka (Russia). High-quality W single crystals grown using the floating zone technique with a low density of dislocations were used for metal step-bunching. To get rid of small angle boundaries and dislocations, the single crystalline ingot was subjected to overcritical plastic deformation followed by a high-temperature annealing, resulting in recrystallization. Crystal quality was monitored by X-Ray diffraction (XRD). The Full Width at Half Maximum (FWHM) of the rocking curves for the (110) reflection (CuK_α) in the XRD experiments was 50 angular seconds. The density of dislocations was estimated to be $2 \times 10^4 cm^{-2}$ [110].

The strips, $10 \times 1.5 \times 0.5$ mm^3, were cut from W(110) with α = 2.6° and 3.2˚ in the $[1\,\bar{1}\,\bar{2}]$ direction and α = 0.8° in the $[1\,\bar{1}\,0]$ direction.

Prior to their treatment in the DC annealing setup, the W(110) samples were cleaned in a separate UHV chamber with a base pressure of 2×10^{-10} Torr. The vicinal tungsten samples were first annealed using electron bombardment at 1300˚C in an oxygen atmosphere ($p=1 \times 10^{-6}$ Torr) for 60 minutes to remove carbon contamination. This was followed by several flash heatings at 2100 ˚C to remove oxygen from the surface. The annealing temperature was measured with an optical pyrometer (*Ircon UX20P*, emissivity 0.35). The pressure in the UHV chamber rose to 1×10^{-8} Torr during the flash heatings but rapidly recovered to 2×10^{-10} Torr after switching off the electron beam. The cleaning process was repeated until the carbon and oxygen impurities could not be detected by Auger Electron Spectroscopy (detection limit is below 1 at. %). Usually, after several cleaning cycles Low Energy Electron Diffraction (LEED) patterns characteristic of vicinal W(110) could be obtained.

As a final preparation step, the W(110) samples were oxidized at 1300˚C in an oxygen atmosphere ($p=1 \times 10^{-6}$ Torr) for 60-90 minutes. This was to protect the surfaces from contamination using a protective oxide layer, so that the samples could be safely removed from the UHV chamber and loaded into the main experimental setup to initiate the step bunching by direct current annealing.

In order to remove the surface oxide layer, the temperature of the effusion cell was brought to 1300˚C and maintained for 1 hour. Next, without radiative heating, a DC of 5A was applied in either the step-up or step-down direction for 24 hours to reduce the density of pinning centers and protrusions. The electric field was applied perpendicular to the orientation of atomic steps. Finally, maintaining the same current direction, the crucible temperature was gradually increased to 1500 ˚C and samples were annealed with direct currents of I = 6 A ($E \approx 0.03$ V/cm), I = 10 A (E = 0.052 V/cm), 12 A ($E \approx 0.06$ V/cm) for 6 hours to initiate the step bunching process. Annealing temperatures of 1500 ˚C were needed to increase adatom mobility and lead to step bunching on the tungsten surfaces.

3.6.2 $Al_2O_3(0001)$ and $MgAl_2O_4(100)$

Samples with size 10 × 1.5 × 0.5 mm^3, were cut from single-crystal, side-polished C-plane Al_2O_3 substrates (99.99% Pure, MTI Corporation, USA) chemically polished (making them UHV compatible) with α = 2˚ and 3˚ in the $[1\bar{2}10]$ direction and $MgAl_2O_4$ (MTI Corporation, USA) with α = 3° and 6˚ in [001] and [011] directions.

To increase the conductivity and adatom mobility, the optimum annealing temperatures of 1400 ˚C and 1500 ˚C were chosen for $MgAl_2O_4$ and Al_2O_3, respectively, and the sample temperature was determined by the effusion cell's thermocouple. The resistance between the contacts was found to be on the order of ~ 30kΩ at 1400˚C and ~ 20kΩ at 1500˚C for magnesium aluminate spinel and sapphire, respectively.

To induce the step bunching process, the α-Al_2O_3 samples were annealed at 1500 ˚C for 6 or 20 hours with electric fields ranging $E \approx 30 – 140$ V/cm and the $MgAl_2O_4(100)$ samples were annealed at 1400 ˚C for 6 hours with electric field, $E \approx 140$ V/cm, applied in the step-down and step-up directions for both insulating surfaces.

Chapter 4

Antiband Instability on Vicinal Si(111) Surfaces

Ілім - жанып тұрған шырақ.
Өнер - ағып жатқан бұлақ,

In this chapter we investigate antiband instability on vicinal Si(111) surfaces with different angles of misorientation. We provide a theoretical description of antiband formation via the evolution of the atomic steps' shape. For the first time we derive a criterion for the onset of the antiband instability under the conditions of sublimation, controlled by slow adatom surface diffusion. We examine this criterion experimentally by studying the initial stage of the antiband formation at a constant temperature of 1270°C, whilst systematically varying the applied electromigration field. The experiment strongly supports the validly of the derived theoretical criterion and indicates the importance of accounting for the factor of critical field in the theoretical modeling of step bunching or antiband instabilities.

4.1 Introduction

The current theoretical model of the evolution of crossing steps towards the formation of antibands considers the down-step adatom electromigration and is derived for the case of the attachment-detachment limited regime (or step kinetics limited regime) [99]. In this regime surface sublimation is controlled by the atomic processes at elementary steps because the rate of adatom attachment-detachment is much slower than the rate of adatom surface diffusion. This results in a pile-up of adatoms at the step edges and creates the gradient of their concentration across large terraces separating step bunches. This non-uniformity of the adatom concentration eventually breaks the stability of the S-shape of crossing steps and initiates the process of antiband formation. However, initially this gradient in adatom concentration can be balanced by the variation of chemical potential μ_s along the crossing steps which is given by $\mu_s = -\bar{\beta} b^2 C_s$, where $\bar{\beta}$ is the step stiffness, *b* - atomic spacing and C_s is the step curvature [98]. Therefore, the appropriate variation of the step curvature C_s can compensate for the non-uniformity of the adatom concentration across the terrace and stabilize the steady state S-shape of the crossing steps. This compensation mechanism fails as the terrace width grows, initiating the onset of the antiband instability, which occurs when the terrace width (L_t) satisfies the necessary condition [98]:

$$\frac{FL_t^2}{\bar{\beta} b^2} > 2 \qquad (4.1)$$

where F given by $F = q_{ef} E$, is the electromigration force acting on adatoms, E is the electric field applied across the sample and q_{ef} is the effective electric charge of surface adatoms. The remarkable aspect of the condition (4.1) is that it does not account for the degree of surface vicinality in any form. It implies that for a given force *F*, the terrace width L_t required for the onset of the antiband instability is the same for any initial interstep distance (*l*) which is determined by the overall surface offcut from the low index plane.

The results of recent experimental investigations strongly suggest that sublimation on the Si(111) surface is a diffusion limited process [109, 111, 112], which is characterized by relatively slow surface adatom diffusion and fast kinetics at the atomic steps. Here we provide for the first time a theoretical treatment of the antiband instability under the condition of diffusion limited sublimation. We also experimentally study the onset of this instability and compare experimental and theoretical findings.

4.2 Theory of Step Shape Instability and Antiband Formation

Depending on temperature, the step bunching process on Si(111) can be maintained by either up-step or down-step driven dc current (*e.g*. in the temperature regimes 1050-1240 or 1250-1350 °C respectively) [34, 113]. Recent experimental studies have affirmed that in both annealing regimes antibands are located close to lower step bunches, while in the case of the attachment limited sublimation they are expected to grow closer to the upper step bunch when the heating current is driven in the up-step direction [28]. This was explained by a possible change in sign the of surface adatoms' effective charge from positive at higher temperatures to negative at lower [25, 96]. However, the assumption of a sign change is in contradiction with the results of earlier experimental studies, which clearly demonstrated that adatom electromigration on Si(111) proceeds in the direction of the applied electric field over a wide range of temperatures [114].

In this section we derive an expression for the adatom concentration gradient under the conditions of slow surface adatom diffusion and show that this gradient is independent of the direction of the electric current. As a consequence, the location of antibands under these conditions is no longer expected to change upon reversal of the electric current direction, which is in agreement with the experimental observations [28, 41]. The expression for the gradient is later used to derive the condition for the onset of the antiband instability.

4.2.1 Nonuniformity of the Adatom Concentration

The adatom concentration gradient on wide terraces between step bunches is induced by two rather different mechanisms in the two aforementioned regimes. In the step kinetics limited regime the concentration gradient is induced directly by the electromigration force *F* which pushes adatoms towards the atomic step at the terrace's edge where the adatoms create a "pile" due to the slow rate of the attachment process [98]. In contrast, the adatom concentration at the step on the opposite side of the terrace is lowered, because atoms detached from the step are immediately removed by means of electromigration.

In the diffusion limited regime, the concentration gradient is created by a different mechanism which is related to the repulsion interaction between atomic steps. On the macroscopic level this mechanism is based on the dependence of the local chemical potential on the curvature of the crystal surface. The positive surface curvature on one side of a wide terrace and negative on the other create conditions for the existence of the concentration gradient. The gradient created in this way can be neglected in the case of the attachment limited sublimation since its contribution is not significant compared to the direct contribution of electromigration force [98]. However, in the diffusion limited regime, the intensive atom exchange between the crystal phase and the adlayer of adatoms results in nearly equilibrium adatom concentration in the vicinity of the *j*-th step, which is given by [102]:

$$n_s^e\left(x_j\right) = n_s^e\left[1 + \tilde{A}\left(\frac{1}{l_{j-1}^3} - \frac{1}{l_j^3}\right)\right] \tag{4.2}$$

where $\tilde{A} = \frac{2\Omega g}{kT}$, n_s^e is the equilibrium adatom concentration on an ideal vicinal surface where $l_{j-1} = l_j$, g is the strength of the entropic and stress-mediated repulsion between atomic steps, Ω is the area of a single atomic site and $l_j = x_{j+1} - x_j$ is the width of the *j*-th terrace between atomic steps with the coordinates x_j and x_{j+1}. When the j-th terrace is the large terrace between two bunches (*i.e.* $l_j = L_t$), the condition $L_t >> l_{j-1} \sim l_{j+1}$ can be

applied and the expressions for $n_s^e(x_j)$ and $n_s^e(x_{j+1})$ can be simplified by neglecting the term $\frac{1}{L_t^3}$ giving:

$$n_s^e\left(x_j\right)=n_s^e\left[1+\tilde{A}\left(\frac{1}{l_{j-1}^3}\right)\right]$$

and

$$n_s^e\left(x_{j+1}\right)=n_s^e\left[1-\tilde{A}\left(\frac{1}{l_{j+1}^3}\right)\right] \tag{4.3}$$

Making use of the equation (4.3) one obtains the expression for the adatom concentration gradient G_r on a wide terrace:

$$G_r=\frac{\mathrm{n_s^e}(x_j)-n_s^e(x_{j-1})}{L_t}=\frac{1}{L_t}n_s^e\tilde{A}\left[\frac{1}{l_{j-1}^3}+\frac{1}{l_{j+1}^3}\right] \tag{4.4}$$

where l_{j-1} is the width of the highest terrace in the lower bunch (outflow region where atomic steps detach from the bunch) and l_{j+1} is the width of the lowest terrace of the higher bunch (inflow region).

Expressions for l_{j+1} and l_{j-1} were derived in earlier theoretical studies (Eq. (22) in Ref. [115]) for a conserved system where surface desorption could be neglected [115]. It should be noted that l_{j+1} and l_{j-1} behave differently in the case of non-negligible desorption, as was revealed by numerical integration of step motion equations within the framework of the one dimensional model [26]. These numerical calculations of l_{j+1} reproduce the result obtained for a conserved system [115] but give considerably larger values of l_{j-1}. As an approximation we will use the expression derived for a conserved system[20] but written with somewhat different notation:

$$l_{j-1}=l_{j+1}=\left(\frac{2\Omega g}{|F|d_s}\right)^{1/3}N^{-1/3} \tag{4.5}$$

where $d_s=\frac{D_s}{K}$ is the kinetic characteristic length, D_s is the coefficient of surface diffusion, *K* is the step kinetic coefficient, *g* is the step repulsion coefficient and *N* is the number of

steps in the bunch, which in the following considerations is assumed to be the same for all bunches. Substituting equation (4.5) into equation (4.4) gives an expression for the adatom concentration gradient:

$$G_r = -2n_s^e \frac{N}{L_t}\left(\frac{|F|d_s}{kT}\right) \tag{4.6}$$

Equation (4.6) suggests that, in the regime characterized by the slow surface diffusion, the gradient of the adatom concentration across wide terraces indirectly arises through the presence of large adjoining step bunches on the terraces' sides. The applied electric field results in the formation and subsequent growth of the step bunches, which provide conditions for the creation of the concentration gradient. The essential aspect of equation (4.6) is that the adatom gradient depends on the absolute value of the electromigration force and is independent of its direction.

4.2.2 Shape of the Crossing Steps-limits of Stability.

For simplicity the shapes of crossing steps are analyzed for the down-step electromigration under equilibrium conditions. Under equilibrium conditions the surface desorption is either negligible or compensated by the appropriate deposition [28] and the crossing steps remain in their fixed positions. In the following we will consider the coordinate system with the *x*-axis along the step bunches, the *y*-axis normal to them with the positive direction from the lower to the higher terraces and the origin in the middle of the terrace (figure 4.1(a)). Using the same approach as formulated by Thurmer [98], the adatom concentration gradient (G_r) compensation by the variation of the step curvature C_s can be expressed in these coordinates as

$$\frac{\bar{\beta} n_s^e \Omega}{kT} C_s = G_r y \tag{4.7}$$

The crossing steps' equilibrium shape *y*(*x*) can be found by solving differential equation (4.7), which is equivalent to

$$\frac{y''}{\left(1+y'^2\right)^{3/2}} = ay \tag{4.8}$$

with $a = \dfrac{G_r kT}{\bar{\beta} n_s^e \Omega}$, and can be easily reduced to

$$y' = \pm \frac{1}{ay^2 - C}\sqrt{4 - \left(ay^2 - C\right)^2} \tag{4.9}$$

where *C* is an arbitrary constant that can be found by applying the boundary condition $y'\left(\dfrac{L_t}{2}\right) = 0$:

$$C = 2 + a\left(\frac{L_t}{2}\right)^2 \tag{4.10}$$

Equations (4.9) and (4.10) provide a background for clear understanding of the different stages of the crossing steps' evolution and transitions between these stages. Initially, the crossing steps are curved in the long S-shape and the sign of their slope $y' = \dfrac{dy}{dx}$ remains the same over the *y*-interval given by $0 \le y \le \dfrac{L_t}{2}$ (figure 4.1(a)). This situation is realized when L_t satisfies the inequality:

$$L_t < 2\sqrt{\frac{2}{|a|}} \tag{4.11}$$

leading to the equation for the critical value of terrace width L_{tcr}:

$$L_{tcr} = 2\sqrt{\frac{2\bar{\beta} n_s^e \Omega}{|G_r| kT}} \tag{4.12}$$

Once L_t exceeds L_{tcr}, the crossing steps make the transition from the long S-shape (figure 4.1(a)) to the S-shape (figure 4.1(b) and (c)). The S-shape is characterized by a change in sign of the slope in each half of the terrace and can only be maintained in the limited interval of L_t values. The lower boundary of this interval is determined by L_{tcr}, while the upper limit $L_{t\max}$ can be determined from the condition $y'(0) = 0$:

$$L_{t\max} = 4\sqrt{\frac{\bar{\beta} n_s^e \Omega}{|G_r| kT}} \tag{4.13}$$

For $L_t > L_{tmax}$ the step's slope becomes zero in the middle of the terrace and the equilibrium S-shape can no longer exist. At this point, the variation of step curvature cannot compensate for the gradient of the adatom concentration so that the steps lose their stability and gradually lose their symmetry marking the onset of the antiband instability (figure 4.1(d) and (f)).

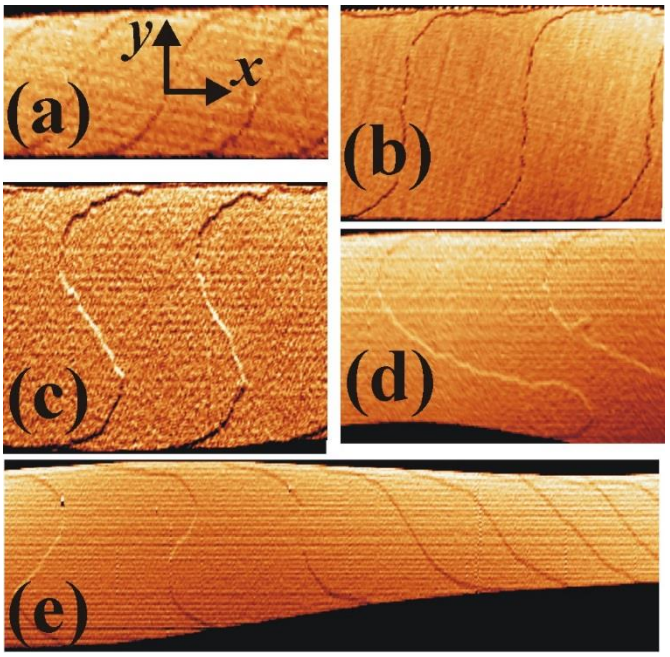

Figure 4.1: Evolution of crossing steps' shape towards the formation of antibands on Si(111) terraces.

(a) Crossing steps are curved in the long S-shape. The sign of the step's slope remains the same along the entire step. (b) Crossing steps are aligned perpendicular to the step bunches. A further increase in the terrace width allows the transition to the S-shape. (c) Crossing steps in the steady-state S-shape, characterized by change in sign of the slope in each half of the terrace. (d) Crossing steps gradually develop a segment with a zero slope indicating the onset of the antiband instability. (e) Crossing steps "frozen" at different stages of their evolution on a single widening terrace.

These results are valid for the equilibrium shape of crossing steps but cannot be applied directly to high temperature regimes where sublimation rates can be significant (*e.g.* 1250<T<1350 °C). As a result, the steps do not retain their positions on terraces but move along at measurable rate. In this case one should consider the steady-state of crossing steps which needs some comments. Generally, the shape evolution of a moving step is described by the equations [116]:

$$\frac{\partial x}{\partial t} = -V\sin\varphi + \frac{dV}{d\varphi}\cos\varphi, \quad \frac{\partial y}{\partial t} = V\cos\varphi + \frac{dV}{d\varphi}\sin\varphi \tag{4.14}$$

where $x(\varphi,t)$ and $y(\varphi,t)$ are coordinates of a point on the step, φ is the angle between the normal to the step at this point and the *x*-axis, *t* is the sublimation time and *V* is the step velocity given by

$$V = K\Omega\left(n_s - n_s^e\right). \tag{4.15}$$

The $V(\varphi)$ dependence is quite complex because the step kinetic coefficient *K* is generally anisotropic. This anisotropy is created by kinks produced along the step by geometrical misalignment of the step orientation and the crystallographic directions for atomically straight steps. When the density of these kinks exceeds the density of thermally activated kinks the coefficient K becomes a function of φ. Also, *V* depends on φ via the adatom undersaturation (or oversaturation) $\Delta n_s = n_s - n_s^e$ because the adatom concentration n_s in the equation (4.15) has a gradient along the *y*-axis, while the equilibrium concentration n_s^e depends on the step curvature, which varies along the step or, in other words, it depends on $x(\varphi,t)$ and $y(\varphi,t)$.

Such complex $V(\varphi)$ dependence makes calculating the time evolution of crossing steps a challenging task. However, here we are interested in the relatively simple case of the steady-state shape, where the step motion is limited to simple translation along the *x*-axis and equation (4.14) can be reduced to:

$$\frac{\partial x}{\partial t} = -V_{tr}, \quad \frac{\partial y}{\partial t} = 0 \tag{4.16}$$

where V_{tr} is the velocity of the step's translational motion as a whole. Finally, combining equations (4.15) and (4.16) results in the equation for the steady state shape of the crossing step:

$$y'' = ay\left(1+y'^2\right)^{3/2} + \frac{V_{tr}}{\Omega K}a'\left(1+y'^2\right) + \Delta n_s a'\left(1+y'^2\right)^{3/2} \tag{4.17}$$

where

$$a' = \frac{kT}{\bar{\beta}\, n_s^e \Omega} \tag{4.18}$$

Equation (4.17), which takes into account the undersaturation Δn_s and the translational velocity V_{tr}, can be reduced to the equation (4.8), derived for the equilibrium conditions, by assuming that Δn_s and V_{tr} are negligible. However, in the general case, the undersaturation and its influence on the step velocity will result in a deviation of crossing steps from their equilibrium shape and affect the final form of equations (4.12) and (4.13) for L_{tcr} and $L_{t\max}$.

4.2.3 Onset of Antiband Formation

Equation (4.6) for the gradient in the adatom concentration can be modified by taking into account that the number of steps in the bunch is given by $N = \frac{L_t + L_{bunch}}{l}$ and substituting this expression into equation (4.6), which results in:

$$G_r = -2n_s^e \frac{1}{l}\left(1+\frac{L_{bunch}}{L_t}\right)\left(\frac{|F|d_s}{kT}\right) \tag{4.19}$$

where L_{bunch} is the width of the step bunch and *l* is the mean initial terrace width. As was discussed earlier, the formation of antibands begins when crossing steps develop segments aligned parallel to the step bunches after the terrace width L_t exceeds L_{tmax} given by equation

(4.13). Substituting equation (4.19) into the equation (4.13) results in the criterion for the onset of the antiband instability under conditions of slow surface adatom diffusion:

$$L_t^2\left(1+\frac{L_{bunch}}{L_t}\right)\frac{d_s|F|}{\bar{\beta}\, l\Omega}\geq 8 \tag{4.20}$$

The condition $L_{bunch} << L_t$ can be applied in the case of a low vicinal surface and the inequality equation (4.20) can be simplified to:

$$L_t^2\frac{d_s|F|}{\bar{\beta}\, l\Omega}\geq 8 \tag{4.21}$$

which is similar to equation (4.1). The relationships in equations (4.20) and (4.21) contain the ratio $\frac{d_s}{l}$, which is determined by the surface miscut from the low index crystallographic plane. This is in striking contrast with the equation (4.1) which was derived for the case of attachment limited sublimation [98] and does not include the degree of surface vicinality in any form.

It is important to point out that equation (4.20) was obtained by solving equation (4.8), which describes the equilibrium shape of crossing steps. It captures the essential thermodynamic aspect of the problem, while the process of antiband formation can be substantially more complex when investigated experimentally. As was discussed earlier, a more accurate result can be obtained by solving equation (4.17), which describes the steady-state shape of crossing steps and accounts for the kinetic processes and under saturation at the steps. However, the solution of equation (4.17) is currently unknown to us.

4.3 Experimental study of the effects of surface vicinality on the formation of antibands

The condition in equation (4.20) formulated in the form of inequality suggests that L_t and L_{bunch} must reach certain minimum width for any fixed values of l and F in order to achieve

the onset of antibands. *F* can be controlled in experiments by varying the electric field applied across the sample, while *l* can be chosen by slicing a low index surface at an appropriate angle α. In the next section we experimentally examine equation (4.20) by studying the relationship between the onset of the antiband instability, the electromigration field, initial distance between the atomic steps and the width of step bunches and terraces.

Experimental Results and Discussion

The surface morphology created on Si(111) by extended annealing was characterised by step bunches separated by several μm wide terraces. It was important to analyse only terrace segments which featured crossing steps at the same stage of their evolution. Therefore, the annealing times were adjusted for all samples so as to create a large selection of terraces comprising crossing steps in the same symmetric steady-state S-shape such as in figure 4.1(c). Significant variation in the size of these terraces was observed with some being up to 80% wider than the detected minimum. Qualitatively, this is in agreement with the inequality in equation (4.20), which gives a necessary but insufficient condition for the onset of the antiband instability. Thus for fixed values of *F* and *l*, the lower limit of this relationship is defined by the widths of the terrace and the corresponding step bunch, which provide the lowest value of the product $L_t^2\left(1+\frac{L_{bunch}}{L_t}\right)$ denoted as L_m from now on. Expectedly, the terraces of the least width were found to be adjoined to the proportionally narrowest step bunches, throughout the entire experiment.

Figure 4.2 shows the dependence of the ratio (l/L_m) on the electromigration field *E* for the terrace segments containing crossing steps in the symmetric steady-state shape. For each experimental point in the figure, 20-25 sites of 50 × 50 μm^2 were randomly selected across the entire step bunched area and the L_m value was drawn from 30-40 separate terraces containing crossing steps in the steady-state S-shape. The critical field is known to be weaker for Si(111) with lower vicinality, therefore samples with lower angles of misorientation provided a wider range of electric fields over which the antiband instability could be studied.

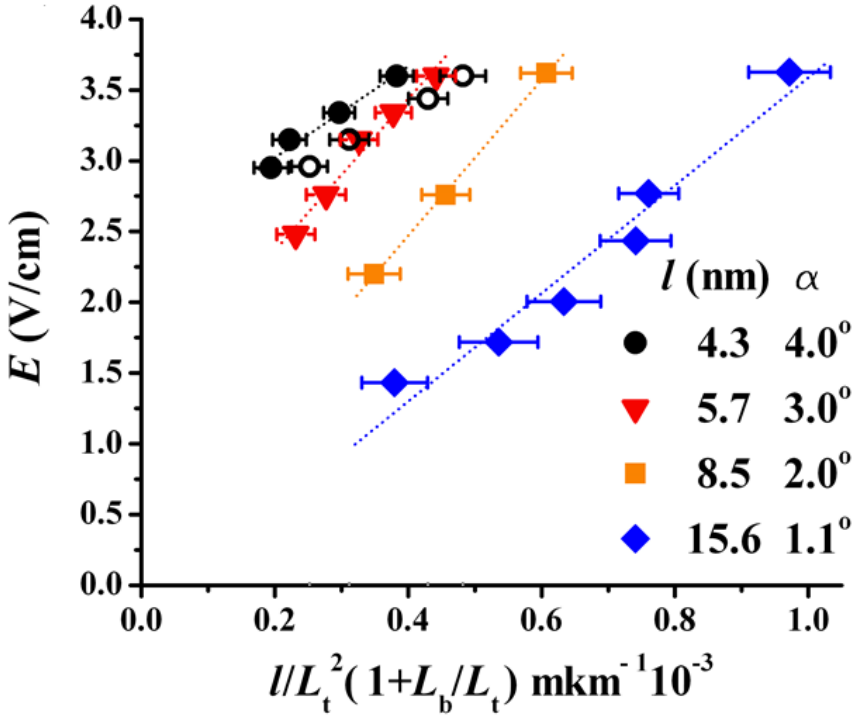

Figure 4.2: Applied electric field E plotted as a function of the highest value of the product $\frac{l}{L_t^2\left(1+L_{bunch}/L_t\right)}$ for Si(111) with different mean initial terrace width l. L_t and L_{bunch} denote the width of the terrace and the adjoining step bunch respectively. The plot is expected to produce a straight line according to equation (4.20). Only terraces containing crossing steps in the symmetric S-shape were taken into account. α indicates the angle of misorientation from the Si(111) surface towards the [11-2] direction. The graphs plotted for Si(111) with α=1.1° & 4° were added to measurements of α=2° & 3°, produced from previous studies.

The open circles in figure 4.2 represent the $E(l/L_m)$ dependence for the narrowest terrace segments featuring crossing steps aligned perpendicular to the step bunches as in figure 4.1(b). These terraces can be deemed to have reached their critical size L_{tcr} given by equation (4.12) as a further increase in the terrace width allows the transition to the S-shape where the crossing steps are separated into two distinct lobes (figure 4.1(c)). This graph was plotted for Si(111) with a 4° misorientation and shows merely an offset in the position of L_m when compared to the graph obtained for terraces with the crossing steps in the steady shape.

Thus, for the same initial inter-step separation, the exponent in the $E(L_m)$ relationship is unaffected by the choice of the step's stage of evolution.

Figure 4.2 shows that the minimum terrace and bunch width required for the onset of the antiband instability progressively increases as the electric field is reduced. The $E(l/L_m)$ graphs are linear and clearly demonstrate that the terrace and bunch widths strongly depend on the initial distance between atomic steps l in agreement with equation (4.20). Due to the nature of the experiment, the pairs of step bunches and terraces which provide the absolute minimum of the product L_m could not be detected on every annealed surface, which can explain the observed difference in the slope between the graphs but cannot account for their significant offset along the E-axis. However, this offset is not significant for Si(111) with α=1.1° (l=15.6 nm), therefore the $E(l/L_m)$ dependence can be directly compared with the equation (4.20), and the value of the effective charge can be estimated. Using the extrapolated value for $\bar{\beta}$ =28 meV/Å [37, 98, 117], the lower limit of the characteristic length d_s=0.3 nm and $\Omega \approx 10^{-1}$ nm^2 results in an excessive value of the effective charge q_{ef}=1.95|e|. However d_s=1.7-4.5 nm gives q_{ef} = (0.35-0.13)|e| as reported in earlier studies [25, 97, 98]. This indicates that there is a possibility for highly vicinal surfaces, with small l, to enter into crossover between attachment-limited and diffusion-limited regimes where the characteristic length d_s is comparable to l. It should be mentioned here that is the d_s value as compared to l that determines the regime of sublimation [118] and that equation (4.1) and equation (4.20) describe two limiting cases, given by conditions $d_s > l$ and $d_s < l$, respectively. For completeness, the $E(L_t)$ dependence for α=1.1° was compared with equation (4.1) for the attachment-limited regime, and the value q_{ef} = 0.013|e|was found.

A possible explanation for the graph's offset along the E-axis is that the $E(l/L_m)$ dependence does account for the relative proximity of the electromigration field E to the critical point, where the surface is stable to the step bunching. Equation (20) was also derived with the implicit assumption that E_{cr} equals zero, which is in disagreement with the results of the latest experimental investigations. These investigations demonstrate that, in the most studied third temperature regime, the critical field for Si(111) is significant and grows linearly with the increasing surface misorientation angle [109]. For example, for Si(111) with

misorientation of 3° (l = 5.7 nm) or 4° (l = 4.3 nm), E = 2.0 V/cm is less than E_{cr} and the value of L_m obtained with these parameters from the equation (4.20) would not be physically meaningful.

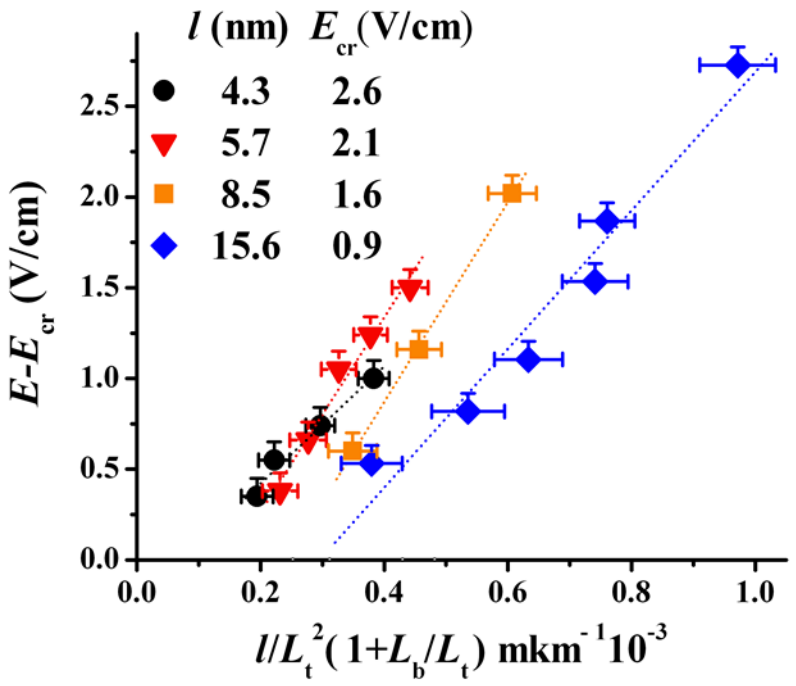

Figure 4.3: The electric field in Fig 4.2 is replaced by $E - E_{cr}$, where E_{cr} is critical field, *i.e*. the lowest field required to initiate the step bunching process.

For $E < E_{cr}$ step bunching cannot be initiated and wide terraces required for antiband formation cannot be created. This, however, is not reflected in equation (4.6) which predicts the presence of the gradient at any applied electric field. The reason for this disagreement can be found in equation (4.5) which is used in the derivation of equation (4.6). The equation (4.5) is valid only for a conserved system with negligible desorption, which assumes that the adatom's mean diffusion path λ_s tends to infinity [119]. As a result, the critical field tends to zero in accordance with the equation for E_{cr}:

$$|E_{cr}| = \frac{12\Omega g}{d_s \lambda_s^2 q_{eff} l} \tag{4.22}$$

obtained under the conditions of slow adatom diffusion [109]. Therefore, when using equation (4.5) we implicitly assume that $E_{cr} = 0$ and pass this assumption onto equation (4.20). This is a necessary measure since an analytical expression for the width of the highest and lowest terraces in the bunch (equation (4.5)) is currently unavailable for the practical case of intensive sublimation.

In order to approximately account for the factor of critical field, E in equation (4.20) can be replaced by the difference E-E_{cr} and L_m can be plotted versus E-E_{cr} as shown in figure 4.3. In this case, the graphs' offset along the E-axis is significantly reduced and experimental data collected on Si(111) with different misorientation partly overlap, as would be expected from equation (4.20). This indicates the importance of accounting for the critical field when modeling step bunching or antiband instabilities. This problem was not identified in earlier theoretical studies where E_{cr} was implicitly assumed to be equal zero [118]. Extrapolating the $E_{cr}(l)$ experimental dependence [109] shows that in the practical case of heavy desorption this is a reasonable assumption for surfaces with a small angle of misorientation of less than 0.5°.

4.4 Conclusions

We provided a theoretical treatment of the antiband instability under the condition of the adatom surface diffusion limited sublimation. Under this condition, we derived an expression for the adatom concentration gradient across the wide terraces where the antiband growth takes place. We showed that this gradient arises through the presence of step bunches separating terraces and depends on the absolute value of the electromigration force. Importantly, it is independent of the force direction in strong agreement with the experiments on Si(111), where the antibands were found to be created in the same locations on terraces regardless of whether the electric field was applied in the up-step or the down-step direction.

We analyzed the limits of stability of crossing steps' shape under equilibrium conditions and used the expression for the concentration gradient to derive the condition for the onset of the antiband instability. Remarkably, this condition implies that the terrace width required

to achieve the formation of antibands strongly depends on the degree of surface vicinality, *i*.*e*. for a given strength of the applied electric field, wider terraces and step bunches are needed in order to create the antibands on the surfaces with wider initial inter-atomic-step distances (or lower angles of surface misorientation from the low index plane).

The condition was experimentally examined by studying an early stage of the antiband formation on the Si(111) surface with the different misorientation angles from the Si(111) plane. The experiments were conducted at constant temperature of 1270 °C, whilst systematically varying the applied electric field. This allowed us to investigate the relationships among the onset of the antiband instability, the electromigration field, initial distance between the atomic steps, and the width of step bunches and terraces. The experiment strongly supports the validity of the theoretically derived condition for the onset of the antiband instability. It also indicates the importance of accounting for the factor of critical field in the theoretical models of step bunching or antiband instabilities.

Chapter 5

Electromigration Induced Step Bunching on Vicinal α-Al_2O_3 Surfaces

Кітап, ғылым - тілсіз мұғалім.

In this chapter we report on the first observation of step bunching induced by electromigration on vicinal c-plane $Al_2O_3(0001)$ surfaces. This step bunching instability occurs for in-plane electric fields applied perpendicular to the miscut direction. Annealing with electromigration fields of $E \approx$ 30-140 V/cm in the step-up direction at 1500 ˚C causes the atomic steps to transform into step bunches. Annealing with same electric field in the step-down direction leads to the formation of a regular step array, however prolonging the annealing time in the same direction does eventually produce weakened step bunching. Atomic steps crossing the terraces were observed to develop towards the formation of antibands. De-bunching of the step-bunches was obtained by annealing the step-bunches in a reversed *E*-field. The bunching behaviour on $Al_2O_3(0001)$ displays a critical electric field (E_{cr}). Below E_{cr}, a faceted surface was created. A scaling relationship between the maximum slope of a step bunch, $y_{m,}$, and step bunch height, *h,* was identified that fitted the form of a power law function ($y_m \sim h^{\alpha}$), with scaling exponent $\alpha \approx$ 0.78 for samples annealed by the step-up electric field of $E \approx$ 140 mV/cm for 6 and 20 hours. The impact of the electromigration force on the slope of step bunches was analyzed by annealing steps with

different applied *E*-fields at the same temperature. A scaling relationship, $y_m \sim E^q$, between y_m and electromigration field was experimentally derived, with $q \approx 0.054$, extracted from step bunching morphologies created by annealing for a variety applied electromigration fields.

5.1 Introduction

Alumina and in particular α-alumina or sapphire, due to its insulating properties and chemical stability, is widely used as a substrate in a large number of technological applications [120, 121]. Since terrace step edges are energetically favourable for the adatom nucleation, the sapphire steps were reported to act as an effective substrate for nanocluster growth, such as the self-assembled nucleation of nanowires and nanodots along the steps [122-124]. Faceted α- Al_2O_3 templates also have been used for the deposition of highly ordered self-assembled noble metal nanoparticle arrays [125, 126]. More recently, sapphire (0001) surfaces have been utilized as a substrate for the growth of graphene. This graphene grown on sapphire is an interesting candidate for the design of field effect transistor arrays [127-129]. In addition, the review by Joselevich reported the self-organized growth of single-walled carbon nanotubes on the steps of α- Al_2O_3 (0001) [130].

Remarkable changes occur in the structure of the vicinal sapphire surface after air annealing at 1500 ˚C, resulting in the agglomeration of atomic steps and the formation of step facets and step bunches [60, 131, 132]. The occurrence of step bunching indicates the presence of a long distance step-to-step attractive interaction [133].

This chapter reports the observation of step bunching induced by electromigration on the (0001) surface of the binary insulator α-Al_2O_3. We present step-bunching morphologies obtained for sapphire surfaces with different applied electric fields at a fixed annealing temperature. It was found that the bunched steps can also de-bunch by annealing with a reversed *E*-field. The value of the critical *E*-field, i.e., the minimum electric field required to initiate step bunching, was determined. It was also established that the step bunch maximum slope y_m depends on its height *h* and the dependence between them fits to the

power-law function of the form $y_m=y_0h^{\alpha}$. The scaling exponents from this form are extracted and compared with the reported values of the scaling exponents of Si(111) [29].

5.2 Results

5.2.1 *E*-field Annealing

The faceting of sapphire surfaces has been widely observed and investigated [60-66]. Vicinal sapphire also is known to form step bunches upon annealing in either ultra-high vacuum (UHV) or ambient conditions [131, 132]. However this is the first systematic study of the influence of electromigration on stepped structures on Al_2O_3(0001) surfaces.

Figure 5.1 shows AFM images for sapphire samples with a miscut of 3° annealed at 1500 °C for 6 hours in the presence of an *E*-field of 140V/cm in the step-down (a) and step-up directions (b). The sapphire annealed with a step-down *E*-field exhibits faceted morphology, with regular steps of height 10-20 nm aligned along the $[10\bar{1}0]$ direction on the (0001) surface. These steps are separated by 0.1-0.4 μm wide terraces and in places join each other at an angle of ~150°, which corresponds to the angle between the $[1\bar{1}00]$ and miscut $[1\bar{2}10]$ directions. The step edges are primarily aligned along $[1\bar{1}00]$ direction, however in the vicinity of merging steps they align to the low index $[1\bar{2}10]$ direction.

Annealing for 6 hours with $E \approx 140$ V/cm in the step-up direction creates notably different step bunched morphology and demonstrates many characteristics similar to those observed on step bunched Si(111) [109]. Figure 5.1(b) shows that an Al_2O_3(0001) surface with 30-110 nm high step bunches separated by 0.4-1.3 μm wide terraces. Figure 5.1(b) also demonstrates a high density of crossing steps on the terraces and majority of them are curved in the long S-shape. It is interesting that each terrace between crossing steps contains one triangular nucleation island with the size 200-500 nm positioned in the middle of the terrace. The two sides of each island are aligned along the step edges of the crossing step and the step bunch respectively.

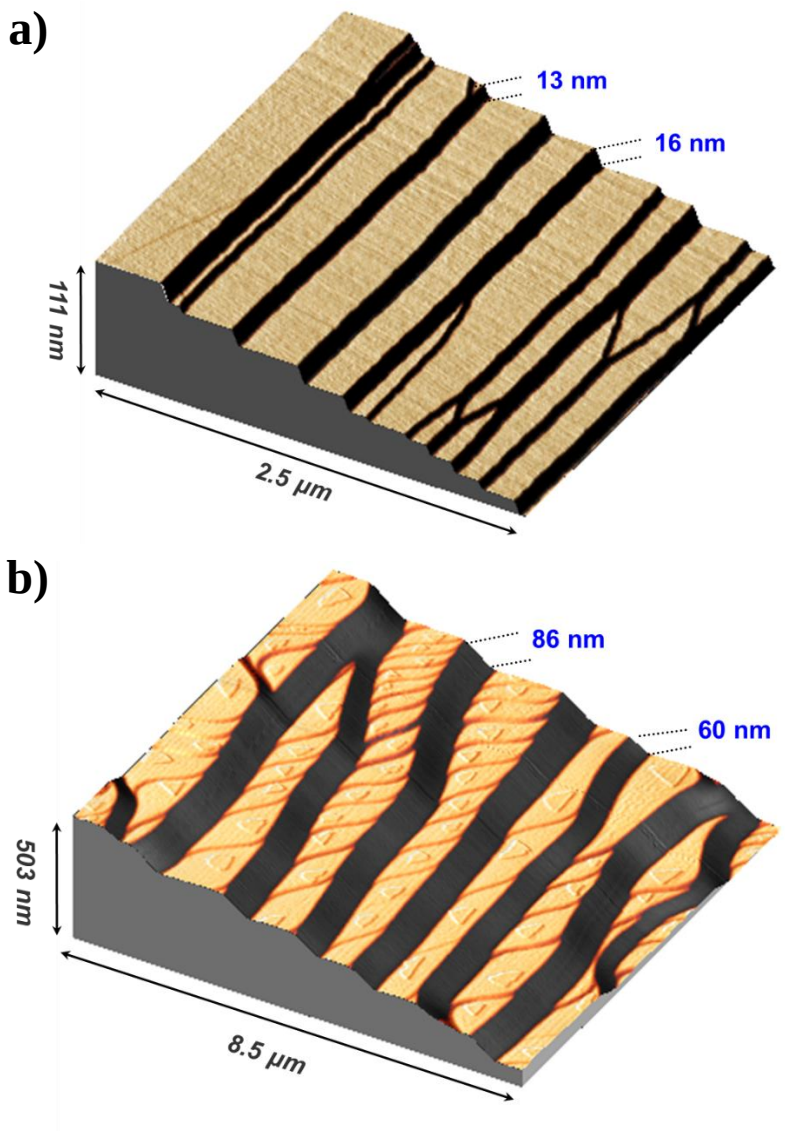

Figure 5.1: Surface morphologies created on 3˚ miscut sapphire sample by annealing with *E*-fields of ~ 140V/cm at 1500 ˚C. (a) Annealed with a step-down *E*-field, there are terrace widths up to ~ 0.4 µm separated by regular 10-17 nm steps with a few step junctions joining at an angle of ~ 150° (b) Annealed with a step-up *E*-field, the step bunches up to ~ 100 nm in height and terrace widths up to ~ 1.3 µm.

The minimum limit of the influence of the electromigration field on the step bunching formation is determined by the critical field E_{cr}, as applying an electric field weaker than E_{cr} results in the cessation of the step bunching process. To examine how the strength of the electric field influences the morphology, samples with same 2˚ miscut angle, were annealed under the same conditions for a variety of E-fields in the range from the attainable maximum to critical. Figure 5.2 shows AFM images of how the morphology of vicinal

Al_2O_3(0001) changes as a function of field strength, for an *E*-field applied in the step-up direction. The surface of the sample annealed with the *E*-field of 100 V/cm is characterized by 0.5-1.2 µm wide terraces and high step bunches up to 100 nm (figure 5.2(a)). Annealing with a weaker applied electric field $E \approx 70$ V/cm reduces the electromigation of adatoms and thus results in the formation of relatively low step bunches, with the maximum bunch height being ~90 nm and an average terrace width of ~ 0.7 µm (figure 5.2(b)). Annealing with a field of 40 V/cm (figure 5.2(c)) produces a step bunched surface with an average bunch height of approximately 20 nm, while the terraces are reduced to the relatively narrow width of 0.2-1 µm. For comparison figure 5.2(d) shows the faceted surface created by annealing without an electric field, the average height is approximately 10 nm. The dimensions of the step bunches formed with the aid of an E-field are notably greater compared with faceted surface produced by annealing without the presence of an electric field. Figure 5.2 also shows that there is a relative loss of step straightness for increasing electric field strength during annealing. It is believed that the Al_2O_3 surface decomposes into O and AlO gas phases upon thermal annealing in vacuum [134], which may be susceptible to a biased adatom drift under the influence of an electric field.

Annealing in the step-down *E*-field direction (figure 5.1(a)) creates a faceted surface with average step height of 10-20 nm which cannot be distinguished from the morphology created by thermal annealing (See figure 5.2(d)). Similar surface structures have been observed on alumina (0001) annealed in vacuum and in air [132]. Similarities between the morphology of the sapphire surfaces produced by annealing with step-down *E*-field and thermally annealed samples, shown in figures 5.1(a) and 5.2(d), respectively, suggest that the electric field annealing in the step-down direction does not significantly affect the surface rearrangement.

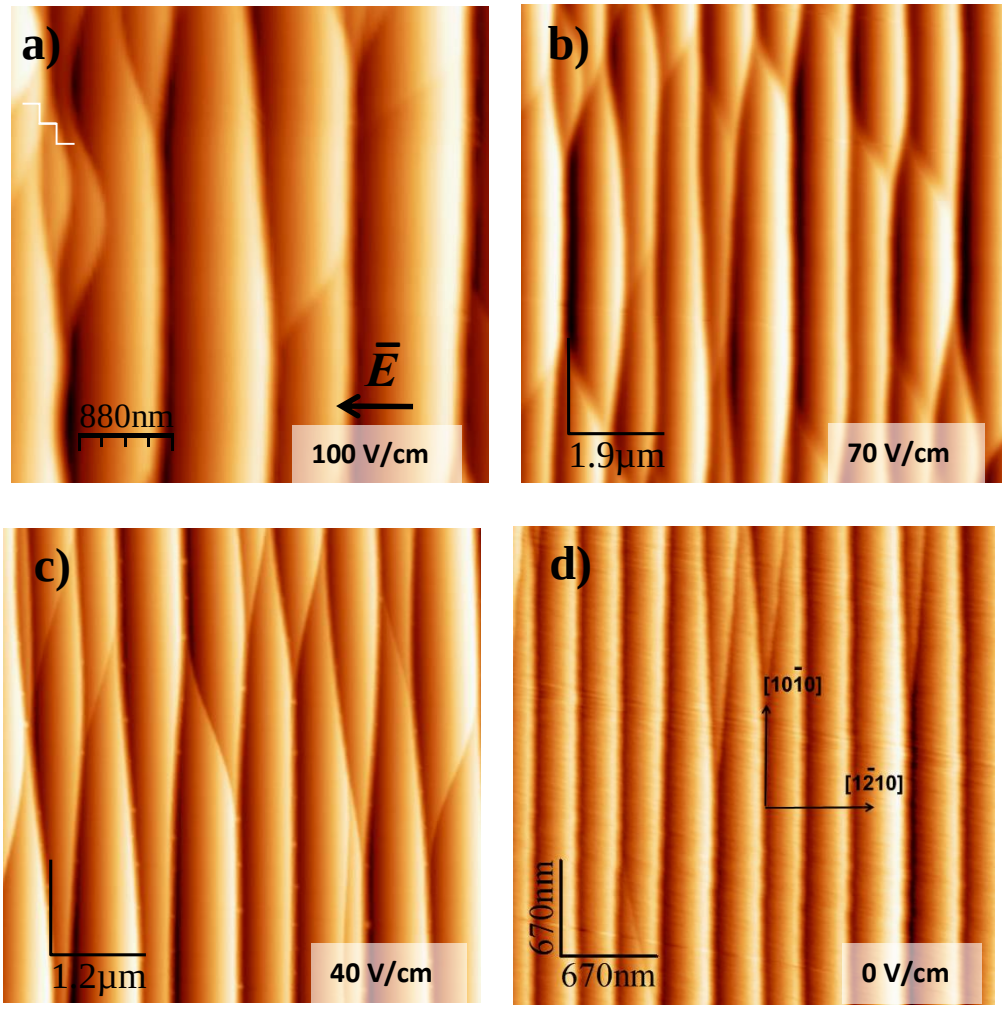

Figure 5.2: The morphology of α- Al_2O_3 surface after annealing for 6 hours at 1500 ˚C for different electromigration forces in the step-up direction. The surface is off cut by 2˚ towards the [1 $\bar{2}$ 10] direction. The miscut direction is from left to right in all images as presented by a staircase symbol in (a). An arrow in (a) shows the electric field direction related to all images. (a) Step bunched Al_2O_3(0001) surface after annealing with $E \approx 100$ V/cm. (b) A reduced electric field of 70 V/cm creates, on average, step bunches 20-50 nm in height. (c) A lower step bunch height of ~ 20 nm is produced on the sapphire surface after annealing with electric field of 40 V/cm. (d) Faceted morphology with a highly regular step array was observed with relatively narrow terrace widths after thermal annealing with no electric field.

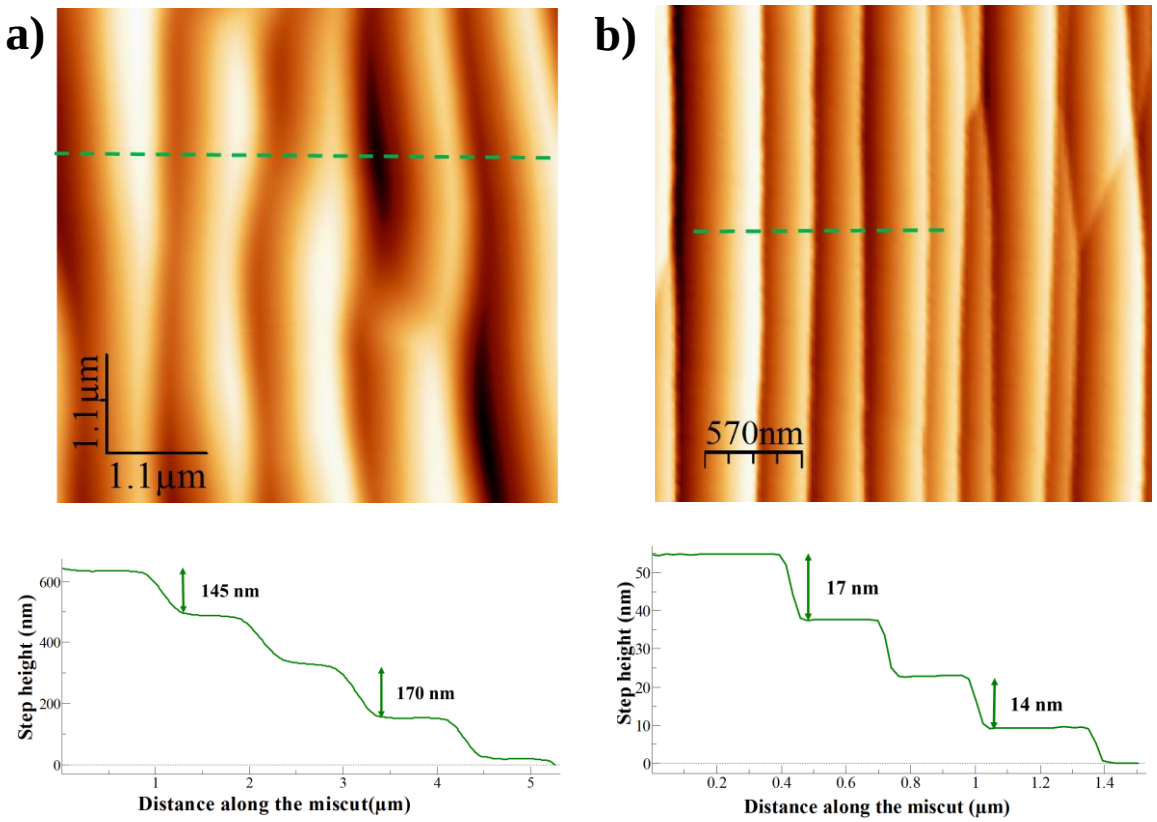

Figure 5.3: Step bunching morphologies on Al_2O_3(0001) surfaces obtained by extended annealing time of 20 hours with $E \approx 140$ V/cm. This surface is off cut by 3° towards the $[1\bar{2}10]$ direction. (a) Bunched sapphire surface after annealing with the electromigration field applied along the step-up direction. (b) Straight step bunches produced on the vicinal surface after step-down *E*-field annealing. Below the AFM images are plane levelled line profile of these surfaces with values of bunch heights.

The effect of extending the annealing time was also studied by annealing samples for a period of 20 hours, these were then analysed *ex-situ* by AFM. Annealing the 3˚ miscut sample with $E \approx 140$ V/cm in the step-up direction creates step bunched surface, where height of step bunches is increased to 90-220 nm and terrace width to 0.8-2.5 µm. The increase in step bunch height is accompanied by a further loss of step straightness (figure 5.3(a)), as was generally observed with increasing electric field. When the same *E*-field of 140V/cm was applied in the step-down direction for the same sample miscut angle, this resulted in a surface that was less bunched, with relatively narrow 0.1- 0.5 µm terraces separated by 12-25 nm high step bunches (figure 5.3(b)). It can be concluded that prolonged annealing with an electric field in the step-up direction results in the formation

of higher step bunches, while annealing in the step-down direction leads to formation of much smaller bunches on the c-plane α- Al_2O_3 surface.

5.2.2 De-bunching Behavior

To see whether the growth process of the step bunches could be reversed (de-bunching), the same electric field of 100 V/cm was applied with the direction reversed (step-down) to a bunched sample which previously had been annealed using step-up *E*-field (figure 5.2(a)). After annealing with the *E*-field in the opposite direction the distance between the single steps in the bunch was increased, leading to a broadening of the step bunches. A comparison between representative bunched steps and those subjected to a de-bunching process are shown in figure 4. Before de-bunching 85 nm step bunch had a typical width of 430 nm. After annealing the reversed field, a step bunch with a similar height is seen to have a width of 990 nm (figure 5.4(b)). This result shows that single steps can be exchanged between neighboring bunches and step bunches are unstable towards de-bunching process. We assume that upon annealing with a reversed *E*-field the step bunches on sapphire tend to de-bunch due to of the lower effective stiffness of a bunch of steps compared to a single step or a smaller cluster in a bunch and that the steps can escape from the bunch as they move with the different velocities under the most probable direct force which mainly acting upon aluminium and oxygen ions.

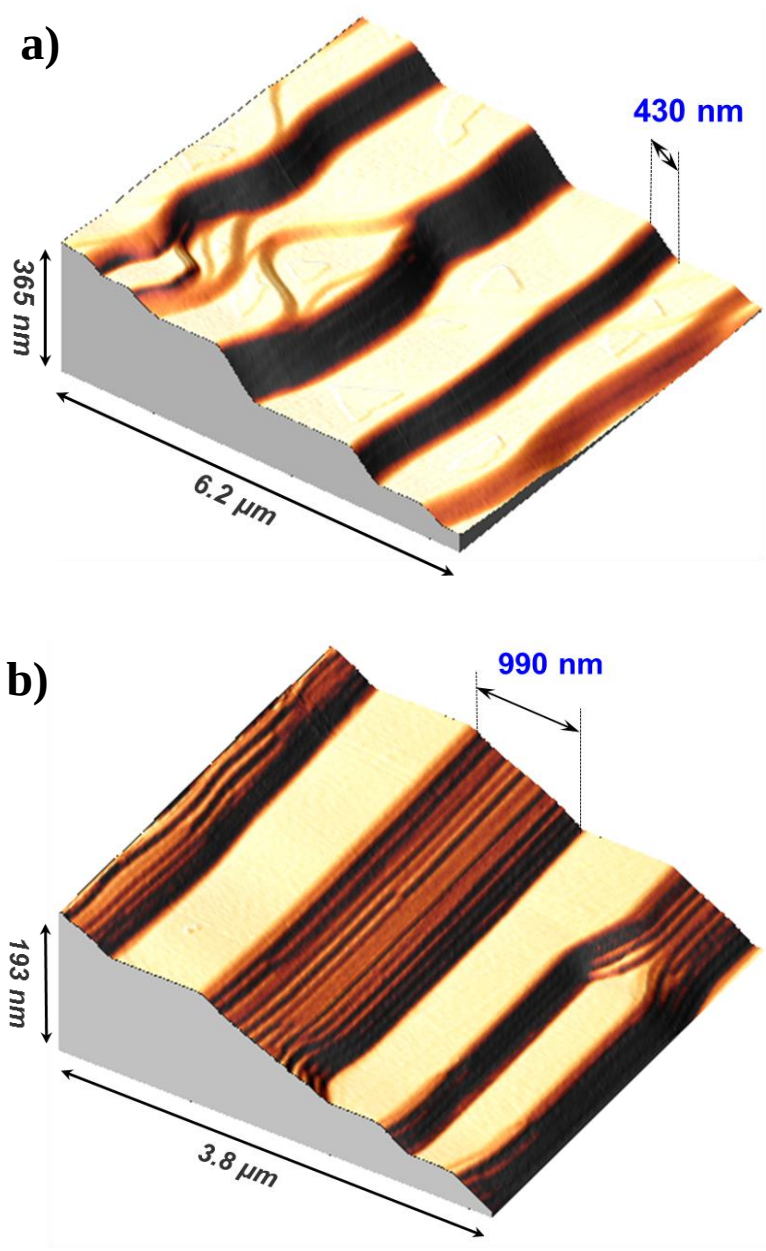

Figure 5.4: Reversal of step bunching on α-Al_2O_3(0001) surface offcut by 2° towards the [$1\bar{2}$10] direction. (a) Step bunched sapphire surface obtained by *E*-field annealing, E ≈ 100V/cm at 1500° C along the step-up direction. (b) Morphology of the same bunched sample after annealing with the *E*-field in the opposite direction. The two step bunches with values of their widths shown have heights of ~ 85 nm in both AFM images.

5.2.3 Crossing Steps and Antibands

The step bunched surfaces produced by annealing in the step-up direction also exhibit multiatomic steps which cross the terraces. In particular, a comparison was made between the shapes of crossing steps for the step-up *E*-field of 140V/cm for the samples annealed for 6 hours and 20 hours, as shown in figures 5.5(a) and (b), respectively. The crossing steps on the terrace are curved in a long S-shape after 6 hours annealing (figure 5.5(a)). These clusters of crossing steps form a regular pattern on the terraces and run over 5-10 μm along the $[10\bar{1}0]$ direction with a periodicity of 0.1-0.2 μm, this behaviour is demonstrated in figure 5.5(a). After extending the annealing time to 20 hours the crossing steps form bunches with slopes oriented opposite to the primary bunches, as seen in figure 5.5 (b). These antibands are known to form on Si(111) via the shape evolution of the atomic-steps crossing the wider terraces [30]. Figure 5.5 (b) also shows antibands on a terrace aligned along the $[10\bar{1}0]$ direction. Different stages of the evolution of crossing steps, with similar shapes to those seen on bunched Si(111), can be seen on the surface as a whole.

Based on the similarity of the studies of crossing steps' morphology on Si(111) under the condition of diffusion-limited sublimation [30, 109], we can deduce that the attachment-detachment of the adatoms is much slower than the rate of adatom surface diffusion for the Al_2O_3(0001) surface too. This results in a pile-up of adatoms at the step edges and produces the gradient of their concentration across large terraces separating step bunches. This non-uniformity of the adatom concentration is responsible for the cluster of crossing steps in a long S-shape located close to each other. This configuration of crossing steps is the initial stage of their evolution towards antiband formation. The variation of step curvature at different development stages can compensate for the non-uniformity of the adatom concentration across the terrace. Prolonged *E*-field annealing allows the crossing steps to further develop and whole terraces become covered by high density crossing steps. As the terrace width grows with prolonged annealing time, the compensation mechanism fails, initiating the antiband formation process.

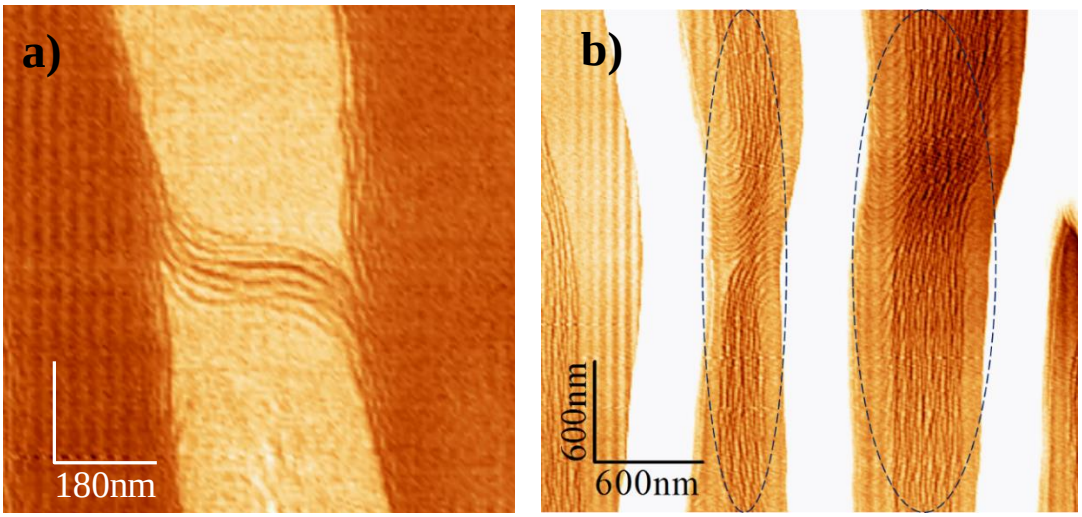

Figure 5.5: Evolution of terrace crossing steps' shape towards the antiband formation on 3˚ miscut sapphire. (a) Crossing steps are curved in the long S-shape on a terrace of the bunched (0001) surface after annealing with $E \approx 140$V/cm for 6 hours. (b) Annealing for 20 hours with the same E-field gives the bunch antibands. A group of high density antibands on a terrace are highlighted.

5.2.4 Quantitative Analysis of Step Bunching Instability

To verify that the steps are not a result of faceting, the relationship between the step bunch height and the maximum slope was examined. A strong correlation between the bunch height and its maximum slope was observed. The maximum slope increased with step bunch height, which is evident from the plane levelled cross-sectional profile and its derivative shown in figure 5.6(a) and (b) respectively.

The influence of the electromigration force on the slope of step bunches is illustrated in figure 5.7 which shows slope profiles along the miscut direction of 84-86-nm-high step bunches produced by annealing with a variety of applied electric field strengths. These slope profiles were taken from the samples with 2˚ miscut towards the $[1\bar{2}10]$ direction, annealed with the E-field in the step-up direction. The step bunch slope is seen to reduce with decreasing electric field, approaching the slope of structures created by thermal annealing. Annealing with $E < 30$ V/cm produces a surface with faceted steps similar to the surface morphology created by thermal annealing. This can be taken as the minimum limit of the electric field required to initiate the step bunching, also known as the critical field E_{cr}, Annealing with $E < E_{cr}$ had no effect on the step dynamics for surfaces with $\vartheta = 2°$.

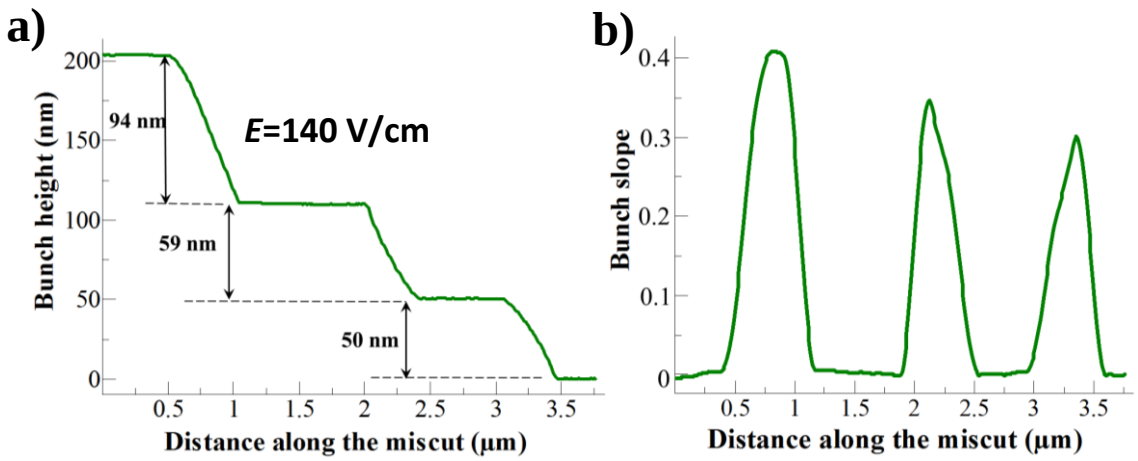

Figure 5.6: The relationship between the step bunch height and its slope. This surface is off cut 3˚ and annealed for 6 hours with $E \approx 140$ V/cm in the step-up direction. (a) Plane levelled line profile along the miscut. (b) Corresponding derivative showing the slope of the line profile.

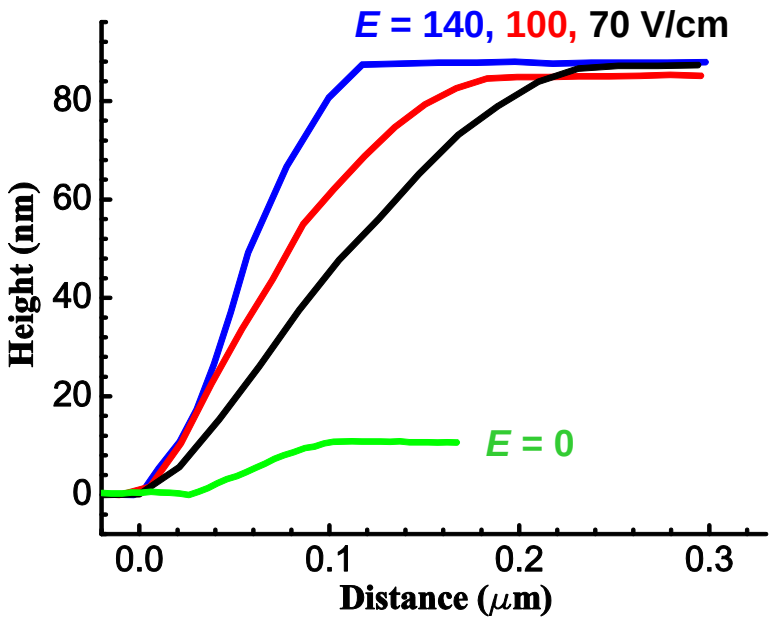

Figure 5.7: Slope profiles of 84-86-nm-high step bunches formed by annealing with different applied *E*-fields along the step-up direction on samples off-cut by 2˚. The step bunches produced by annealing with stronger electromigration fields have steeper slopes.

In order to get a quantitative understanding of how the electric field strength influences the density of steps within the bunches, the maximum slope y_m was plotted against electromigration field E for two different sample step-bunch heights (figure 5.8). The step bunches with values of h=30 nm and 40 nm were selected from bunched areas of 2˚ miscut samples that is free of high-density crossing steps or antibands. The height (h) of step bunches observed on each sample by AFM was measured with an error of ~ 1 nm from the plane levelled topography. The corresponding maximum slope, $y_{m,}$ was extracted by taking the maxima of the derivative of the plane levelled step profiles, i.e. step profiles corrected so that flat (0001) terraces have zero slope and height is taken as the difference between adjacent terraces. The data were fitted to a power-law function $y_m = y_1 E^q$ and the values of q were found to be ~ 0.054 and 0.055. These values of q are notably lower compared to the experimentally extracted scaling exponent $q \approx 0.33$ for bunched Si(111) after step- up electric field annealing [29].

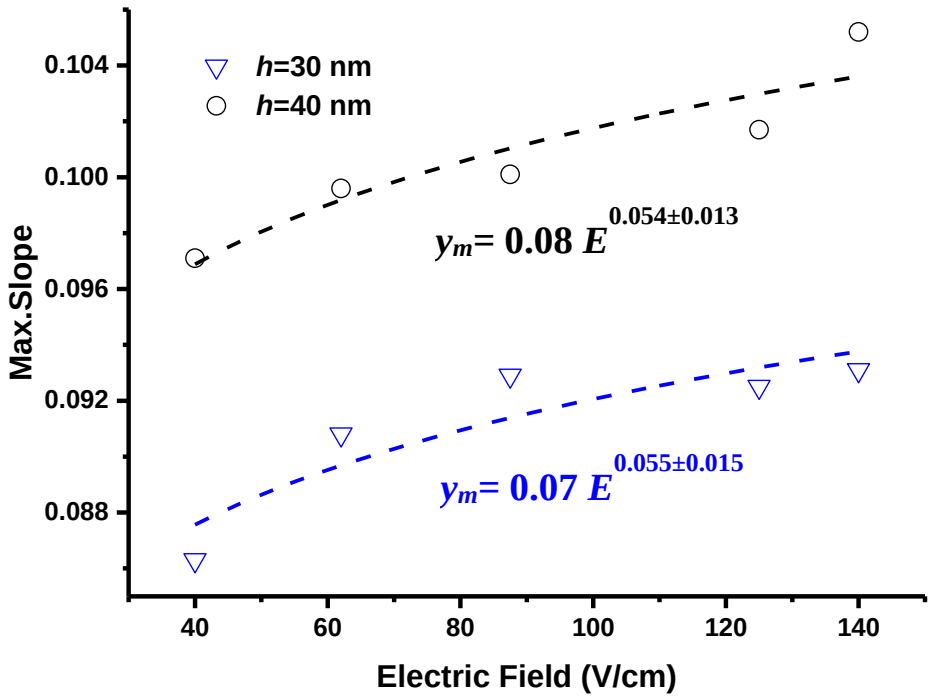

Figure 5.8: Maximum slope y_m as a function of electric field E for 30- and 40-nm-high step bunches produced on a sapphire surface with off-cut by 2˚. Fitting the data with a power-law function $y_m = y_1 E^q$ results in the values of $q \approx 0.054$ and 0.055.

The sample with 3˚ miscut in figure 5.1(b) was analysed *ex-situ* by AFM. Figure 5.9 shows that in different annealing times, the dependences between maximum slopes and their heights fitted with a power law function of the form, $y_m = y_0 h^{\alpha}$, where α was found to be ~ 0.78 after annealing for 6 and 20 hours, with fitting error of ±0.04. The values of α for the same miscut sample are the same which means an extended *E*-field annealing increases the step bunch height by keeping the same scaling relationship between the step bunch height h and the maximum slope y_m. This value of "α" is notably larger than the experimentally determined scaling factor of "$\alpha \approx 0.6 \pm 0.04$" for Si(111), step-bunched with a step-up electric field [25, 29]. The observed values of α for bunched Al_2O_3(0001) surfaces are not similar to the reported values of scaling exponents of Si(111).

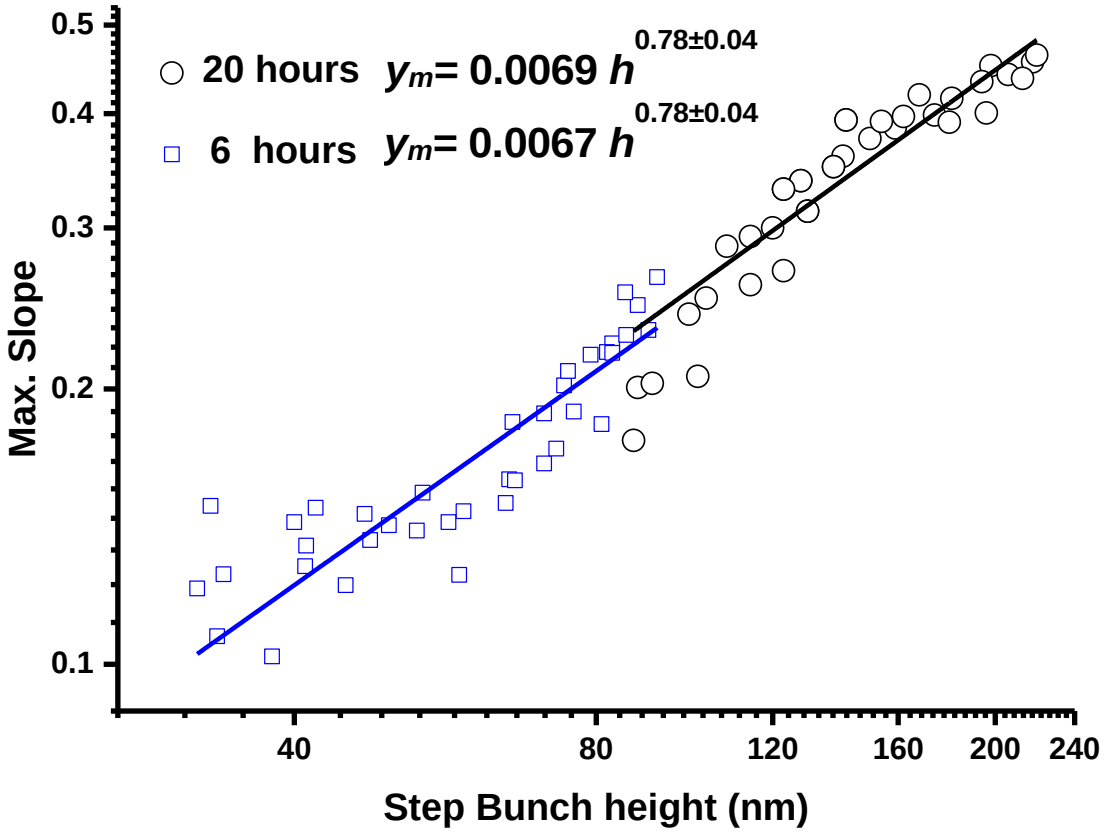

Figure 5.9: Plot of maximum slope of the bunch y_m, against its height h for vicinal α- Al_2O_3 with a miscut of 3˚ annealed at $E \approx 140$ V/cm for 6 and 20 hours in the step-up direction. These scaling relationships show that y_m, increases with step height.

As can be seen from figure 5.9 the maximum slope increases with height over the whole range of data. For faceting one would expect a levelling out of the maximum slope for larger steps, however this is not the apparent case.

Despite the differences in temperature, electric field and scaling exponents, step bunching on Al_2O_3(0001) share many similar features with electromigration induced step bunching on seen on Si(111). It is sensitive to the strength and direction of the *E*-field, the atomic steps can be bunched and de-bunched, crossing steps and antibands form on the surfaces, at values below the critical electric field step bunching is not observed, and there are scaling relationships between the slopes of step bunches and their heights. From these similarities it can be deduced that the step bunching process on sapphire surfaces, much like silicon, is due to adatom diffusion resulting from a direct electrostatic force.

5.3 Conclusions

For the first time, electromigration induced step bunching has been observed on the surface of an insulator, aluminium oxide. A range of electric fields $E \approx$ 30-140 V/cm were applied to vicinal sapphire samples perpendicular to the miscut direction, for a variety of annealing times. We observed that an electric field driven along the step-up direction for 6 hours at 1500˚ C forced the migration of adatoms on Al_2O_3(0001), resulting in the formation of step bunches separated by wide terraces. These step bunches were found to grow with time, as could be seen by a comparison of the morphologies of steps bunches on surfaces annealed for 6 and 20 hours by step-up *E*-field of $\sim$ 140 V/cm. In contrast, an *E*-field at $\sim$140 V/cm directed along the step-down direction for 6 hours leads to formation of the faceted surface by stabilizing the regular step distribution. However, weakened step bunching was observed after prolonged annealing with the same *E*-field for 20 hours in the step-down direction. Crossing steps on the terraces of the bunched sapphire evolve towards the formation antibands by prolonging the annealing time, much like for Si(111).

The value of the critical electric field E_{cr}, was measured ($E_{cr} \approx$ 30 V/cm) for a miscut angle of 3º. Applying electric field below this critical value results in cessation of the step bunching process and produces a faceted surface, similar to the surface morphology after

thermal annealing. Weaker electromigration fields close to E_{cr} create straighter step bunches with lower step bunch heights and, as a result, steps become more stable towards the step bunching instability. It was also found that the step bunches are unstable towards the de-bunching process under the oppositely applied *E*-field. These step bunches de-bunch under a reversed *E*-field annealing as a result of the exchange of single step distance attributed to the enhanced step-step repulsive interaction.

The scaling relationship between the maximum slope of a step bunch height y_m, and step bunch height, was experimentally probed. The same scaling exponent was found to be $\alpha \approx 0.78$ for the vicinal sapphire samples with a miscut of 3° annealed at 1500˚ C with electric field $E \approx 140$ V/cm applied in the step-up direction for 6 and 20 hours. The difference in the final state of the step bunched morphologies is expressed in terms of scaling relation, $y_m \sim E^q$, between y_m and electromigration field *E,* for a constant height. Scaling exponents $\alpha \approx 0.054$ and 0.055 were extracted from different step bunch heights. This work may be interesting for future applications, as we have demonstrated control of the step bunch height and slope of stepped sapphire, by controlling the main parameters, such as applied *E*-field strength and annealing duration, at fixed temperature. Further theoretical studies are needed to explain the mechanism of the step bunching instability on insulating sapphire surfaces induced by the electromigration.

Chapter 6

Step Bunching Induced by Electromigration on W(110)

Ақыл азбайды, білім тозбайды.

This chapter reports on the electromigration-induced step bunching on vicinal W(110) surfaces, for a variety of miscut angles, that occurs when electric fields are applied perpendicular to the step direction. An electric field of 30 mV/cm, applied in both step-down and step-up directions, was found to be sufficient to induce electromigration of the tungsten atoms and produce step bunching on vicinal W(110) at 1500 ˚C. A scaling relationship between the maximum slope of a step bunch, $y_{m,}$ and its height, $h,$ was identified that fitted the form of a power law function ($y_m \sim h^{\alpha}$), with scaling exponents $\alpha \approx 0.6$ and 0.69 for the vicinal W(110) samples annealed under the step-up and step-down electric fields of $E \approx 30$ mV/cm and 60 mV/cm, respectively. These obtained values are similar to the scaling exponents found for the step bunched Si(111) surface. However our results suggest that step bunching mechanism is fundamentally different for the vicinal silicon and tungsten surfaces. Step bunching morphology created on tungsten surfaces annealed with an electric field is analysed and discussed, providing insight into the step bunching process. Experimental results show that higher electric fields result in larger step bunches on vicinal W(110) surfaces.

6.1 Introduction

Tungsten, with its advantageous physical and electrical properties and numerous technological applications, has held a particular importance in this research area [135-139]. More recently, vicinal tungsten surfaces have been used as templates for directly ordered growth of thin films and nanowire arrays [140-142]. For instance, the near step flow growth regime exhibited by Fe on the vicinal surface of W(110) has led to significant progress in the area of magnetic nanowires [143]. In addition, surface spin spirals in Fe double layers on the W(110) surface has been the focus of multiple experimental and theoretical studies [144-149].

Vicinal W(110) surfaces have been used as templates for the deposition and oxidation of submonolayer Au, also concluding that chemisorption of oxygen causes nano-faceting of the vicinal W(110) surfaces [150]. Another atomic level study, by *Basset*, investigating the effect of heating on a field-evaporated tungsten surface, showed surface rearrangements such as the formation of surface steps several atomic layers high and local roughening at temperatures above 850 K, due to the random movement of adatoms [151].

This chapter discusses the first observation of the phenomenon of electromigration-induced step bunching on a metallic W(110) surface. It is suggested that the step bunching process occurs on tungsten surfaces due to adatom diffusion resulting from the so-called electron wind force [152]. We establish that the scaling relationship which exists between the step bunch height, h, and the maximum slope, $y_{m,}$ follows a power law relationship, as in previous Si(111) studies [29].

6.2 Experimental Results and Discussion

6.2.1 STM Results

To assess the quality of the surface and determine the impact of the cleaning and oxidising pre-treatment procedure, the samples were examined using a room temperature scanning tunnelling microscopy (STM) *in-situ* during cleaning and a comparison was made with the post annealed surface. Figure 6.1 shows examples of the STM topography of the vicinal

W(110) sample with a miscut of 0.8° after the cleaning and oxidising treatment process and after DC induced step bunching. The base pressure in the preparation and analysis chambers of the STM were 2×10^{-10} Torr and 3×10^{-11} Torr, respectively. Figures 6.1(a) and (b) demonstrate typical large area STM images of the vicinal W(110) sample after annealing in oxygen and flash heating at 2100 ˚C. The inset in figure 6.1(a) is 1×1 LEED pattern taken from the clean vicinal W(110) surface. The STM image in figure 6.1(a) shows that steps on this clean vicinal tungsten surface are not quite equidistant, while figure 6.1(b) reveals that most of the steps are monoatomic. The STM studies demonstrate that after oxidation of the vicinal tungsten samples, producing the protective oxide layer, most of the steps become multi-atomic. The typical heights of the formed multi-atomic steps were 1 to 2 nanometers and these values were very rarely exceeded. Figures 6.1(c) and (d) provide typical STM images taken after annealing in an oxygen atmosphere (1×10^{-6} Torr) for 80 minutes. The large area STM image in figure 6.1(c) shows a surface region containing several 2 nm high steps. The surface oxide layer forms a row-like reconstruction, highly regular at the atomic scale, with oxide rows parallel to the step direction, as LEED pattern inset in figure 6.1(c) and STM image in figure 6.1(d) illustrate. The oxide rows in figure 6.1(d) are parallel to the [001] crystallographic direction coinciding with the step direction on this vicinal tungsten surface. According to the LEED and STM data, the oxide row periodicity is 3.0±0.1 nm for the structures shown in figure 6.1(c) and (d). The exact atomic structure of the oxide layers used for the protection of different samples is beyond the scope of the current study. It should, however, be emphasized that the conventional annealing by external heat sources in an oxygen atmosphere never produced steps with heights above 3 nanometers, proving that the observed high bunches could only be a result of DC annealing-induced electromigration. As examples, figures 6.1(e) and (f) illustrate that the typical heights of the step bunches on the vicinal W(110) sample with a 0.8° miscut are in the range of 30-90 nanometers after annealing for 6 hours at 1500°C with directcurrent of 6 A in the step-up direction.

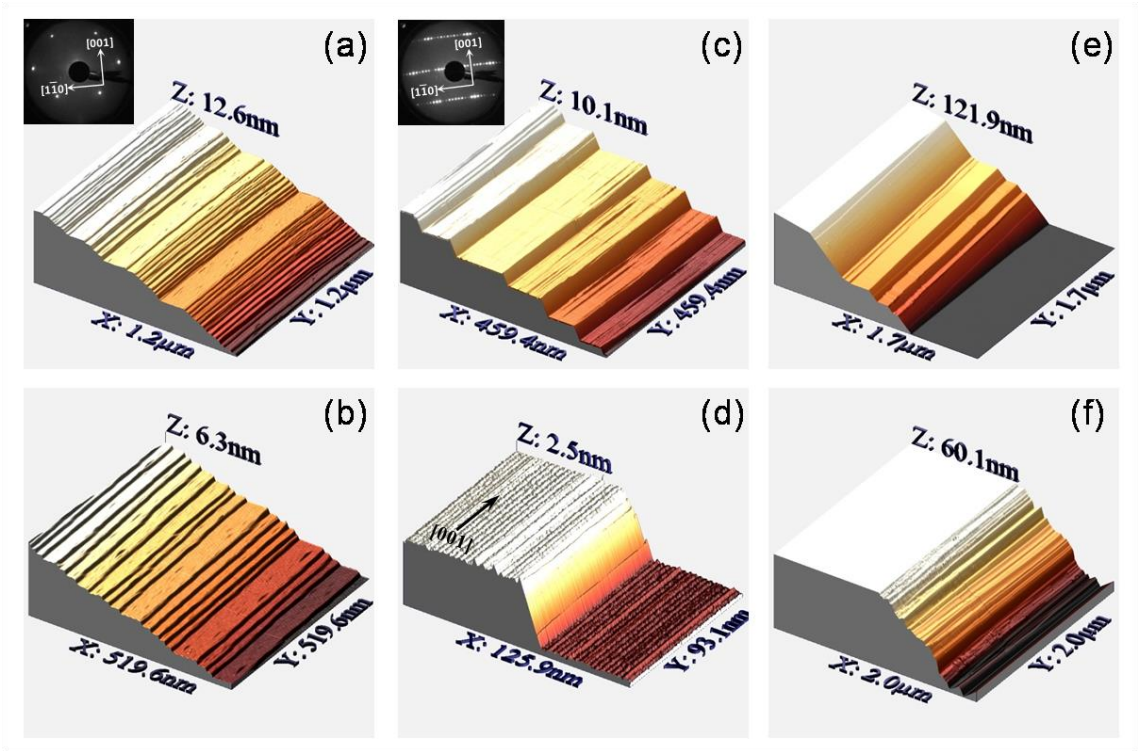

Figure 6.1. STM images of clean (a, b), oxidised (c, d) and bunched by electric field (e, f) vicinal W(110) surfaces with a miscut of 0.8° in the [1 $\bar{1}$ 0] direction. The images demonstrate preferentially single atomic steps on the clean surface (b), oxygen induced 2-nm-height bunches (c) and regular oxide rows parallel to the step direction (d) and multi-step 30-90 nm bunches formed after DC annealing at 1500°C (e, f). Insets in panels (a) and (c) show LEED patterns taken from clean and oxidized vicinal W(110) surfaces at electron beam energies of 62 and 55 eV, respectively.

6.2.2 *E*-field Annealing

To calculate the electromigration field that initiates the step bunching process on W(110) surface, the resistance of the sample at the annealing temperature of 1500˚C was estimated to be R = 4.2 x 10^{-3} Ω using the following equation:

$$R = R_0(1 + \alpha(T - T_0))$$

where R_0 is the resistance of the tungsten at room temperature [153], α is the temperature coefficient of W, and T_0 and T are the initial and final temperatures respectively. By using Ohm's law with a DC of 6A, an electric field of E ≈ 0.03 V/cm was determined. The applied

electric field of 0.03 V/cm is approximately 20 times smaller than the previously determined critical field for step bunching on Si(111) with a similar miscut [109]. However the step bunching occurring on tungsten at a lower electric field than on Si(111) could be attributed to a larger effective charge of the surface adatoms on W(110).

The bare vicinal W(110) surface has non-equidistant monoatomic steps, as is demonstrated by the STM images in figures 6.1(a) and (b). To see the rearrangement of the surface morphology after annealing at 1500 °C without electric field, one of the vicinal W(110) samples was thermal annealed in UHV for 6 hours. Tapping mode AFM characterization verifies that this UHV prepared surface is relatively flat, as shown in figure 6.2(a).

In contrast, AFM measurements of the vicinal W(110) sample with a miscut of 0.8° towards the [$1\,\bar{1}\,0$] direction annealed for 6 hours with step-up 6 A dc current revealed a step bunched surface. As shown in figure 6.2(b) 30-90 nm high step bunches are separated by 1-2.5 µm wide terraces. Figure 6.2(b) also shows a line profile from this AFM image, taken perpendicular to the bunched steps, indicating the bunch heights. This AFM characterization complements the STM images shown in figure 6.1(e) and (f) of the same sample. W(110) with a miscut angles 3.2˚ and 2.6 ˚ towards the [$1\,\bar{1}\,\bar{2}$] direction were annealed at 1500 ˚C for 6 hours with a 6A current. Figure 6.2(c) shows a sample miscut by 3.2˚ annealed with a step-down current. It can be noted, that the step bunches on this surface are smaller than for the previous surface with the 0.8˚ miscut in the [$1\,\bar{1}\,0$] direction. The narrow 50-200 nm terraces are separated by relatively small step bunches aligned along the [$1\,\bar{1}\,1$] direction with heights of 6-15 nm. Figure 6.2(d) shows a sample with a miscut of 2.6˚ towards the [$1\,\bar{1}\,\bar{2}$] direction, annealed at 1500 ˚C with a step-up DC of 6 A ($E \approx 30$ mV/cm). For this miscut (and conditions) there are 0.3-1.6 µm wide terraces separated by 30-70 nm step bunches.

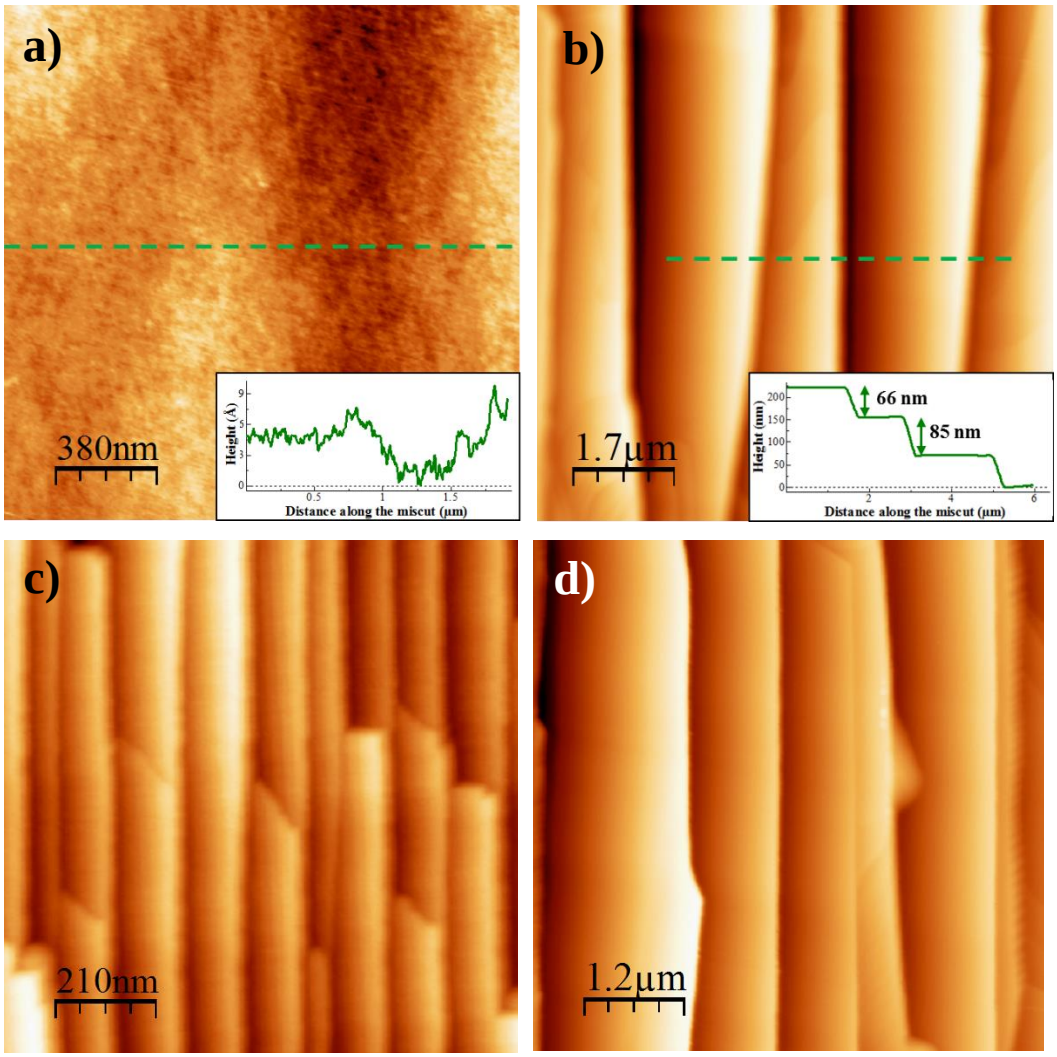

Figure 6.2: (a) Flat unbunched surface of W(110) with an off cut of 3.2˚ after thermal annealing in UHV at 1500 °C for 6 hours. (b) Bunched W(110) surface with a miscut of 0.8˚ annealed with a step-up direct current of 6 A toward the [1 $\bar{1}$ 0] direction. Inset, a plane leveled line profile showing the step heights. (c) Step bunching morphology, on the W(110) surface with an off cut of 3.2˚, obtained by annealing with a dc current of I = 6 A at 1500 ˚C along the step-down [1 $\bar{1}$ $\bar{2}$] direction ($E \approx 30$ mV/cm). (d) Bunched surface of W(110) with an off cut of 2.6˚ annealed with a step-up current, I = 6 A, towards the [$\bar{1}$ 12] direction.

For the same electromigration field of 30 mV/cm, the sample with the 3.2˚ miscut, annealed with a step-down current, produces smaller step bunches when compared with the surfaces with a miscut angles of 0.8˚ and 2.6˚ annealed with step-up. It was found step bunching could be amplified by applying a greater field in the step-down direction, which was achieved by driving greater current through the sample. It is unlikely that the increased

dc current could significantly affect the annealing temperature of the W samples as their resistance was low and therefore any heating contribution made by the resistive heating of the sample is overwhelmed by the ambient heating of the K-cell. Also, due to the metallic nature of the W samples, it can be argued that the electron wind must make a greater contribution to adatom electromigration as compared with Si samples, where the atomic steps bunch due to the direct force [152].

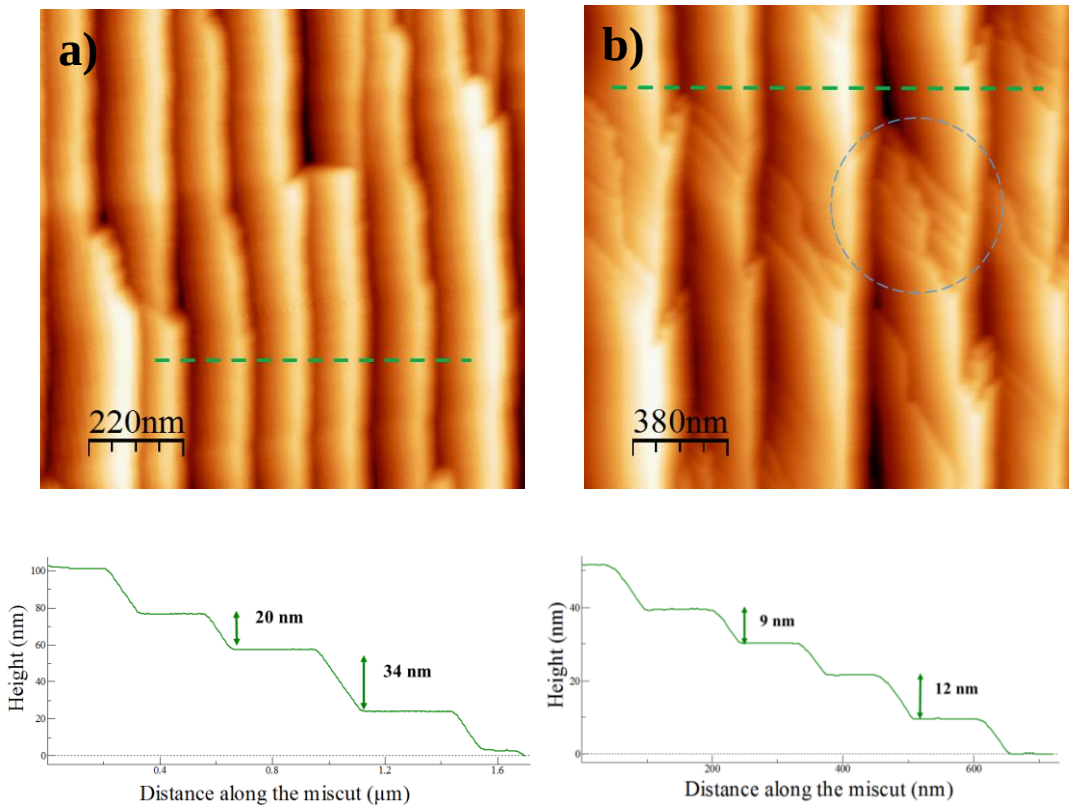

Figure 6.3: (a) Bunched W(110) sample with a miscut of 3.2˚ previously annealed with step-down direction (topography shown in figure 6.2c) subsequently annealed with step-up current, I = 6 A, towards the $[1\,\bar{1}\,\bar{2}]$ direction. The bunch height remains unchanged. (b) Surface morphologies created on the same bunched W sample by third annealing with a current of 10 A (E = 52 mV/cm) in the step-up direction. A group of high density crossing steps on a terrace are highlighted. Plane levelled line profiles for both AFM images are shown under the respective images.

To determine the stability of the step bunches a sample, which previously had been annealed by step-down 6A current (figure 6.2(c)), was annealed under the same conditions but with the electric field applied in the opposite direction (step-up), in an effort to

de-bunch the morphology. No appreciable change in the morphology of the bunched surface was observed as the bunch height and width remain the same as before, as demonstrated in figure 6.3(a). The same sample was then further annealed at a higher *E*-field of 52 mV/cm (*I* = 10A) in the same step-up direction for 6 hours. Figure 6.3(b) shows that this caused the dimensions of the step bunches to grow. The step bunches are 20-40 nm high and are separated by 0.2-0.5 μm wide terraces. It was noted however that after high DC annealing, the crossing steps' morphology had changed and loose bunches of crossing steps were observed on the terraces. The formation of these high density crossing steps may suggest an increased adatom concentration on the terraces. Further annealing with a current of 10A in the opposite, but initial, step-down direction for the same sample did not change the morphology.

To further illustrate the influence of reversal of the electric field on the integrity of the step bunches, figure 6.4 shows slope profiles, along the miscut direction, of a 9-nm-high step bunches produced by annealing with a DC of 6 A in the step-down and a step bunch of similar height from the same surface after annealing with the current in the opposite direction under the same conditions. The similarity of the slopes suggests the influence of reversal of the *E*-field on established step bunches is minimal as there is no apparent relaxation of the bunches with the distance between steps in the bunch being preserved. Thus it can be concluded that the step bunches are stable towards de-bunching as the reversed *E*-field does not influence the slopes of step bunches.

It appears that the tungsten steps are stable to the de-bunching process, which may be due to the greater effective stiffness of a bunch of steps compared to a single step in a bunch and that the individual steps within the bunch cannot readily escape from the pack as they move with the same velocity under the "electron wind" force which is the main lateral driver acting upon tungsten atoms.

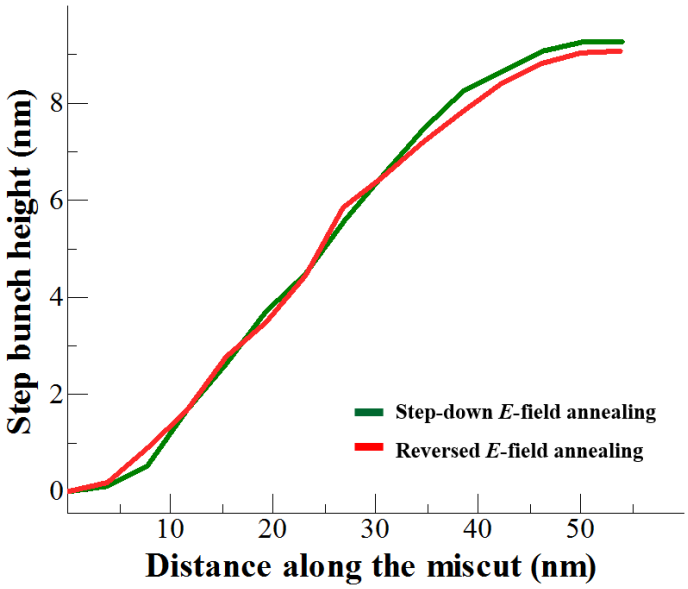

Figure 6.4: Slope profiles along the miscut direction, showing the lack of effect of annealing with a reversed *E*-field on representative 9-nm-high step bunches. The surface is off cut 3.2˚. The profiles were taken from the surface after annealing with a step-down DC of 6 A (figure 6.2(c)) and the same bunched surface then annealed by step-up 6 A current (figure 6.3(a)), respectively.

W(110) samples with a 2.6˚ miscuts towards the $[1\,\bar{1}\,\bar{2}]$ direction were also annealed with higher *E*-fields at 1500 °C for 6 hours. A vicinal W sample was annealed with step-down current of 12 A and an estimated $E \sim 60$ mV/cm. As seen in figure 6.5(a), this resulted in a step bunched surface with the average bunch height of approximately 70 nm and a maximum height of above 100 nm separated by 1.1-2.8 µm wide terraces. The effects of this increased electromigration force in the step-up direction were also examined for the same surface miscut. Figure 6.5(b) shows the resultant W(110) surface having step bunches with an average height of approximately 80 nm and a maximum bunch height up to 120 nm. The step bunches produced on this surface have a periodicity of 0.9-1.9 µm and the step-edges are notably rougher than for the down-step current. Comparing these results with the surfaces annealed with an $E \sim 30$ mV/cm for the same annealing time, there is an increase in the height of the step bunches obtained, for both the step-up and step-down current directions.

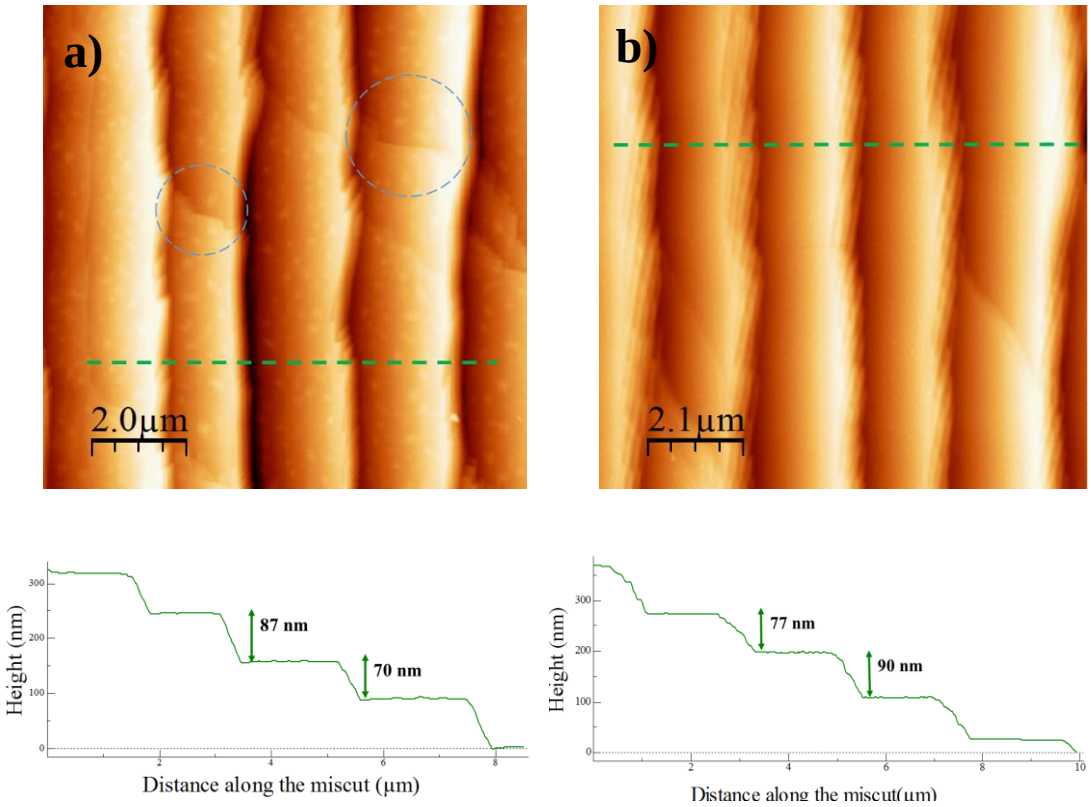

Figure 6.5: (a) Bunched W(110) surface with a miscut 2.6˚ annealed with step-down current of 12A towards the [1 $\bar{1}$ $\bar{2}$] direction. Below a plane levelled line profile of this surface is shown. (b) Step bunching morphology of the vicinal W(110) sample after annealing with step-up 12A dc current toward the [$\bar{1}$ 12] direction with a miscut of 2.6˚. The crossing steps are highlighted.

Both the step bunch morphologies obtained for the stepped surfaces annealed with step-up and step-down dc currents showed monoatomic crossing steps on the terraces. The majority of the crossing steps for all the bunched tungsten surfaces in this study, are curved in a long S-shape (as seen in a figure 6.5(a)), similar to the shape of crossing steps seen on the terraces of step bunched Si(111) [30].

These results demonstrate that step bunching in W(110) is sensitive to the direction of the current: step down vs step up. The larger step bunches observed for the higher applied annealing currents are caused by the increased adatom drift produced by the increased electromigration force with a stronger electron-wind component.

It was found that the step edges of bunches on the sample annealed with the step-up current at 12 A (figure 6.5(b)) had unusual corrugated edges with sharp angular features.

The orientation of these features was analysed in finer detail. As can be seen in figure 6.6(a) the steps within the bunch make clearly definable angles in the range of 90˚ - 125˚. A direct comparison can be made between the crystallographic directions noted for the W(110) surface in figure 6.6(b) and the steps figure 6.6(a), which allows the crystallographic directions of the steps to be labelled in the AFM image in figure 6.6(a).

This morphology can be explained by the under lying crystallographic structure of the surface. When the higher current of 12 amps was applied along the $[\bar{1}\,12]$ direction, atoms on the surface move by hopping to the nearest atomic site. The largest atomic separation between atomic sites on the W(110) plane is along $[\bar{1}\,12]$ direction. Therefore, since adatoms preferentially diffuse to the nearest atomic position, the $[\bar{1}\,12]$ crystallographic direction is unfavorable, resulting in the coarse step edges forming seen in figure 6.6(a).

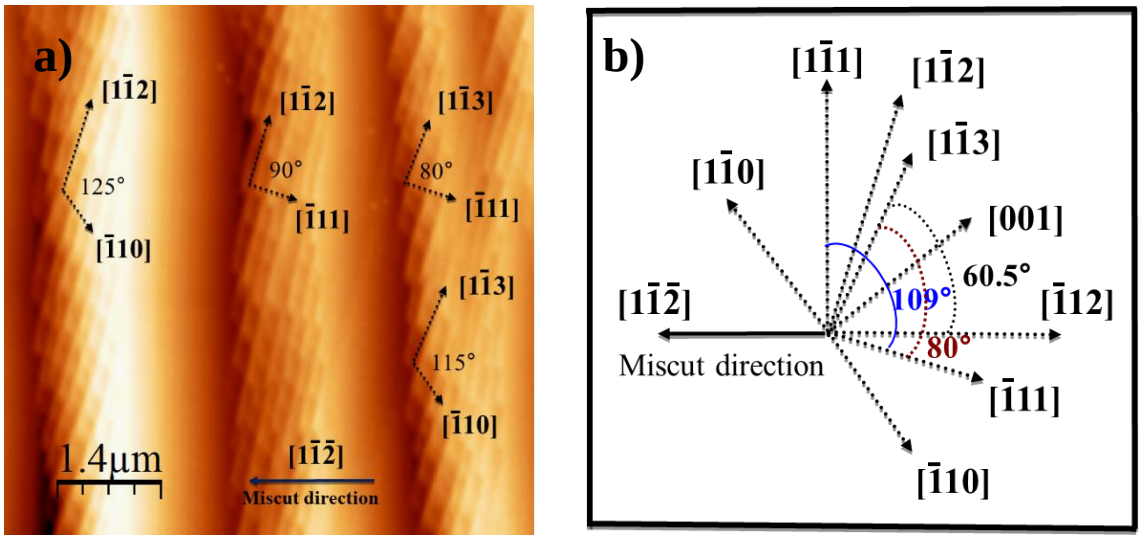

Figure 6.6: (a) Step bunching behaviour on a W(110) surface at 1500˚ C with an applied step-up electric field $E \approx 60$ mV/cm, $I = 12$ A. The surface is off cut 2.6˚ toward the $[1\,\bar{1}\,\bar{2}]$ direction. Step bunches created on this surface have corrugated edges formed by many minor steps with angles between them greater than 90˚. (b) A top view schematic notes the crystallographic directions on the W(110) surface.

A dependence between the bunch height and its maximum slope was found to exist for all samples. As the bunch height increases the maximum slope also increases, this is

evident from a plane levelled cross-sectional profile and its derivative, as shown in figure 6.7(a) and (b) respectively.

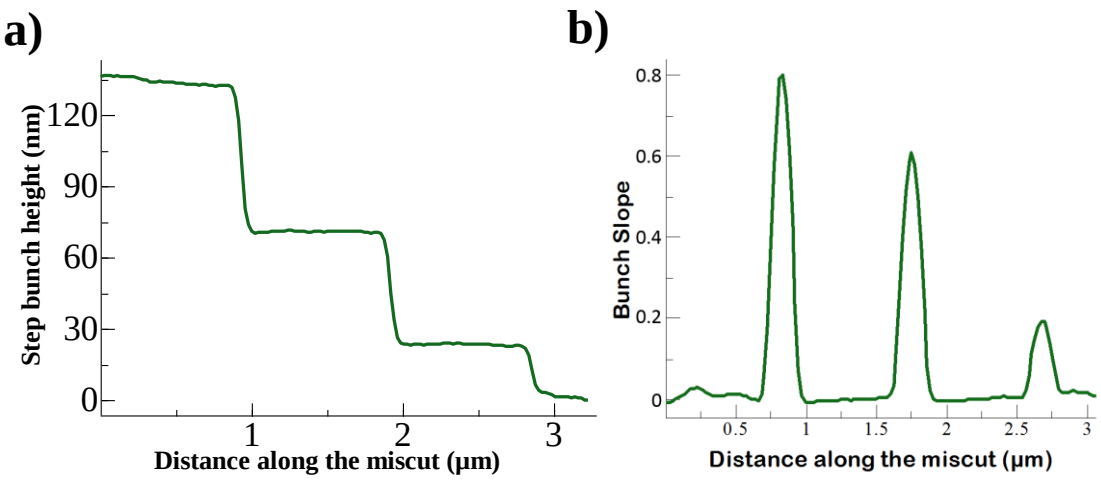

Figure 6.7: The relationship between the line profile of a typical step bunched surface and the slopes attributed to the step bunches separating flat terraces. The surface is off cut by 2.6˚ and annealed with a current of 6A in the step-up direction. (a) Plane levelled line profile along the miscut. (b) Corresponding slope of the line profile.

A quantitative study was made of the relationship between the step bunch height and the maximum slope. The sample with the 2.6˚ miscut, annealed with step-up 6A current for 6 hours, as seen in figure 6.2(d), was analysed by *ex-situ* AFM. Using the AFM topographical data the distribution of the step-bunch dimensions was determined, height (h) was measured with an error of ~ 1 nm from plane levelled profiles. The corresponding maximum slope, y_m, was extracted by taking the maxima of the derivative of levelled step profiles, i.e. step profiles corrected so that flat the W(110) terraces have zero slope and height is taken as the difference between adjacent terraces. As seen in figure 6.8, the dependence between maximum slope and height can be fitted with a power law function of the form, $y_m = y_0 h^{\alpha}$, where α was found to be 0.60 with a fitting error of ±0.03. This result bares a strong resemblance to the experimentally determined scaling relation with $\alpha \approx 0.6 \pm 0.03$ for bunched Si(111) surface after annealing with the step-up electromigration field [25, 29].

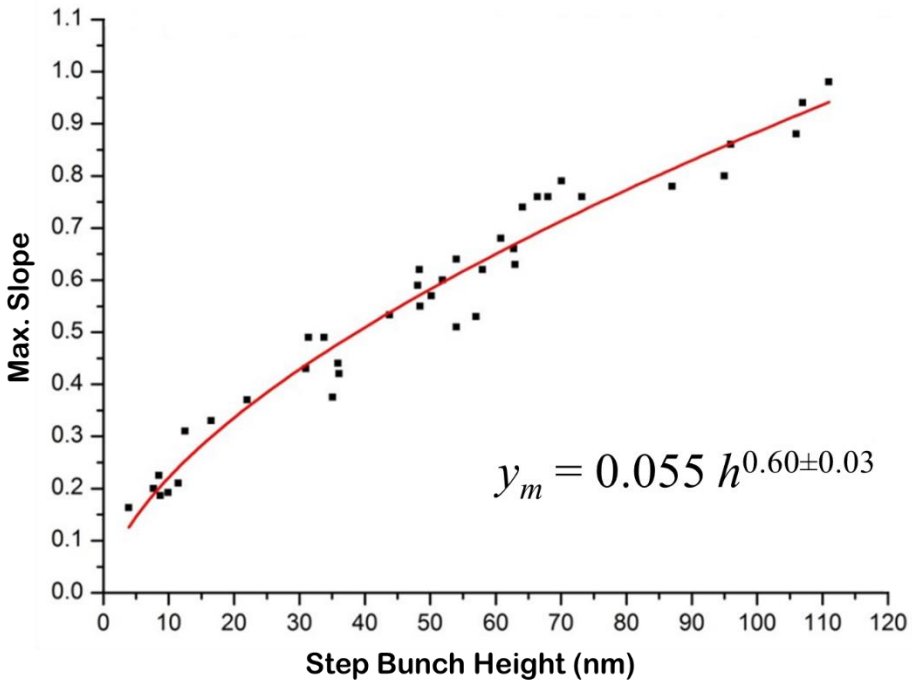

Figure 6.8: Scaling relationship between the maximum slope and height of step bunches on W(110) surface with miscut 2.6˚ annealed by step-up direct current of 6 A towards the [$\bar{1}$ 12] direction.

A similar distribution was attained for the sample with a miscut of 2.6˚, annealed with a step-down DC of 12 A. Figure 6.9 shows a plot the step bunch height h and the maximum slope y_m fitted with the power law function $y_m=y_0h^{\alpha}$. α was found to be ~ 0.69 with an error of ±0.02 on this sample. However for this case the scaling exponent $\alpha \approx 0.69$ is close to the experimentally determined exponent values of α, ranging between 0.64 and 0.67, for bunched Si(111) annealed with step-down electromigration field [25, 29]. The sample annealed with the DC of 12A in the step-up direction was deemed unsuitable for maximum slope analysis due to the corrugation of the step edges.

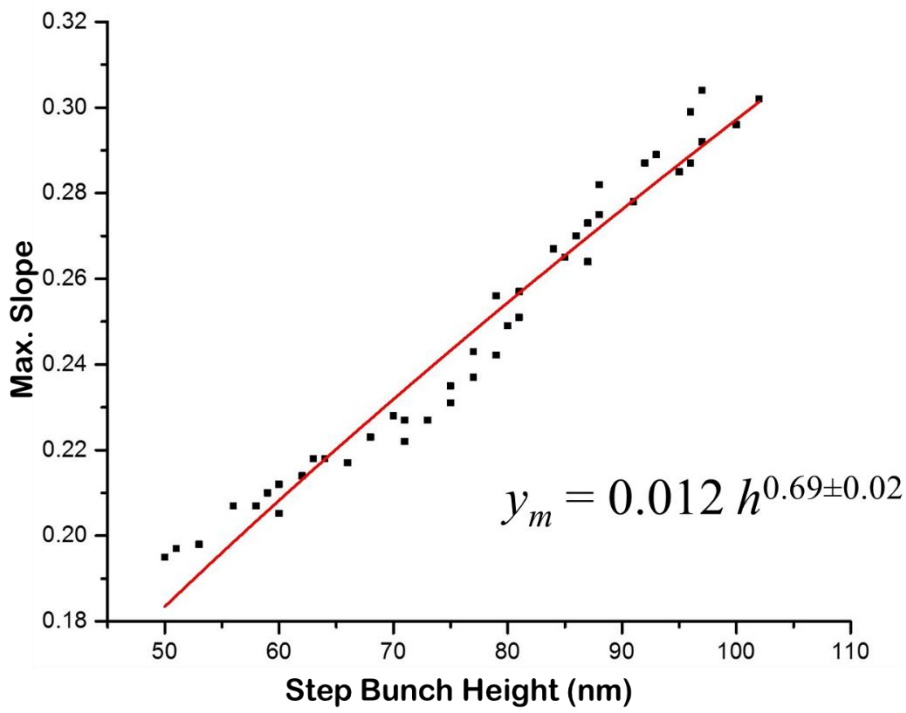

Figure 6.9: Plot of the maximum slope of the bunches against height for W(110) steps with a miscut of 2.6˚, annealed with step-down 12 A current.

6.3 Conclusions

For the first time, electromigration induced step bunching was been observed on the surface of a metal and the resultant surface morphology due to the step bunching process was examined by scanning probe microscopy. Using a combination of DC and irradiative heating, electric field-induced step bunching was observed on several tungsten single crystals for a variety of surface miscut angles annealed at 1500˚ C. The electric fields of the order of 30 mV/cm, 52 mV/cm and 60 mV/cm directed towards the miscut direction, were sufficient to initiate the step bunching on the vicinal W(110) surfaces at this temperature. It appears that at the lower electric field of ~ 30 mV/cm the emergence of step bunches was dependent on the direction of the electric field with respect to the step direction. Such a field was barely sufficient to induce marginal step bunching for current in the step-down direction compared to step substantial bunching produced after step-up *E*-field annealing.

For higher electric fields (~ 60mV/cm), step bunches with heights of 30-120 nm were observed on the vicinal W(110) surfaces both for step-up and step-down current directions.

Step bunches with triangular shaped step edges were observed within the bunches of the W(110) surface with a miscut of 2.6°, when an electric field of $E \approx 60$ mV/cm was applied in the step-up direction during annealing. These are believed to be due to anisotropic adatom hopping during annealing underlined by the atomic structure of the surface thus causing the step edges to align along preferential crystallographic orientations.

The relationship between the step bunch height h and maximum slope $y_m = y_0 h^{\alpha}$ was obtained for annealed W(110) samples for both step-up and step-down currents. The scaling exponents were found to be $\alpha \approx 0.6$ and 0.69 for the vicinal W(110) samples with a miscut of 2.6° annealed at 1500° C with electric fields $E \approx 30$ mV/cm ($I = 6$ A) directed towards the $[\bar{1}\,12]$ (step-up) and $E \approx 60$ mV/cm ($I = 12$ A) towards the $[1\,\bar{1}\,\bar{2}]$ direction (step-down), respectively. The observed α values for bunched W(110) surfaces are strikingly similar to the reported values of the scaling exponents of Si(111) [29]. However despite of this agreement, the basic mechanism of step bunching on the Si(111) and W(110) appear to be fundamentally different.

Chapter 7

Impact of Electromigration on Morphology of Vicinal $MgAl_2O_4(100)$ Surfaces

Білім басы - бейнет, соңы - зейнет.

In this chapter, I report on the first observation of electromigration induced step bunching on vicinal $MgAl_2O_4(100)$ with different off-cut directions. It was found that a step bunching instability occurs on vicinal spinel surfaces for electric fields applied perpendicular to the miscut direction. On $MgAl_2O_4(100)$ annealing with electromigration field $E \approx 140$ V/cm at 1400 ˚C in the step-up direction causes the atomic steps to transform into step bunches. Straight and triangular edged step bunches were produced on surfaces with off-cut in the [011] and [001] directions, respectively. Annealing with electric fields in the step-down direction leads to a different faceted morphology. Other aspects of the morphology such as the inner steps formed on the terraces between step bunches are also discussed. Bunched spinel samples with miscuts of 3˚ and 6˚ annealed with a step-up electric field, $E \approx 140$ mV/cm were analysed, and a scaling relationship between the maximum slope of a step bunch, $y_{m,}$, and step bunch height, $h,$ was found that fitted the power law ($y_m \sim h^{\alpha}$), with scaling exponent $\alpha \approx 0.64 \pm 0.02$. These values is similar to the scaling exponents for the step bunched Si(111) surface. Our results suggest that step bunching mechanism is broadly similar for vicinal silicon and insulating spinel surfaces.

7.1 Introduction

Magnesium aluminate ($MgAl_2O_4$) spinel has long been a subject of scientific interest due to both its mechanical and optical properties and technological relevance [154-157]. For instance, $MgAl_2O_4$ is an important template for Fe_3O_4 heteroepitaxy, which finds applications in the fabrication of multilayer devices [158]. Spinel surfaces also have been shown to be promising nearly lattice-matched substrates for the growth of high-quality GaN films and horizontal nanowires [159-161]. In addition, the deposition of strongly oriented Co_3O_4 thin films on $MgAl_2O_4$(100) highlights its potential in cold plasma technologies [162]. Recently, the specific surface structure of $MgAl_2O_4$ has been used as a support material capable of stabilizing Pt nanoparticles during severe aging [163].

Annealing by direct current affects the surface morphology in a conventional way. However, annealing by ac heating, irradiation, or by thermal contact with a heater affects the surface morphology in an unconventional way. The latter two common methods of heating will be referred to as thermal annealing here to distinguish them from annealing by direct current. It has been suggested that, by the thermal annealing of $MgAl_2O_4$(100) at 1200° C in oxygen, Mg ions in the bulk become mobile at high temperature and could fill in a part of the Mg vacancies on the surface, which can help stabilize the surface [91]. Further surface stabilization is achieved by the formation of wide elongated patches with Al terminated step edges. The (001) surface of spinel, upon annealing at 1200-1800° C for 8 hours in vacuum, rearranges into the step-and-terrace morphology with wide square terraces, resulting in surface faceting and coarsening [164].

This chapter discusses the successful observation of step bunching induced by electromigration on the surface the insulator $MgAl_2O_4$(100). As with Si(111), step bunching occurs on the spinel surfaces due to biased adatom diffusion, resulting from the force on charged particles, induced by the electric potential. Different step bunching morphologies were observed on (100) spinel samples with miscuts of 3° in the [001] and [011] directions. Here, a probable qualitative explanation of the electromigration induced step bunching mechanism on the (100) surface is proposed. It was established that the maximum slope y_m of a step bunch depends on its height h and the dependence between them fits to the

power-law function form ($y_m = y_0 h^{\alpha}$). Scaling exponents of this form were extracted and found to be comparable with the reported values of the scaling exponents for Si(111) [29].

7.2 Results

7.2.1 Thermal Annealing

Vicinal $MgAl_2O_4$(100) samples with miscut angles of ϑ = 3° and 6˚ along the [001] and [011] directions were thermally annealed, that is without an electric field, at 1400 °C in UHV for 6 hours as a control. The resulting surface morphologies can be seen in figure 7.1. The (100) surface of spinel, with a miscut 6° in the [001] direction, rearranges into a step and terrace morphology upon thermal treatment (see figure 7.1(a)). The structure of this surface is characterised by right-angled corrugation of the step edges. The triangular steps, with an average height of 2-4 nm, form faceted steps with the edges aligned along the both [011] and $[0\,\bar{1}\,1]$ directions. This surface arrangement suggests that without the bias of an electric field the adatoms on the (100) spinel surface preferentially diffuse along these two directions during thermal annealing. This surface structure was observed by others in previous studies [164]. Under the same annealing conditions, the sample with the 3˚ miscut in the [011] direction, creates regular faceted steps with heights of 1-3 nm separated by terraces of 10-50 nm in width (Fig. 7.1(b)). As with the previous sample, there is sharp alignment of these steps along the $[0\,\bar{1}\,1]$ direction. Figure 7.1(b) also shows a line profile from this AFM image, taken perpendicular to the step alignment, indicating the step heights. By increasing the miscut angle to 6˚ for the same orientation, the average step height is increased to 2-5 nm and the terrace with becomes 20-70 nm, as shown in figure 7.1(c).

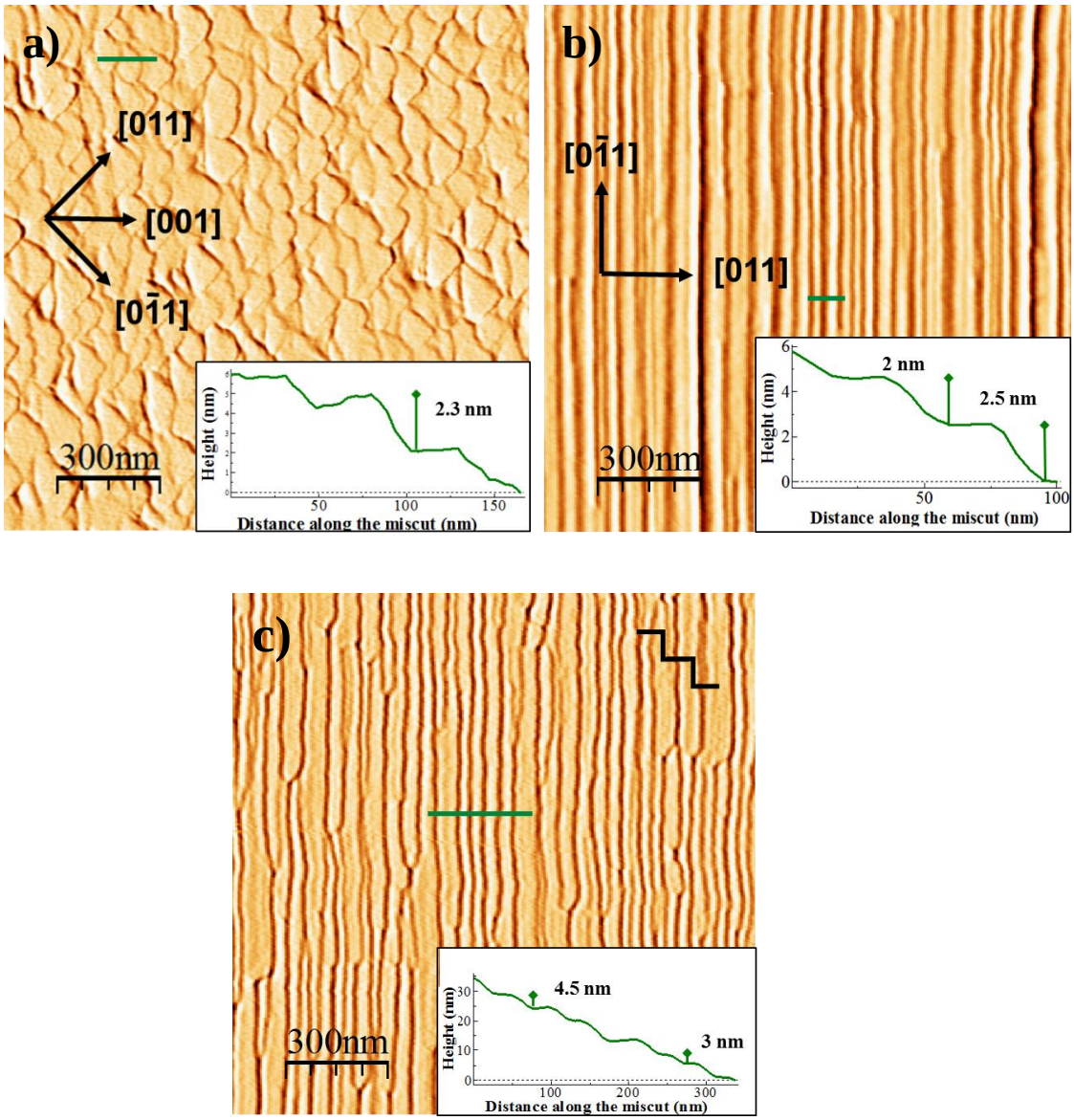

Figure 7.1: Derivative AFM images of $MgAl_2O_4$(100) morphologies after thermal annealing in UHV for 6 hours at 1400 ˚C without an electric field. The miscut direction is from left to right in all images as presented by a staircase symbol in (c). (a) The surface is off cut by 6˚ towards the [001] direction. The step and terrace morphology has an average step height of 2-4 nm. (b) A regular faceted $MgAl_2O_4$(100) surface with a step height of 1-4 nm created on a surface miscut by 3˚ towards the [011] direction. (c) Faceted morphology of the thermally annealed 6° miscut surface, regular steps are aligned along [0 $\bar{1}$ 1] direction and the step heights range from 2-5 nm. Insets show plane levelled line profiles indicating the step heights along the green lines in each of the figures.

The figure also demonstrates that while there is a minor loss in straightness, most of straight steps on the (100) surface preferentially tend to align to $[0\,\bar{1}\,1]$ direction of the crystal.

7.2.2 *E*-field Annealing

If the annealing is performed in the presence of electric field, entirely different morphologies are obtained. Figure 7.2 displays the effect of annealing with an electromigration field of 140 V/cm on $MgAl_2O_4$(100) miscut by 6˚ in the [001] direction. For an E-field in the step-up direction for this miscut, 130-250 nm high step-ledge bunches are produced, with edges aligned along the [011] and $[0\,\bar{1}\,1]$ directions, as seen in figure 7.2(a). The length of these elongated step bunches along these directions is 0.4-1.5 μm. A similar sample, annealed with step-down *E*-field (figure 7.2(b)), has steps with an average height of 8 nm and maximum step height of 12 nm. The step heights are higher compared with those on the faceted surface produced by thermal annealing (see figure 7.1(a)). It was observed that the tips of serrated steps are notably rounder as compared with the thermally annealed morphology. The reason for this can be understood as follows. The exposed atoms at the tips of step-ledges have lower binding energy than those with more neighbours and therefore, under the *E*-field annealing conditions with biased diffusion, adatoms can more readily escape from these extremities and are forced diffuse along the step edges. Eventually the higher adatom detachment from the newly exposed step edge tips leads to the rounding of it.

.

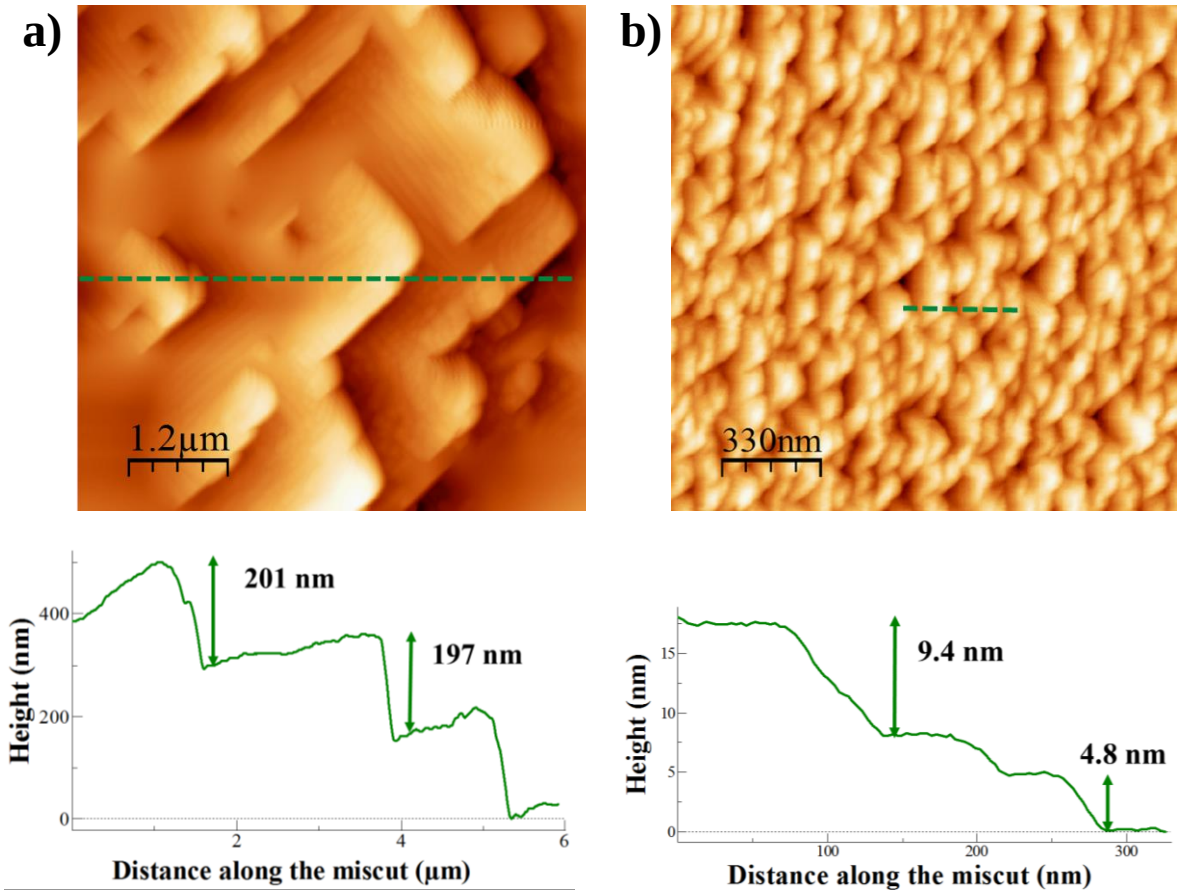

Figure 7.2: (a) Bunched $MgAl_2O_4$(100) sample with a miscut of 6˚ annealed with *E*-field towards the step up [001] direction. Triangular zig-zag shaped step bunches have edges aligned along [011] and [$0\,\bar{1}\,1$] directions. Below a plane levelled line profile of this surface along the dashed green lines is shown. (b) A modified faceted morphology is created on a sample annealed with the electric field in the step-down [$00\,\bar{1}$] direction.

AFM characterisation of $MgAl_2O_4$(100) with a 3° miscut towards the [011] direction, annealed at 1400 °C for 6 hours in the presence of step-up *E*-field of 140V/cm demonstrates a step bunched morphology, an example is presented in figure 7.3(a). The surface is covered by large step bunches with heights of 60-130 nm separated by 0.2-0.4 µm wide terraces.

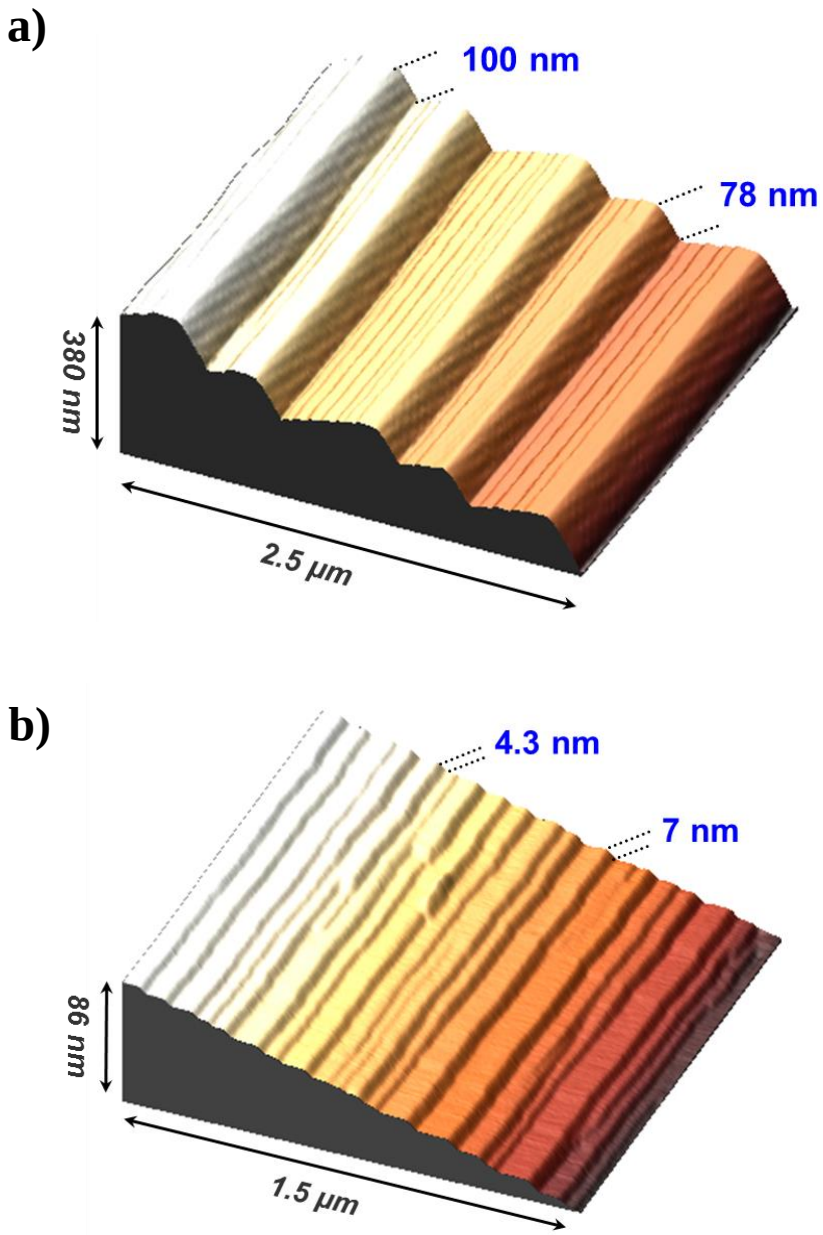

Figure 7.3: Surface morphologies produced on 3˚ miscut $MgAl_2O_4$ by annealing with *E*-field, $E \approx 140$ V/cm, applied along the miscut direction at 1400 ˚C. (a) Surface annealed with a step-up *E*-field, the step bunches are up to ~ 130 nm high separated by 0.2-0.4 μm wide terraces by terraces. (b) Annealed with a step-down *E*-field, produces an array of regular steps, 2-8 nm in height and relatively narrow terrace widths up to ~ 80 nm.

The (100) surface annealed with a step-down *E*-field, however, exhibits a faceted morphology with regular steps 2-8 nm in height separated by terraces 30-80 nm in width, as demonstrated by the AFM image in figure 7.3(b). These steps are, again, nearly aligned

along the [0 $\bar{1}$ 1] direction, with the exception of a number of connecting steps aligned along [011] direction. The step-down *E*-field annealing enhances the faceted step height by some 1-5 nm, as compared with the steps produced by thermal annealing alone (See figure 7.1(b)).

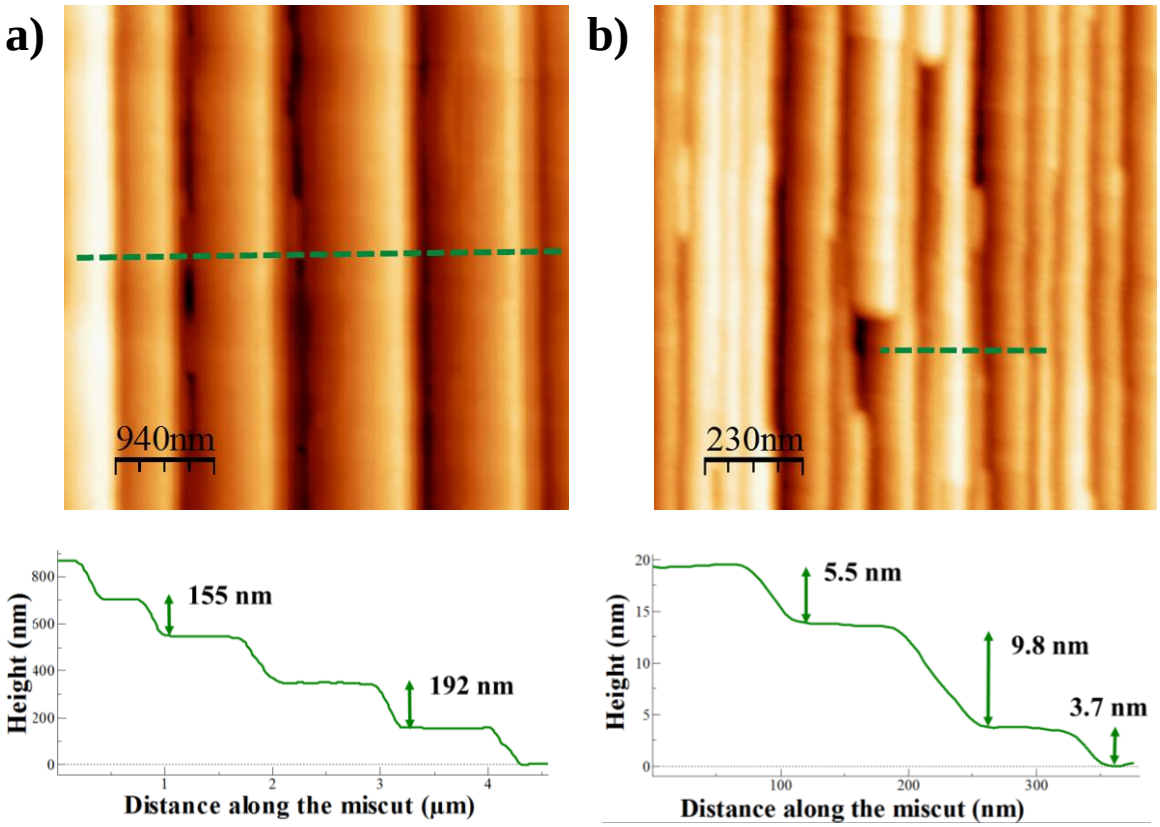

Figure 7.4: (a) Morphology of $MgAl_2O_4$(100) surface with a miscut of 6˚ in the [011] direction obtained by *E*-field annealing, $E \approx 140$ V/cm, along the miscut directions. (a) Bunched surface after annealing with the electromigration field applied along the step-up direction. (b) Relatively small steps 3-12 nm in height with narrow terraces 30-150 nm in width are created on the same (100) surface of $MgAl_2O_4$. Plane levelled line profiles, corresponding to the green dashed lines in both AFM images, are presented below the respective images.

$MgAl_2O_4$(100) samples with a miscut of 6˚ towards the [011] direction were also annealed at 1400ºC for 6 hours with an electric field of 140 V/cm applied along the miscut

direction. Figure 7.4(a) shows such a surface annealed with a step-up *E*-field. The 0.3-1 µm wide terraces on this surface are separated by relatively high step bunches aligned along the $[0\,\bar{1}\,1]$ direction with heights of 120-250 nm. It can be noted, that the step bunches on this surface are higher than for the previous step bunched surface with the 3˚ miscut in the $[1\,\bar{1}\,0]$ direction. The surface of the sample annealed with the step-down *E*-field is characterized by narrow 30-150 nm terraces and small steps of up to 12 nm, as in seen in figure 7.4(b)). Again, these faceted steps are found to be higher compared with the faceted morphology of 3˚ miscut sample annealed under the same conditions (see Fig. 7.2(b)).

To produce a better quantitative understanding of the step bunches, the relationship between the step bunch height and the maximum slope, as has been done for Si(111) [29], was investigated. The $MgAl_2O_4$(100) sample with the 3˚ miscut, as in figure 7.2(a), was analysed by using *ex-situ* AFM measurements. Step bunches with a distributed variety of dimensions were scanned by AFM and their heights (*h*) were measured with an error of ~ 1 nm by taking a line profile of the plane levelled topography. The corresponding maximum slope, $y_{m,}$ was extracted by taking the maxima of the derivative of levelled step profiles, i.e. step profiles corrected so that flat wide (100) spinel terrace region had zero slope, and the height was taken as the difference between the levels of terrace segments adjacent to the step bunches. As shown in figure 7.5, the dependence between maximum slope and height can be fitted well with a power law function of the form, $y_m = y_0 h^{\alpha}$, where α is found to be 0.64 with a fitting error of ±0.02. This scaling relationship shows how $y_{m,}$ continues to increase with step height, whereas for faceted surface the slope would remain constant.

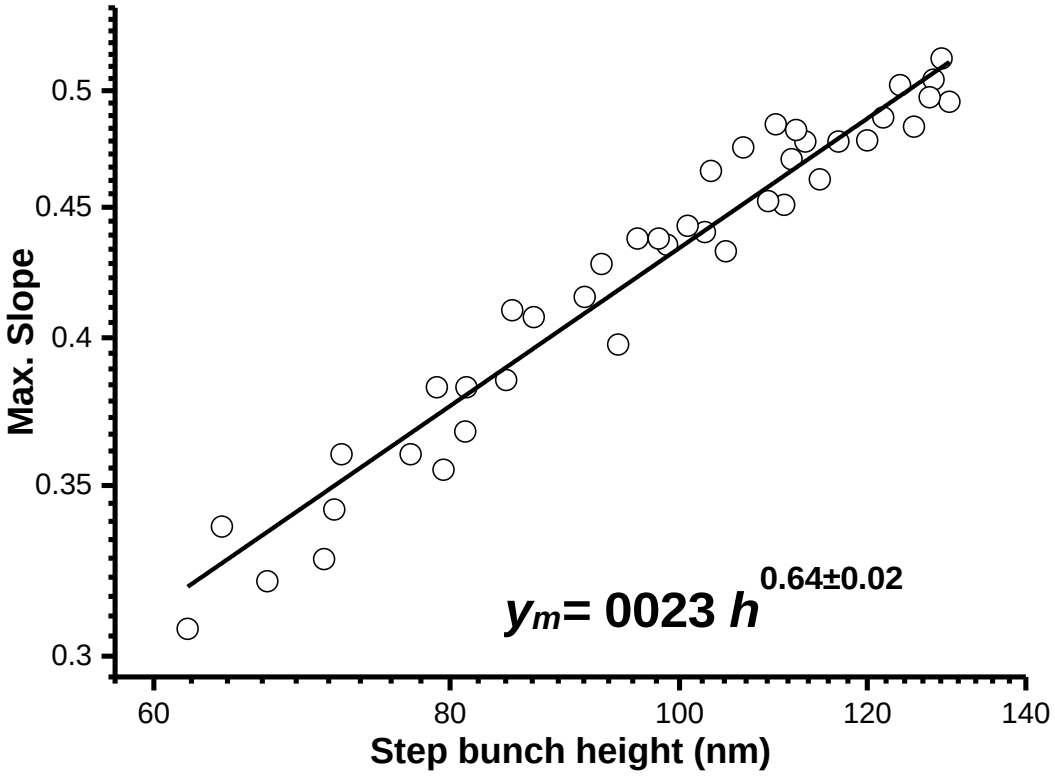

Figure 7.5: A log-log plot of the maximum slope of bunches $y_{m,}$ against their height h for an $MgAl_2O_4(100)$ sample with a miscut of 3˚ towards the [011] direction annealed at $E \approx 140$ V/cm for 6 hours in the step-up direction.

Similarly figure 7.6 shows the dependence between the step bunch height and the maximum slope for the spinel sample with a miscut of 6˚ towards the [011] direction, annealed by step-up E-field of 140 V/cm for 6 hours. In this case α was found to be ~ 0.63 with an error of ±0.02. This is within the error of value found for the sample with the lower miscut. These scaling exponents are similar to the experimentally determined exponent values of α, ranging between 0.57 and 0.59, for bunched Si(111) annealed with a step-up electromigration field [25, 29]. This is despite the differences in strengths of the fields used and the nature of the vicinal surfaces, which suggest parallels in the dynamic processes involved.

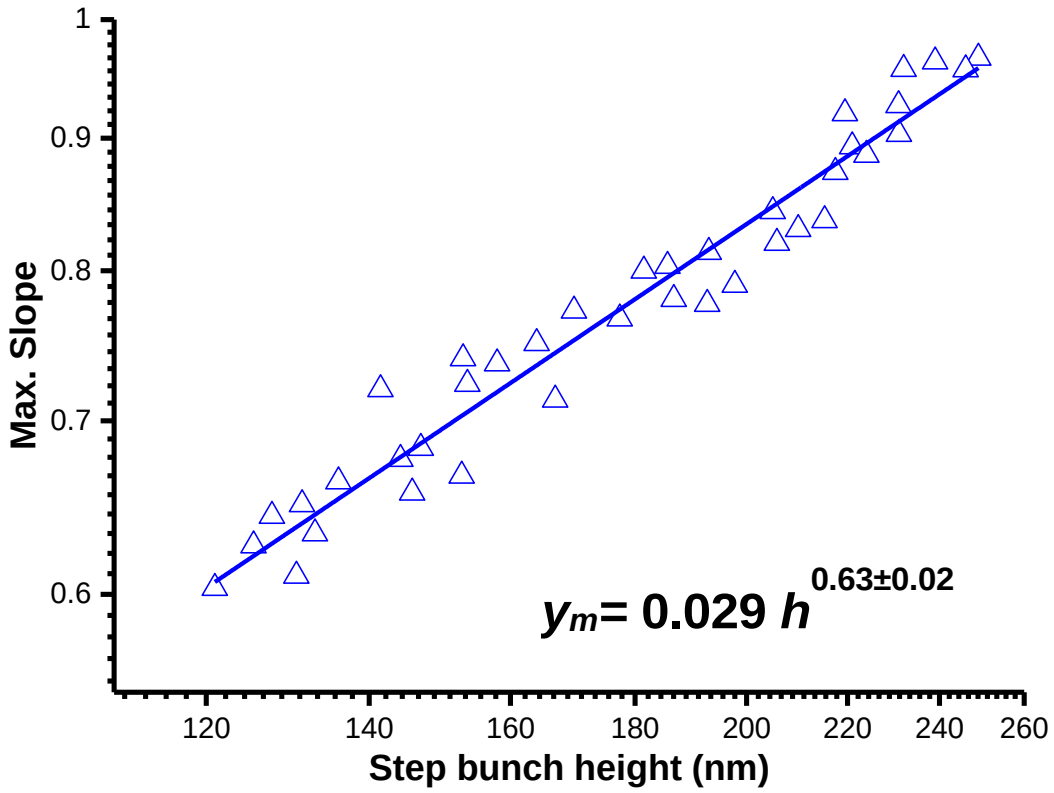

Figure 7.6: Scaling relationship between the maximum slope and height of step bunches on sapphire surface with a miscut 6˚ in the [011] direction annealed by step-up *E*-field of 140 V/cm for 6 hours.

7.2.3 Inner Steps on Large Terraces

It is worth noting that for some step-bunched $MgAl_2O_4$ samples the wider terraces can be broken by inner steps antiparallel to the step bunches, as shown in figure 7.5. These inner steps are clearly visible on the terraces of the step-bunched sample miscut by 3˚ in the [011] direction (figure 7.2(a)). These inner steps have typical heights of 5-15 nm (equating to approximately 25-75 atomic steps, where an atomic step is ~ 2 Å) [84] and are separated by minor terraces 20-40 nm in width. As can been seen from the plane levelled line profile of the spinel surface (figure 7.7(a)), the slope of these inner steps is opposite to that of the main step bunches. The segment of terrace before the first inner step, closest to the step-bunch edge, is noticeably wider (50-120 nm) than the distances between other subsequent steps. Similar sub-bunches of steps, the so-called antibands, were also seen on Si(111) surface as discussed in chapter 4 [30]. Antibands on the bunched Si surface are more

compact and primarily formed via the evolution of atomic steps crossing the wide terraces between step bunches.

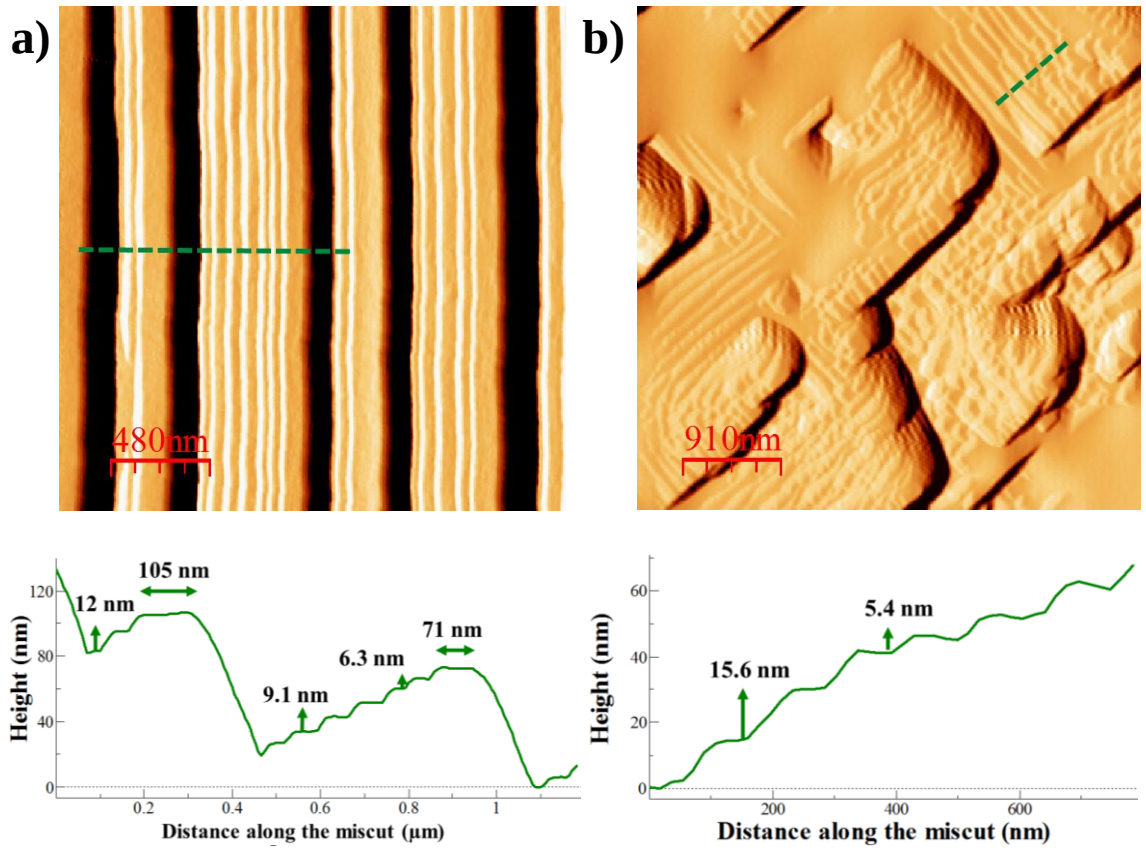

Figure 7.7: Derivative AFM images to highlight inner steps created on spinel terraces between step bunches. Bright and dark areas of the surface correspond to the positive and negative slopes of the inner steps and step bunches, respectively. (a) Inner steps running along the $[0\,\bar{1}\,1]$ direction are antiparallel to the step bunches formed on a sample miscut by 3˚ in the [011] direction. (b) A step-up annealed $MgAl_2O_4$(100) sample with a 6˚ miscut in the $[00\,\bar{1}\,]$ direction results in the formation of inner step-ledges on a terrace of the bunched surface and the edges of these steps are aligned along the [011] and $[0\,\bar{1}\,1]$ directions.

In contrast, the inner steps on bunched $MgAl_2O_4$(100) terraces are not a product of the same evolution of atomic crossing steps. For the step-bunched surface miscut by 6˚ towards the step-down [001] direction inner step-ledges with heights of 5-25 nm are produced on the terraces of the sample, as shown in figure 7.7(b). These steps are aligned

along the both [011] and [$0\bar{1}1$] directions close to the edge of step-ledge bunches by having the form in triangular shapes. This alignment is more clearly apparent the closer they are to the bottom of the step bunches. As with the previous steps the slope of these inner step ledge bunches are also in opposition to the main step ledge bunches.

7.3 Discussion

Literature suggests that the steps on the vicinal $MgAl_2O_4$(100) surface will consist of neighbouring layers containing alternate Mg and Al-O-terminated surfaces on the adjacent terraces [83, 86, 89]. Thus these steps will have fundamentally different properties, as illustrated in figure 7.8(a). This configuration originates from the spinel structure, where it can be seen that the 2 Å-step between layer A and B is different from the 2 Å-step below created between layer B and C, since layers A and B are Al-O-terminated, while layer B is Mg-terminated. Under the thermal annealing conditions the steps move as the result of adatom migration and their attachment/detachment to edges of these layers. Due to the chemical contrast of these different terminations there will be anisotropic surface diffusion of adatoms across these surfaces, which will result in adjacent steps having different velocities. The ions on terraces have different contributions to the step movement. Mg ions with high mobility have greater contribution than the Al ions [91]. If one step in the train moves relatively faster than the adjacent steps, its reduction in width will lead to proportional growth of the subsequent terrace. The example in our case, the Al-O-terminated upper layer A will become wider and the Mg-terminated lower layer B narrower as demonstrated in figure 7.8(b) The movement of the step helps compensate for the polarity of the surface as it liberates atoms which can then be incorporated into adjacent steps. Desorption of certain atoms in the surface layer also occurs. It is known from previous studies that Mg ions preferentially detach from the surface, in part because Mg has lower binding energy since it is tetrahedrally coordinated to four O, while the Al cations are octahedrally coordinated to six O anions. The Mg rich layer B will recede more rapidly as compared to the Al-O terminated adjacent layers. In order to fulfil the polar stabilization, surface vacancies re-organise until octahedral/tetrahedral vacancies are equally favored

and the steps are stabilized by their proximity to others within the train. This means that the step train starts to move with the same velocity, however the perturbations in step width created by this action aid the progression towards the formation of surface faceting.

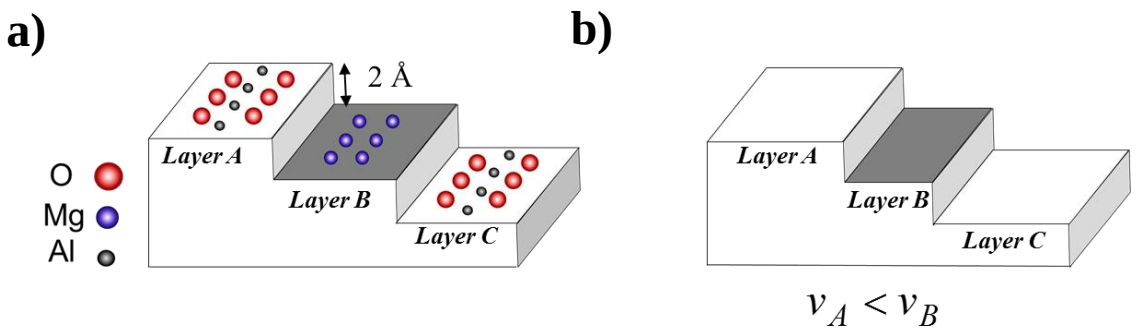

Figure 7.8: Schematic step movement on a vicinal $MgAl_2O_4$ surface.

A qualitative explanation for the formation of the step bunches on $MgAl_2O_4$ can be provided using quite simple physics. The relatively narrowness for un-interrupted terrace width that is observed on both the step-up and step-down annealed surfaces suggests a proportionally short lifetime and distance for adatoms crossing the terraces. Furthermore, it is well known from step dynamics that the energy required for an adatom to hop up a step onto a terrace is significantly greater than that required for it to migrate across the terrace or along the step edge. In our system, if we consider the mobile species on the surface, Mg and Al have a net positive charge and will preferentially migrate in the direction of the electric field. Of these two, Mg is the most readily desorbed, suggesting the surface could easily become Mg deficient. If the field is oriented in the step down direction adatoms will be drawn away from the step edges. This flux of adatoms will stabilise the surface by helping the terraces reach optimum relative occupancies of Mg and Al. This process should be very similar to what appears to happen due to unbiased diffusion on the samples annealed without the presence of an electric field. That is to say, the morphology should thus be like that of a surface where the rearrangement is a result of a thermally activated diffusion process and where there is an equivalence relationship between surface periodicity and the displacement of adatoms [62].

When the electric field is oriented in the step-up direction there is a potential barrier for the adatoms to cross. As such relatively few adatoms can hop onto the terraces, to cross to the adjacent steps, and a higher proportion will be bound up at the step edges, leading to a sharp gradient across the terraces, as is illustrated in figure 7.9(a). It is the presence of an adatom concentration gradient across the terraces that is responsible for the growth of step-bunches on Si(111). However in addition to electromigration, at high temperatures there is substantial desorption of ions from the surface, which means that the concentration is lower than equilibrium n_s^e over the whole layer. It is known that Al is the most stable termination for the step edges [91]. If the step edges within the bunch are Al terminated, it is suggested that Mg adatoms arriving at the bunches are not incorporated into it, and as such they are trapped at the bunches until either they hop over the barrier or are lost from the surface through desorption. The low concentration of Mg adatoms on the terraces will have its most appreciable effect close to the inner edges of the terraces, where adatom concentration will be lowest. Observations at lower temperatures have suggested that micro-faceted structures, pits and patches, with Al terminated edges can form to stabilize the surface [91]. We suggest that structures such as these form in the areas where there is low surface adatom concentration and particularly Mg depleted regions, to stabilize the surface. These then become elongated parallel to the step bunches which further develop to become the inner steps visible in the AFM images. The creation of these additional inner steps edges increase the local adatom flux and concentration, thus stabilizing a further segment of terrace until the width becomes great enough for the adatom concentration to drop again. The additional Al terminated step edges help to stabilize the wider terraces on a surface where there is less Mg available, as compared with surfaces annealed with the field in the opposite direction. This behavior would also explain why the terrace segments closest to the step bunches are the widest, see figure 7.9(b). As they would experience a relatively large adatom flux from the step bunches, compared with the smaller inner steps, as they are a larger sink of Mg adatoms. Thus a step in proximity to the step bunches would recede more slowly than individual steps. However further NC-AFM, X-ray photoelectron spectroscopy (XPS) and surface X-ray diffraction (SXRD) studies would be desirable to quantify of structural occupancies of bunched morphologies of $MgAl_2O_4$ surface.

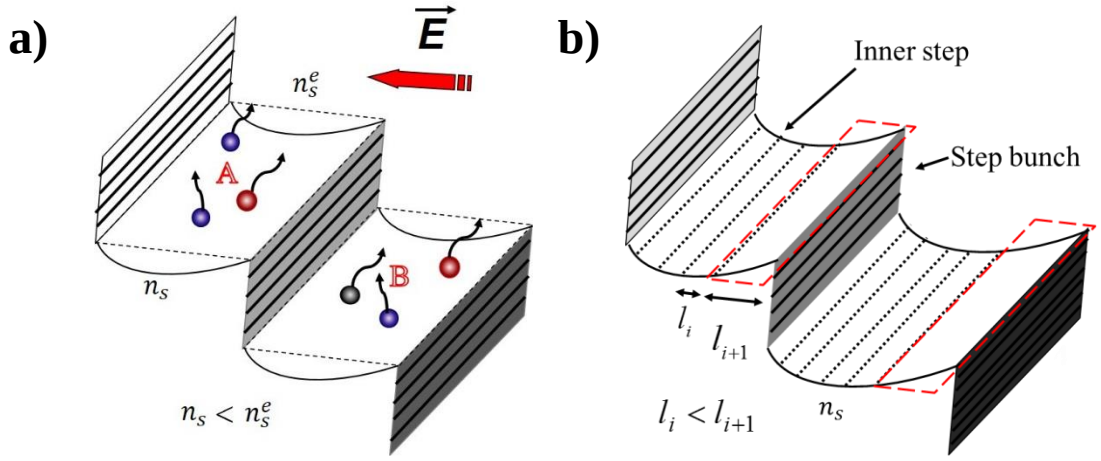

Figure 7.9: Growth of terraces $MgAl_2O_4$.

(a) Actual ion concentration n_s on a terrace is lower than equilibrium n_s^e due to the substantial evaporation. Al terminated step bunch edges act as a Mg sink for the *E*-field in the step-up direction. (b) Al terminated inner steps further stabilize the surface. The outside terrace segment closest to the bunch l_{i+1} is wider than subsequent terrace segment l_i.

7.4 Conclusions

We observed for the first time, electromigration induced step bunching on the surface of the insulator $MgAl_2O_4$(100), when an electric field of ~ 140V/cm was applied to vicinal spinel perpendicular to the miscut direction. Annealing a sample off-cut in the [011] direction with *E*-fields in the step-up direction for 6 hours at 1400 ˚C results in the formation of step bunches separated by wide terraces through the forced the migration of adatoms on the (100) surface. In sharp contrast, step-down *E*-field annealing under the same conditions leads to the formation a regular step train, similar to the faceted surface produced by annealing without an electric field. The wide terraces of the step-bunched surfaces are interrupted by well-structured inner steps running antiparallel to the primary bunches along the [011]. Samples with miscut of 3° in the [001] direction displayed faceted

triangular so-called step-ledges and step-ledge bunches were produced, after annealing with an *E*-field of 140 V/cm. It was also found that similar complementary triangular inner steps are created on the terraces of this bunched surface.

As would be expected, the step bunch height increases with the offcut angle, higher step heights were found on the surface with a 6° miscut compared with step bunches produced on the surface miscut by 3°. However the scaling relationships between the maximum slope of a step bunch height y_m, and step bunch height, remain similar. The scaling exponents were found to be $\alpha \approx 0.64$ and 0.63 with an error of ±0.02 for the bunched $MgAl_2O_4$ samples with a miscuts of 3° and 6°, respectively. These values are within the error of each other, which effectively demonstrates that for low miscuts the slope of the step bunches is independent of the initial inter-step spacing, for constant electric field and temperature. The observed α values for bunched $MgAl_2O_4$(100) surfaces bear similarity to the reported values of the scaling exponents of Si(111), attesting to the universality of the process [29]. Furthermore the step bunching instability occurs on spinel for a specific *E*-field orientation and at the examined temperature, which strongly suggests there is a shared basic mechanism of step bunching instabilities on Si(111) and $MgAl_2O_4$(100).

Chapter 8

Conclusions and Outlook

Жеті жұрттың тілін біл,

Жеті түрлі білім біл.

8.1 Conclusions

This thesis has examined the formation of crossing steps and antibands on the terraces of bunched Si(111). It is known that during prolonged DC anneals of vicinal Si(111) surface may lead to the formation of antibands which have an inclination opposite to that of the miscut angle. The dependencies of these features on annealing parameters such as anneal time and strength of applied electric field were also investigated. Antiband instability on bunched Si(111) has been studied under the condition of adatom surface diffusion limited sublimation. Here, a theoretical treatment was given for the evolution of atomic steps crossing the wide terraces towards the formation of antibands. The adatom concentration gradient which was compensated by the different crossing step curvature was found to be dependent on the value of the electromigration force. However the location of antibands on terraces was found to be independent of the electric field direction which is in strong agreement with experimental findings. The conditions for the onset of antiband instability and antiband formation was found to depend strongly on the degree of surface vicinality.

Finally, our experiments support strongly the derived condition for the onset of antiband instability.

The formation of ordered arrays of step-bunches was demonstrated for the first time on classes of materials which had not been known before to exhibit this phenomenon. In particular, we observed step bunches on vicinal tungsten, sapphire and spinel surfaces by applying the electromigration field along the miscut directions. These results demonstrate the universality of the phenomenon and it opens new pathways to the control and understanding of the morphologies of those surfaces.

Different values of the electric field were applied on vicinal Al_2O_3(0001) perpendicular to the step direction. In the case of Al_2O_3(0001) the height of step-bunches was found to increase with annealing time, by annealing samples at 1500°C for durations of 6 and 20 hours. In the case of samples annealed with the applied field in the step down direction, the resulting morphology was found to depend on the annealing time, with faceted surfaces observed after short anneals (6 hr) and weakened stepped-bunches observed following longer anneals (20 hr). The crossing steps on terraces of bunched sapphire surface after prolonged annealing times were found to develop into antibands. The critical field required to initiate step bunching E_{cr}, was found by examining the scaling relationship between the step bunch height and its maximum slope.

For vicinal $MgAl_2O_4$(100), it was found that step-bunching could be induced by applying a step-up electric field of 140V/cm at 1400°C, while in the case of a step-down electric field the surface stabilized as an array of uniform steps. The relationship between the maximum slope and height was investigated by fitting with a power-law function $y_m=y_0h^{\alpha}$. The most probable theoretical treatment has been provided for the step bunching formation on $MgAl_2O_4$(100).

W(110) samples with different miscuts were annealed at 1500 ˚C with the applied electric field aligned parallel to the miscut direction. An electomigration field of $\sim$ 25 mV/cm was found to be sufficient to induce step bunching in both step-up and step-down current directions. Higher electric fields were found to result in an increase in the height of the step bunches. The maximum slope of the bunches against height was plotted for W(110) steps.

The common form of the scaling relationship between the step bunch height and its slope, for the step bunches on Si(111), Al_2O_3(0001) and $MgAl_2O_4$(100) surfaces, suggests similar dynamical processes for adatoms on these surfaces, this despite differences in the field strength, temperature and crystallography. Thus it is arguable that for these semiconductor and insulating surfaces the direct electrostatic force, acting on diffusing adatoms, is responsible for surface migration. However, the most striking similarity between the step bunching behaviour on Al_2O_3(0001), $MgAl_2O_4$(100) and that on Si(111) is the influence that the *E*-field direction has on the surface morphology. Although there are four distinct high temperature annealing regimes for Si(111), in each of them annealing with the electric field perpendicular to the steps produces step bunches in one direction and a regular step array for the opposite direction. Analogously the step bunching instability on Al_2O_3(0001) and $MgAl_2O_4$(100) surfaces has been observed when the *E*-field is applied in the step-up direction at 1500 ˚C and 1400 ˚C, respectively. This may indicate that the *E*-field annealing dependence of sapphire and spinel at this temperature satisfies the conditions of step bunching on Si(111) for the temperature regimes II (~ 1040-1190 ˚C) and IV (>1300 ˚C). However, this is in contrast with the behaviour on W(110) surface where step bunching occurs regardless of *E*-field annealing direction. These results indicate that it is primarily the electron wind which is responsible for the motion of tungsten atoms on vicinal W(110) surfaces.

Models proposed by Stoyanov can be used explain the step bunching instability on Si(111) in each of the annealing regimes and a similar theoretical treatment could plausibly be applied for the case of electromigration on Al_2O_3 and $MgAl_2O_4$. However caution is warranted, as the diffusion equations used for sapphire and spinel will be more complex than for Si. There are two or three elements and combinations thereof to consider, instead of one, when formulating an equation for surface transport. This will mean separate and possibly opposing effective charges for each, where scattering from the other elements may need to be considered, and consequently a variety of drift velocities. Importantly, the models of Stoyanov cannot be applied for the case of W(110), because the same step bunching behaviour occurs on the tungsten surface, as mentioned before, for electric fields in both the step-up and step-down directions at the same temperature. The initiation of

step bunching on metallic and semiconductor surfaces may reflect a different combination of factors present in both.

Spinel elements, for a given temperature, will have different surface concentrations, subject to their availability at the surface and their desorption time. XPS studies have shown that the relative concentrations of elements on $MgAl_2O_4(100)$ are highly temperature dependent [18]. Simplification of the system may however be possible, because while Mg and O are undoubtedly critical to surface stability, at the high temperature of 1400˚C the lifetimes of Mg and O adatoms on the surface will be significantly shorter than those of Al or under coordinated Al-O. Thus the identification of mobile species on the surface is of significant importance as it will determine the direction of the mass flow. Furthermore, as conventional thermal studies of the surface have revealed changes in the composition with increasing temperature, driven by changing mobility and evaporation [18, 19], this may in turn give rise to an exotic temperature dependence with electric field.

Below is a summary table for all the observed step bunched surfaces.

Vicinal Surfaces	Temperature	Step-up *E*-field	Step-down *E*-field	Reversed *E*-field
Silicon Si(111)	~850˚C – 950˚C 1200˚C – 1300˚C	Regular	Bunched	De-bunched
	1040˚C – 1190˚C >1300˚C	Bunched	Regular	
Tungsten W(110)	1500˚C	Bunched	Bunched	No de-bunch
Saphire $Al_2O_3(0001)$	1500˚C	Bunched	Regular or weakened Step Bunches	De-bunched
Spinel $MgAl_2O_4(100)$	1400˚C	Bunched	Regular	Unknown

Figure 8.1: Summary table of results on *E*-field annealed vicinal surfaces.

This table shows the resultant morphology of different vicinal surfaces produced upon *E*-field annealing in the step-up and step-down directions.

8.2 Future work

The results relating to step bunching shown here open up further possibilities for the examination of the W(110) surface. A number of these are outlined below.

1. **Study of the influence of oxidation on adatom movement on the bunched surface of W(110).** The surface of W(110) oxidizes at 1300˚C (see Chapter 3.6.2) and it would be interesting to examine the effect of oxidation on the step bunching process. While step bunching has been demonstrated at 1500°C, it is not known whether or not bunching will occur at 1300°C as required for oxidation. If it can be shown to be the case that step-bunching does occur at this lower temperature, the next step would be to introduce oxygen into the annealing chamber and examine its effects on the bunching dynamics. Adatoms of both types would move along the surface under the influence of the applied electric field. As oxygen and tungsten adatoms must carry partial charges of opposite sign, they will migrate in opposite directions. The effects of binding of oxygen and tungsten atoms and how this binding affects the step bunching would need to be considered. The additional complication of a chemical interaction between the adatoms undergoing electromigration has not been studied before, and would make for a very exciting project.
2. **Effects of a metal on the bunched W(110) surface.** It would be interesting to deposit a metal of lower melting point than tungsten onto the W(110) surface and allow it to freely migrate during the anneal. It would be important to choose a metal that does not interact with the W(110) surface and does not form alloys with it. Ag and Cu would be suitable candidates for this experiment. According to the phase diagram [26] these metals do not form alloys with W up to 3422˚C. The effect of the electric field on these extra metals could be investigated by carrying out anneals with the applied field in both the step-up and step-down directions. It may be possible to extract the value of the potential barrier of the step edge on the diffusion of Cu and Ag.

Another potentially fruitful experiment would be to carry out an examination of electromigration on copper in UHV. Copper is an important metal in industry because of its high ductility, malleability, thermal and electrical conductivity. However the effect of

electromigration on Cu has received little attention. Following the results achieved with tungsten in the present work, it would be interesting to try to produce a step bunched morphology on Cu. Then thin films of other metals such as Ag or Al could be deposited onto this surface. It may even be possible to prepare graphene on a step-bunched Cu surface.

Faceted Al_2O_3(0001) substrates could be used as a template for the growth of Si and NiO nanowires (NWs) produced by the atomic terrace low angle shadowing (ATLAS) deposition technique, which is the main method of our group for the fabrication of NWs [27].

Si NWs are attractive due to their potential applications in various fields such as microelectronics, optoelectronics, photonics, photovoltaics and sensors [165-169]. The possibility to study and manipulate the Si NWs in one dimension could prove useful in these applications. In future, optical properties of Si NWs for different values of their thicknesses may be investigated. The study could involve several experimental steps:

- Faceted Al_2O_3(0001) substrates prepared by thermal annealing in air. Planar arrays of Si NWs could then be grown by ATLAS technique, with Si atoms deposited at low angles of several degrees to the surface.
- The wire's optical properties could be studied during their growth by *in-situ* RAS followed by *ex-situ* AFM characterization of their structure.
- The Al_2O_3(0001) substrate together with the deposited Si NWs could then be annealed at high temperatures to investigate the optical response of the Si NWs using *in-situ* RAS measurements. It would be useful to correlate the optical response of the NWs with the dimensions of the structures produced through annealing.

Recently, resistive switching phenomena in binary transition metal oxides such as NiO, TiO_2, or ZnO have received significant attention because of their potential application in NW-based memory devices [170-173]. It would be worthwhile to investigate the possibility of resistive switching in NiO NW's instead of thin films, which is the norm in the literature. NWs of NiO could be prepared using the following procedure:

- NiO NW arrays on Al_2O_3(0001) prepared using the ATLAS technique. Dimensions of the NWs could be controlled through appropriate choice of the deposition parameter, and confirmed using AFM.

- Optical response of the NiO NWs to be studied by *in-situ* RAS measurements.
- If continuous NiO NWs can be produced using this procedure, then resistive switching experiments could also be conducted.

References

[1] J. J. De Yoreo, and P. G. Velikov. Principles of Crystal Growth and Nucleation. *Reviews in Mineralogy and Geochemistry*, 54: 57-93, 2003.

[2] X. Q. Gong, A. Seloni, and M. Batzill. Steps on anatase TiO_2(101). *Nature Materials*, 5: 665-670, 2006.

[3] C. Hahn, J. Shan, Y. Liu, O. Berq, A. W. Kleijn, and L.B. Juurlink. Employing a cylindrical single crystal in gas-surface dynamics. *The Journal of Chemical Physics*, 136 (11): 114201, 2012.

[4] G. A. Somorjai and D. W. Blakely. Mechanism of catalysis of hydrocarbon reactions by platinum surfaces. *Nature*, 258: 580-583, 1975.

[5] F. Cuccureddu, V. Usov, S. Murphy, C. Ó Coileáin, and I. Shvets. Planar nanowire arrays formed by atomic-terrace low-angle shadowing. *Review of Scientific Instruments*, 79 (5): 053907-1, 2008.

[6] O. Pietzsch, A. Kubetzka, M. Bode, and R. Wiesendanger, Real-Space Observation of Dipolar Antiferromagnetism in Magnetic Nanowires by Spin-Polarized Scanning Tunneling Spectroscopy. *Physical Review Letters*, 84 (22): 5212-5215, 2000.

[7] J. P. Pierce, E. W. Plummer and J. Shen. Ferromagnetism in cobalt–iron alloy nanowire arrays on W(110). *Applied Physics Letters*, 81 (10): 1890-1892, 2002.

[8] S. Dahl, A. Logadottir, R. C. Egeberg, J. H. Larsen, I. Chorkendorff, E. Törnqvist, and J. K. Nørskov. Role of steps in N_2 activation on Ru(0001). *Physical Review Letters*, 83 (9): 1814-1817, 1999.

[9] R. T. Vang, K. Honkala, S. Dahl, E. K. Vestergaard, J. Schnadt, E. Lægsgaard, B. S. Clausen, J. K. Nørskov, and F. Besenbacher. Controlling the catalytic bond-breaking selectivity of Ni surfaces by step blocking. *Nature Materials*, 4: 160-162, 2005.

[10] Bas. L. M. Hendriksen, M. D. Ackermann, R. van Rijn, D. Stoltz, I. Popa, O. Balmes, A. Resta, D. Wermeille, R. Felici, S. Ferrer, and Joost W. M. Frenken. The role of steps in surface catalysis and reaction oscillations. *Nature Chemistry*, 2: 730-734, 2010.

[11] U. Martinez, L. B. Vilhelmsen, H. H. Kristoffersen, J. S. Møller, and B. Hammer. Steps on Rutile TiO_2(110): Active Sites for Water and Methanol Dissociation. *Physical Review B*, 84: 205434, 2011.

[12] J. L. MacManus-Driscoll, P. Zerrer, H. Wang, H. Yang, J. Yoon, A. Fouchet, R. Yu, M. G. Blamire, and Q. Jia. Strain control and spontaneous phase ordering in vertical nanocomposite heteroepitaxial thin films. *Nature Materials*, 7**:** 314-320, 2008.

[13] V. Usov, S. Murphy, I.V. Shvets. Study of in-plane magnetic anisotropy of ultrathin epitaxial Fe films grwon on vicinal Mo(110) surface*. Journal of Applied Physics*, 95 (11): 7312-7314, 2004.

[14] V. Moshnyaga and K. Samwer. Ferromagnetic Manganite Films. *Handbook of Magnetism and Advanced Magnetic Materials*, 2007.

[15] L. Néel. Anisotropie magnétique superficielle et surstructures d'orientation. *Journal de Physique et Le Radium*, 15: 225-239, 1954.

[16] H. C. Mireles, and J. L. Erskine. Surface-Step-Induced Double Magnetic Switching of Fe on Vicinal W(100). *Physical Review Letters*, 87 (3): 037201-1, 2001.

[17] J. Chen and J. L. Erskine. Surface-step-induced magnetic anisotropy in thin epitaxial Fe films on W(001). *Physical Review Letters*, 68 (3): 1212, 1992.

[18] H. J. Choi, Z. Q. Qiu, J. Pearson, J. S. Jiang, D. Li, and S. D. Bader. Magnetic anisotropy of epitaxial Fe films grown on curved W(001) with a graded step density. *Physical Review B*, 57 (20): R12713-R12716, 1998.

[19] W. Weber, C. H. Back, A. Bischof, Ch. Würsch, and R. Allenspach. Morphology-Induced Oscillations of the Magnetic Anisotropy in Ultrathin Co Films. *Physical Review Letters*, 76 (11): 1940-1943, 1996.

[20] J. V. Barth, G. Costantini, and K. Kern. Engineering atomic and molecular nanostructures at surfaces. *Nature,* 437: 671-679, 2005.

[21] T. Zubkov, G. A. Morgan Jr, J. T. Yates Jr, O. Kühlert, M. Lisowski, R. Schillinger, D. Fick, and H. J. Jänsch. The effect of atomic steps on adsorption and desorption of CO on Ru(109). *Surface Science,* 526 (1-2): 57-71, 2003.

[22] A. Latyshev, A. Aseev, A. Krasilnikov, and S. Stenin. Transformations on clean Si(111) step surface during sublimation. *Surface Science*, 213 (1): 157-169, 1989.

[23] S. Stoyanov. Electromigration induced Step-Bunching on Si Surfaces – How does it depend on the temperature and current direction? *Japanese Journal of Applied Physics Part 1*, 30 (1): 1-6, 1991.

[24] E. S. Fu, D.J. Liu, M. D. Johnson, J. D. Weeks, and E. D. Williams. The effective charge in surface electromigration. *Surface Science*, 385 (2-3): 259-269, 1997.

[25] K. Fujita, M. Ichikawa and S. Stoyanov. Size-scaling exponents of current-induced step bunching on silicon surfaces. *Physical Review B*, 60 (23): 16006-16012, 1999.

[26] J. Krug, V. Tonchev, S. Stoyanov, and A. Pimpinelli. Scaling properties of step bunches induced by sublimation and related mechanisms. *Physical Review B* 71, 045412 (4-15): 1-15, 2005.

[27] I. V. Shvets, H. C. Wu, V. Usov, F. Cuccureddu, S. K. Arora, and S. Murphy. Concept of a nanowire array magnetoresistance device. *Applied Physics Letters*, 92 (2), 2008.

[28] E. E. Rodyakina, S. S. Kosobolov, and A. V. Latyshev. Drift of Adatoms on the (111) Silicon Surface under Electromigration Conditions. *JETP Letters*, 94 (2): 147-151, 2011.

[29] V. Usov, C. Ó Coileáin and I. V. Shvets. Experimental quantitative study into the effects of electromigration field moderation on step bunching instability development on Si(111). *Physical Review B*, 83 (15): 155321, 2011.

[30] V. Usov, S. Stoyanov, C. Ó Coileáin, O. Toktarbaiuly, I.V.Shvets. Antiband instability on vicinal Si(111) under the condition of diffusion-limited sublimation. *Physical Review B*, 86 (19): 195317, 2012.

[31] D. M. Polishchuk, A. I. Tovstolytkin, S. K. Arora, B. J. O' Dowd, and I.V. Shvets. Magnetic and resonance properties of Fe nanowire arrays on oxidised step-bunched silicon templates. *Physica E: Low-dimensional systems and Nanostructures*, 67: 192-196, 2015.

[32] S. N. Filimonov and Y. Y. Hervieu. Terrace-edge-kink model of atomic processes at the permeable steps. *Surface Science*, 553 (1-3): 133-144, 2004.

[33] H. C. Jeong and E. D. Williams. Steps on surfaces: experiment and theory. *Surface Science Reports*, 34 (6-8): 171-294, 1999.

[34] F. Leroy, D. Karashanova, M. Duffay, and J.M. Debierre, T. Frisch, J. J. Métois, and P. Müller. Step bunching to step-meandering transition induced by electromigration on Si(111) vicinal surface. *Surface Science*, 603 (3), 507-512, 2009.

[35] P. Nozieres. On the motion of steps on a vicinal surface. *Journal de Physique*, 48 (10): 1605-1608, 1987.

[36] E. D. Williams, R. J. Phaneuf, J. Wei, N. C. Bartelt, and T. L. Einstein. Thermodynamics and statistical-mechanics of the faceting of stepped Si(111). *Surface Science*, 294 (3): 219-242, 1993.

[37] J. M. Bermond, J. J. Metois, J. C. Heyraud, and F. Floret. Shape universality of equilibrated silicon crystals. *Surface Science*, 416 (3): 430-447, 1998.

[38] J. Kallunski, J. Krug, and M. Kotrla. Competing mechanisms for step meandering in unstable growth. *Physical Review B*, 65 (20), 2002.

[39] A. Natori and N. Suga. In-phase step wandering on vicinal Si(111) surfaces. *Applied Surface Science*, 190 (1-4): 96-102, 2002.

[40] V. Usov, C. Ó Coileáin and I. V. Shvets. Influence of electromigration field on the step bunching process on Si(111). *Physical Review B*, 82 (15): 153301, 2010.

[41] A. Latyshev, A. Krasilnikov and A. Aseev. UHV REM study of the Anti-band structure on the vicinal Si(111) surface under heating by a direct electric current. *Surface Science*, 311 (3): 395-403, 1994.

[42] Y. Saito and M. Uwaha. Anisotropy effect on step morphology described by Kuramoto-Sivashinsky equation. *Journal of the Physical Society of Japan*, 65 (11): 3576-3581, 1996.

[43] T. Zhao and J. D. Weeks. A two-region diffusion model for the current–induced instabilities of step patterns on vicinal Si(111) surfaces. *Surface Science*, 580 (1-3): 107-121, 2005.

[44] T. Zhao, J. D. Weeks, and D. Kandel. Unified treatment of current-induced instabilities on Si surfaces. *Physical Review B*, 70 (16): 161303(R), 2004.

[45] S. Stoyanov. New type of step bunching instability at vicinal surfaces during crystal sublimation. *Surface Science*, 370 (2-3): 345-354, 1997.

[46] V. B. Fiks. Ionnaya provodimost' v metallakh i poluprovodnikah (Ionic Conductivity in Metals and Semiconductor). *Nauka*, 1967.

[47] H. B. Huntington and A. R. Grone. Current-induced marker motion in gold wires. *Journal of Physics and Chemistry of Solids*, 20: 76-87, (1961).

[48] D. N. Bly and P. J. Rous. Theoretical study of the electromigration wind force for adatom migration at metal surfaces. *Physical Review B*, 53 (20): 13909-13920, 1996.

[49] H. Yasunaga and A. Natori. Electromigration on semiconductor surfaces. *Surface Science Reports*, 15 (6-7): 205-280, 1992.

[50] Yu. S. Kaganovski. *Ukrainski Fizicheski Zhurnal* (Russian Edition), 27: 1070, 1982.

[51] R. P. Johnson. Construction of filament surfaces. *Physical Review*, 54: 459-467, 1938.

[52] P. Adam and H. Wever. Faceting and surface transport phenomena on tungsten in the presence of an electric field or a temperature gradient. *Surface Science*, 21 (2): 307-323, 1970.

[53] K. Takayanagi. Y. Tanishiro, M. Takanashi, and S. Takanashi. Structural analysis of Si(111)–7x7 by UHV-transmission electron diffraction and microscopy. *Journal of Vacuum Science & Technology A: Vacuum, Surfaces, and Films*, 3(3): 1502, 1985.

[54] J. J. Lander. Chemisorption and Order Surface Structures. *Surface Science*, 1 (2):125-164, 1964.

[55] A. Latyshev, A. Krasilnikov, A. Aseev, L. Sokolov, and S. Stenin. Reflection electron-microscopy study of clean Si(111) surface reconstruction during the (7x7) reversible (1x1) phase-transition. *Surface Science*, 254 (1-3): 90-96, 1991.

[56] R. J. Phaneuf, E. D. Williams, and N. C. Bartelt. Temperature-dependence of vicinal Si(111) surfaces. *Physical Review B*, 38 (3): 1984-1993, 1988.

[57] C. Ó Coileáin. *PhD thesis: Controlled Electromigration on Vicinal Surfaces.* Trinity College Dublin, September 2011.

[58] B. O'Dowd. *PhD thesis: Self-assembled Arrays of Magnetic Nanostructures on Morphologically Patterned Semiconductor Substrates.* Trinity College Dublin, October 2013.

[59] J. Toofan and P. Watson. The termination of the α-Al2O3 (0001) surface: a LEED crystallography determination. *Surface Science*, 401: 162–172, 1998.

[60] J. R. Heffelfinger, M. W. Bench, and C. B. Carter. Steps and the structure of the (0001) α-alumina surface. *Surface Science*, 370: L168-L172, 1997.

[61] L. P. Van, O. Kurnosikov, and J. Cousty. Evoltution of steps on vicinal (0001) surfaces of α-alumina. *Surface Science*, 411 (3): 263-271, 1998.

[62] R. Verre, R. Sovin, V. Usov, K. Fleischer, D. Fox, G. Behan, H. Zhang, and I. Shvets. Equilibrium faceting formation in vicinal Al_2O_3(0001) surface caused by annealing. *Surface Science*, 606 (23-24): 1815-1820, 2012.

[63] P. R. Ribic, G. Bratina. Behavior of the (0001) surface of sapphire upon high-temperature annealing. *Surface Science*, 601 (1): 44-49, 2007.

[64] S. Curiotto and D. Chatain, Surface morphology and composition of c-, a- and m-sapphire surface in O_2 and H_2 environments. *Surface Science*, 603 (17): 2688-2697, 2009.

[65] O. Kurnosikov. About anisotropy of atomic-scale height step on (0001) sapphire surface. *Surface Science*, 459 (3): 256-264. 2000.

[66] L. P. Van, J. Cousty, and C. Lubin. Step heights and terrace terminations of a vicinal (0001) α-alumina surface annealed in UHV. *Surface Science*, 549 (2): 157-164, 2004.

[67] O. Kurnosikov, L. P. Van, and J. Cousty, High-temperature transformation of vicinal (0001) Al_2O_3-α surfaces: an AFM study. *Surface and Interface Analysis*, 29: 608-613, 2000.

[68] S. G. Kim, J. S. Yang, and W. T. Kim. Dendritic sublimation of sapphire. *Journal of the American Ceramic Society*, 89 (10): 3194-3200, 2006.

[69] O. Ualibek. *PhD thesis: Tuning and Characterization of Self-assembled Plasmonic Nanoparticle arrays.* Trinity College Dublin, September 2014.

[70] R. Verre, K. Fleischer, R. Sovin, N. McAlinden, J. McGilp, and I. Shvets. *In situ* characterization of one-dimensional plasmonic Ag nanocluster arrays. *Physical Review B*, 83 (12): 125432-125440, 2011.

[71] V. Marchenko. Theory of equilibrium shape of crystals. *Sov. Physical JEPT*, 54 (3): 605-606, 1981.

[72] H. –C. Jeong and E. D. Williams. Steps on surfaces; experiment and theory. *Surface Science Reports*, 34 (6-8): 171-294, 1999.

[73] C. R. Hammond. *The Elements, in Handbook of Chemistry and Physics* (81st edition). CRC press, 2000.

[74] S. R. Vadapoo. *PhD thesis: Self-assembly of C_{60} molecules on oxidized W(110) surface*. Trinity College Dublin, November 2010.

[75] J. P Bourdin, G. Tréglia, M. C. Desjonquiéres, J. P. Ganachaud, and D. Spanjaard. Is the (110) face of tungsten reconstructed. *Solid State Communications*, 47 (4): 279-282, 1983.

[76] D. Chauveau, C. Guillot, B. Villette, J. Lecante, M. C. Desjonquiéres, D. Sébilleau, D. Spanjaard, and G. Tréglia. Photoelectron diffraction study of the unreconstructed and hydrogen reconstructed W(110) surfaces. *Solid State Communications*, 69 (11): 1015-1018, 1983.

[77] M. A. Van Hove and S. Y. Tong. Surface structures of W(110) and W(100) faces by the dynamical LEED approach. *Surface Science*, 54 (1): 91-100, 1976.

[78] R. J. Smith, C. Hennessy, M. W. Kim, C. N. Whang, M. Worthington, and Xu Mingde. High-energy ion-scattering studies of anisotropic surface-atom vibrations on W(110). *Physical Review Letters*, 58 (7): 702-705, 1987.

[79] J. S. Luo and B. Legrand. Multilayer relaxation at surfaces of body-centered-cubic transition metals. *Physical Review B*, 38 (3): 1728-1731, 1988.

[80] J. C. Buchholz, G. -C. Wang, M. G. Lagally. Surface crystallography of W(110) and W(110) p (2x1) – O: The position of W atom. *Surface Science*, 49 (2): 508-528, 1975.

[81] Z. M. Zhurtsov and A. A. Shebzukhov. *Fizika Khimia poverhnosti.* 48-56, 1982.

[82] P. Villars, L. D. Calvert, Pearson's Handbook of Crystallographic Data for Intermetallic phases, *American Society for Metals*, Metals Park, 1989.

[83] J. H. Harding. The simulation of general polar boundaries. *Surface Science*, 422 (1-3): 87-94, 1999.

[84] M. K. Rasmussen, A. S. Foster, B. Hinnemann, F. F. Canova, S. Helveg, K. Meinander, N. M. Martin, J. Knudsen, A. Vlad, E. Lundgren, A. Stierle, F. Besenbacher, and J. V. Lauritsen. Stable Cation at the $MgAl_2O_4$(100) Surface. *Physical Review Letters*, 107: 036102, 2011.

[85] F. R. Massaro, M. Bruno, and F. Nestola. Configurational and energy study of the (100) and (110) surfaces of the $MgAl_2O_4$ spinel by means of quantum mechanical and empirical techniques. *CrystEngComm*, 16: 9224-9235, 2014.

[86] C. Barth, A. S. Foster, C. R. Henry, and A. L. Shluger. Recent Trends in Surface Characterization and Chemistry with High-Resolution Scanning Force Methods. *Advanced Materials*, 23: 477-501, 2011.

[87] M. K. Rasmussen, A. S. Foster, B. Hinnemann, S. Helveg, K. Meinander, F. Besenbacher, and J. V. Lauritsen. Noncontact atomic force microscopy imaging of atomic structure and cation defects of the polar $MgAl_2O_4$(100) surface: Experiments and first-principles simulations. *Physical Review B*, 84 (23): 235419, 2011.

[88] C. M. Fang, G. de With, and S. C. Parker. Computer simulation of dissociative adsorption of water on the surface of spinel $MgAl_2O_4$. *Journal of the American Ceramic Society*, 84 (7): 1553-1558, 2001.

[89] C. Noguera. Polar Oxide surfaces. *Journal of Physics: Condensed Matter*, 12 (31): R367-R410, 2000.

[90] N. J. van der Laag, C. M. Fang, G. de With, G. A. de Wijs, and H. H. Brongersma. Geometry of Spinel-$MgAl_2O_4$ {001} Surfaces: First-Principles Simulations and Experimental Measurements. *Journal of the American Ceramic Society*, 88 (6), 1544-1548, 2005.

[91] T. N. Jensen, M. K. Rasmussen, J. Knudsen, A. Vlad, S. Volkov, E. Lundgren, A. Stierle, and J. V. Lauritsen. Correlation between stoichiometry and surface structure of the polar $MgAl_2O_4$ (100)

surface as a function of annealing temperature. *Physical Chemistry Chemical Physics*, 17: 5795-5804, 2015.

[92] P. S. Ho and T. Kwok. Electromigration in metals. *Reports on Progress in Physics*, 52 (3): 301-348, 1989.

[93] Z. Suo, W. Wang, and M. Yang. Electromigration instability: Transgranular slits in interconnects. *Applied Physics Letters*, 64 (15): 1944-1946, 1994.

[94] Yu. S. Vedula. *Ukrainski Fizicheski Zhurnal* (Russian Edition), 14: 132, 1969.

[95] M. Schimschak and J. Krug. Surface Electromigration as a Moving Boundary Value Problem. *Physical Review Letters*, 78 (2): 278-281, 1997.

[96] D. Kandel and E. Kaxiras. Microscopic theory of electromigration on semiconductor surfaces. *Physical Review Letters*, 76 (7): 1114-1117, 1996.

[97] Y. Homma and N. Aizawa. Electric-current-induced step bunching on Si(111). *Physical Review B*, 62 (12): 8323-8329, 2000.

[98] K. Thurmer, D. J. Liu, E. D. Williams, and J. D. Weeks. Onset of step antibanding instability due to surface electromigration. *Physical Review Letters*, 83 (26): 5531-5534, 1999.

[99] Y. Yang, E. Fu, E. Williams. An STM study of current-induced step bunching on Si(111). *Surface Science*, 356 (1-3): 101-111, 1996.

[100] B. J. Gibbons. *PhD thesis: Electromigration induced step instabilities on silicon surfaces.* The Ohio State University, 2006.

[101] K. Burton, N. Cabrera, and F. C. Frank. *Philosophical Transactions of the Royal Society of London Series A-Mathematical and Physical Sciences*, 243 (866): 299-358, 1951.

[102] S. Stoyanov. Step-bunching instabilities of vicinal surfaces during growth and sublimation of crystals the role of electromigration of adatoms. In Gerhard Ertl, Hans Lüth, Douglas L.Mills, and Michail Michailov, editors, *Nanophenomena at Surfaces*, volume 47 of *Springer Series in Surface Sciences*, pages 259-275, 2011.

[103] S. Stoyanov. Heating current induced conversion between 2x1 and 1x2 domains at Vicinal (001) Si surfaces – can it explained by electromigration of Si adatoms. *Japanese Journal of Applied Physics Part 2-Letters*, 29 (4): L659-662, 1990.

[104] R. Schwoebel. Step Motion on Crystal Surfaces. II. *Journal of Applied Physics*, 40 (2): 614, 1969.

[105] G. Ehrlich and F. Hudda. Atomic View of Surface Self-Diffusion: Tungsten on Tungsten. *The Journal of Chemical Physics*, 44: 1039, 1966.

[106] G. Binning, H. Rohrer, C. Gerber, and E. Wiebel. Surface studies by Scanning Tunneling Microscopy. *Physical Review Letters*, 49 (1):57-61, 1982.

[107] G. Binning, C. F. Quate, and C. Gerber. Atomic Force Microscope. Physical Review Letters, 56 (9): 930-933, 1986.

[108] B. E. Murphy. *PhD thesis: The physico-chemical properties of fullerenes and porphyrin derivatives deposited on conducting surfaces.* Trinity College Dublin, February 2014.

[109] C. Ó Coileáin, V. Usov, I. V. Shvets, and S. S. Stoyanov. Critical field behavior and antiband instability under controlled surface electromigration on Si(111). *Physical Review B*, 84 (7): 075318, 2011.

[110] S. I. Bozhko, V. G. Glebovsky, V. N. Semenov, and I. Smirnova. On the growth of tungsten single crystals of high structural quality. *Journal of Crystal Growth*, 311 (1): 1-6, 2008.

[111] B. J. Gibbons, S. Schaepe, and J. P. Pelz. Evidence for diffusion-limited kineticks during electromigration-induced step bunching on Si(111). *Surface Science*, 600 (12): 2417-2424, 2006.

[112] K. L. Man, A. B. Pang, and M. S. Altman. Kinetic length and step permeability on the Si(111) (1x1) surface. *Surface Science*, 601 (20): 4669-4674, 2007.

[113] A. Latyshev, A. Aseev, A. Krasilnikov, and S. Stenin. Reflection electron microscopy study of structural transformations on a clean silicon surface in sublimation, phase transition and homoepitaxy. *Surface Science*, 227 (1-2): 24-34, 1990.

[114] M. Degawa, H. Minoda, Y. Tanishiro, and K. Yagi. Direct-current-indiced drift direction of silicon adatoms on Si(111)-(1x1) surfaces. *Surface Science*, 461 (1-3): L528-L536, 2000.

[115] M. Sato and M. Uwaha. Growth of step bunches formed by the drift of adatoms. *Surface Science*, 442 (2): 318-328, 1999.

[116] A. A. Chernov. *Modern Crystallography III: Crystal Growth. Part I*, Springer, New York, 1984.

[117] K. Sudoh, T. Yoshinobu, H. Iwasaki, and E. D. Williams. Step Fluctuations on Vicinal Si(113). *Physical Review Letters*, 80 (23): 5152, 1998.

[118] D. J. Liu and J. D. Weeks. Quantitative theory of current-induced step bunching on Si(111). *Physical Review B*, 57 (23): 14891, 1998.

[119] S. Stoyanov and V. Tonchev. Properties and dynamic interaction of step density waves at a crystal surface during electromigration affected sublimation. *Physical Review B*, 58 (3): 1590, 1998.

[120] I. Stara, V. Nehasil, V. Matolin, and C. Lubin. Influence of substrate structure on activity of alumina supported Pd particles: CO adsorption and oxidation. *Surface Science*, 365 (1): 69-77, 1996.

[121] S. Gota, E. Guiot, M. Henriot, and M. Gautier-Stoyer, Atomic-oxygen-assisted MBE growth of α-Al_2O_3 (0001): Metastable FeO(111)-like phase at subnanometer thicknesses. *Physical Review B*, 60 (20): 14387-14395, 1999.

[122] A. Sasaki, S. Akiba, A. Matsuda, W. Hara, S. Sato and M. Yoshimoto. Crystallinity of NiO Nanowires Grown at Step Edges of Sapphire Substrate. *Japanese Journal of Applied Physics*, 44 (7): L256-L259, 2005.

[123] J. Son, S. Lim, J. Cho, W. Seong, and H. Kim. Synthesis of horizontally aligned ZnO nanowires localized at terrace edges and application for high sensitivity gas sensor. *Applied Physics Letters,* 93 (5): 053109, 2008.

[124] B. Qi, B. Agnarsson, S. Ólafsson, H. Gíslason, and M. Göthelid. Room temperature deposition of self-assembled Al nanoclusters on stepped sapphire (0001) surface and subsequent nitridation. *Thin Solid Films*, 520 (1): 64-73, 2011.

[125] R. Verre, M. Modreanu, O. Ualibek, D. Fox, K. Fleischer, C. Smyths, H. Zhang, M. Pemble, J. McGilp, and I. Shvets. General approach to the analysis of plasmonic structures using spectroscopic ellipsometry. *Physal Review B*, 87 (23): 235428 (2013).

[126] O. Ualibek, R. Verre, B. Bulfin, D. Fox, V. Usov, K. Fleischer, J. McGilp, and I. Shvets. Manipulating and probing the growth of plasmonic nanoparticle arrays using light. *Nanoscale*, 5: 4923-4930, 2013.

[127] M. A. Fanton, J. A. Robinson, C. Puls, Y. Liu, M. J. Hollander, B. E. Weiland, M. LaBella, K. Trumbull, R. Kasarada, C. Howsare, J. Stitt, and D. W. Snyder. Characterization of graphene films and transistors grown on sapphire by metal-free chemical vapor deposition. *ACS Nano*, 5 (10): 8062-8069, 2011.

[128] H. J. Song, M. Son, C. Park, H. Lim, M. P. Levendorf, A. W. Tsen, J. Park, and H. C. Choi. Large scale metal-free synthesis of graphene on sapphire and transfer-free device fabrication. *Nanoscale*, 4: 3050-3054, 2012.

[129] J. Hwang, M. Kim, D. Campbell, H. A. Alsalman, J. Y. Kwak, S. Shivaraman, A.R. Woll, A.K. Singh, R.G. Hennig, S. Goranta, M.H. Rümmel, and M. G. Spencer. van der Waals Epitaxial Growth of Graphene on Sapphire by Chemical Vapor Deposition without a Metal Catalyst. *ACS Nano*, 7 (1): 385-395, 2013.

[130] E. Joselevich. Self-organized growth of complex nanotube patterns on crystal surfaces. *Nano Research*, 2 (10): 743754, 2009.

[131] Y. Kim, and T. Hsu. Study of α-Al_2O_3 (R) surfaces with the reflection electron microscopy (REM) technique. *Surface Science*, 275 (3): 339-350, 1992.

[132] O. Kurnosikov, L. P. Van, and J. Cousty. High-temperature transformation of vicinal (0001) Al_2O_3 -α surfaces: an AFM study. *Surface and Interface Analysis*, 29 (9): 608-613, 2000.

[133] T. Kimoto, A. Itoh, and H. Matsunami. Step bunching in chemical vapor deposition of 6H- and 4H-SiC on vicinal SiC (0001). *Applied Physics Letters*, 66 (26): 3645-3647, 1995.

[134] Z. L. Wang, and J. Bentley. In-situ dynamic processes on cleaved α-alumina bulk crystal surfaces imaged by reflection electron microscopy. *Ultramicroscopy*, 51 (1-4): 64-80, 1993.

[135] A. Benasoula, J. C. Wolfe, A. Ignatiev, F. O. Fond, and T. S. Leung. Direct-current-magnetron deposition of molybdenum and tungsten with rf-substrate bias. *Journal of Vacuum Science & Technology A: Vacuum, Surfaces, and Films*, 2 (2): 389-392, 1984.

[136] A. M. Haghiri-Gosnet, F. R. Ladan, C. Mayeux, and H. Launois. Stresses in sputtered tungsten thin films. *Applied Surface Science*, 38 (1-4): 295-303, 1989.

[137] H. S. Witham, P. Chindandam, I. An, R. W. Collins, R. Messier, and K. Vedam. Effect of preparation conditions on the morphology and electrochromic properties of amorphous tungsten oxide films. *Journal of Vacuum Science & Technology A: Vacuum, Surfaces, and Films*, 11 (4): 1881-1887, 1993.

[138] S. Basavaiah and S. R. Pollak. Superconductivity in β-Tungsten Films. *Journal of Applied Physics*, 39 (12): 5548-5556, 1968.

[139] N. Suga, S. Ando, and S. Adachi. Properties of tungsten film deposited on GaAs by RF magnetron sputtering. *Journal of the Electrochemical Society*, 132 (9): 2245-2250 (1985).

[140] O. Pietzsch, A. Kubetzka, M. Bode, and R. Wiesendanger. Real-Space Observation of Dipolar Antiferromagnetism in Magnetic Nanowires by Spin-Polarized Scanning Tunneling Spectroscopy. *Physical Review Letters*, 84 (22): 5212-5215, 2000.

[141] J. Hauschild, H. J. Elmers, and U. Gradmann. Dipolar superferromagnetism in monolayer nanostripes of Fe(110) on vicinal W(110) surfaces. *Physical Review B*, 57 (2): R 677-R680, 1998.

[142] L. Carroll, F. Pedreschi, J. D. O'Mahony ,and J. F. McGilp. Optical reflectance anisotropy studies of Fe nanostructures grown on vicinal W(110). *Physica Status Solidi (b)*, 242 (13): 2650-2654, (2005).

[143] J. P. Pierce, E. W. Plummer, and J. Shen. Ferromagnetism in cobalt–iron alloy nanowire arrays on W(110). *Applied Physics Letters*, 81 (10): 1890-1992, 2002.

[144] E. Y. Vedmedenko, A. Kubetzka, K. von Bergmann, O. Pietzsch, M. Bode, J. Kirschner, H. P. Oepen, and R. Wiesendanger. Domain Wall Orientation in Magnetic Nanowires. *Physical Review Letters*, 92 (7): 077207, 2004.

[145] H. J. Elmers, J. Hauschild, and U. Gradmann. Onset of perpendicular magnetization in nanostripe arrays of Fe on stepped W(110) surfaces. *Physical Review B*, 59 (5): 3688-3695, (1999).

[146] M. Bode, M. Heide, K. von Bergmann, P. Ferriani, S. Heinze, G. Bihlmayer, A. Kubetzka, O. Pietzsch, S. Blügel, and R. Wiesendanger. Chiral magnetic order at surfaces driven by inversion asymmetry. *Nature*, 447: 190-193, 2007.

[147] M. Heide, G. Bihlmayer, and S. Blügel. Dzyaloshinskii-Moriya interaction accounting for the orientation of magnetic domains in ultrathin films: Fe/W(110). *Physical Review B*, 78 (14): 140403(R), 2008.

[148] S. Meckler, N. Mikuszeit, A. Preßler, E. Y. Vedmedenko, O. Pietzsch, and R. Wiesendanger. Real-Space Observation of a Right-Rotating Inhomogeneous Cycloidal Spin Spiral by Spin-Polarized Scanning Tunneling Microscopy in a Triple Axes Vector Magnet. *Physical Review Letters*, **103 (**15): 157201, 2009.

[149] S. Meckler, O. Pietzsch, N. Mikuszeit, and R. Wiesendanger. Micromagnetic description of the spin spiral in Fe double-layer stripes on W(110). *Physical Review B*, 85 (2): 024420, 2012.

[150] A. Varykhalov, O. Rader, V. K. Adamchuk, W. Gudat, B. E. Koel, and A. M. Shikin, Oxidation of Au on vicinal W(110): Role of step edges and facets. *Physical Review B*, 75 (20): 205417, 2007.

[151] D. W. Basset. The Thermal Stability and Rearrangement of Field-Evaporated Tungsten Surfaces. *Proceedings of the Royal Society of London. Series A, Mathematical and Physical Sciences*, 286 (1405): 191-203, 1965.

[152] R. P. Gupta, The electron wind force in electromigration. *Journal of Physics and Chemistry of Solids*, 47 (11): 1057-1066, 1986.

[153] D. R. Lide and H. P. R. Frederikse, *CRC handbook of chemistry and physics : a ready-reference book of chemical and physical data*, 75th Edition, CRC Press, 1994-1995.

[154] R. Barton. *Journal of the American Ceramic Society*, **54**: 141-160, 1971.

[155] P. F. Becher. Press-Forged Al_2O_3-Rich Spinel Crystals for IR Applications. *American Ceramic Society Bulletin*, **56**: 1015-1017, 1977.

[156] A. F. Dericioglu and Y. Kagawa. Effect of grain boundary microcracking on the light transmittance of sintered transparent $MgAl_2O_4$, *Journal of the European Ceramic Society*, 23 (6): 951-959, 2003.

[157] K. Izumi, S. Miyazaki, S. Yoshida, T. Mizokawa, and E. Hanamura. Optical properties of 3*d* transition-metal-doped $MgAl_2O_4$ spinels. *Physical Review B*, 76 (7): 075111, 2007.

[158] M. Ziese, A. Bollero, I. Panagiotopoulos, and N. Moutis. Magnetoresistance switch effect in a multiferroic $Fe_3O_4/BaTiO_3$ bilayer. *Applied Physics Letters*, 88: 212502, 2006.

[159] G. Q. Li, J. Ohta, K. Okamoto, A. Kobayashi, and H. Fujioka. Room-Temperature Epitaxial Growth of GaN on Atomically Flat $MgAl_2O_4$ Substrates by Pulsed-Laser Deposition. *Japanese Journal of Applied Physics*. 45, Part 2, Numbers 17-19: L457-L459, 2006.

[160] G. He, T. Chikyow, X. Chen, H. Chen, J. Liu, and Z. Sun. Cathodoluminescence and field emission from $GaN/MgAl_2O_4$ grown by metalorganic chemical vapor deposition: substrate-orientation dependence. *Journal of Materials Chemistry C*, 1: 238-241, 2013.

[161] D. Tsivion and E. Joselevich. Guided Growth of Horizontal GaN Nanowires on Spinel with Orientation-Controlled Morphologies. *The Journal of Physical Chemistry C*, 118 (33): 19158-19164, 2014.

[162] D. Barreca, A. Devi, R. A. Fischer, D. Bekermann, A. Gasparotto, M. Gavagnin, C. Maccato, E. Tondello, E. Bontempi, L. E. Depero, and C. Sada. Strongly oriented Co_3O_4 thin films on MgO(100) and $MgAl_2O_4$(100) substrates by PE-CVD. *CrystEngComm*, 13: 3670-3673, 2011.

[163] W. Z. Li, L. Kovarik, D. Mei, J. Liu, Y. Wang, and Charles H. F. Peden. Stable platinum nanoparticles on specific $MgAl_2O_4$ spinel facets at high temperatures in oxidizing atmospheres. *Nature Communications*, 4: 2481, 2013.

[164] S. V. Yanina and C. B. Carter. Terraces and ledges on (001) spinel surfaces. *Surface Science*, 513 (2): L402-L412, 2002.

[165] X. F. Duan, Y.Huang, R. Agarwal, C.M.Lieber. Single-nanowire electrically driven lasers, *Nature*, 421: 241-245, 2003.

[166] B. Tian, X. Zheng, T. J. Kempa, Y. Fang, N. Yu, G. Yu, J. Huang, C. M. Lieber, Coaxial silicon nanowires as solar cells and nanoelectronics power sources, *Nature*, 449: 885-889, 2007.

[167] P. Yang, R. Yang, M. Fardy. Semiconductor nanowire: What's next? *Nano Letters*, 10 (5): 1529, 2010.

[168] G. Bronstrup, N. Jahr, C. Leiterer, A. Csaki, W. Fritzsche, S. Christiansen. Optical properties of individual silicon nanowires for photonic devices. *ACS Nano*, 4(12): 7113-7122, 2010.

[169] M.D. Kelsenberg, D.B.Turner-Evans, B.M. Kayes, M.A. Filler, M.C. Putnam, N.S. Lewis, H.A. Atwater. Photovoltaic measurements in single-nanowire silicon solar cells. *Nano Letters*, 8 (2): 710-714, 2008.

[170] S. I. Kim, J. H. Lee, Y. W. Chang, S. S. Hwang, and K. Yoo. Reversible resistive switching behaviors in NiO nanowires. *Applied Physics Letters*, 93: 033503, 2008.

[171] Y. C. Huang, P. Y. Chen, T. S. Chin, R. S. Liu, C. Y. Huang, and C. H. Lai. Improvement of resistive switching in NiO-based nanowires by inserting Pt layers. *Applied Physics Letters*, 101: 153106, 2012.

[172] K. Kinoshita, T. Tamura, M. Aoki, Y. Sugitamo, and H.Tanaka. Lowering the switching current of resistance random access memory using a hetero junction structure consisting of transition metal oxides. *Japanese Journal of Applied Physics*, 45, Part 2, Numbers 37-41: L991, 2006.

[173] I. G. Baek, M. S. Lee, S. Seo, M. J. Lee, D. H. Seo, D.-S. Suh, J. C. Park, S. O. Park, H. S. Kim, I. K. Yoo, U.-I. Chung, and J. T. Moon. Higly scalable nonvolatile resistive memory using simple binary oxide driven by asymmetric unipolar voltage pulses. *Technical Digest - International Electron Devices Meeting*, 587: 2004.